6-17-2016

Mechanical Behavior of Hybrid Glass/Steel Reinforced Epoxy Composites

Amanda McBride
University of Connecticut - Storrs, amanda.mcbride@uconn.edu

Mechanical Behavior of Hybrid Glass/Steel Reinforced Epoxy Composites

Amanda K. McBride, EIT
B.S. Civil Engineering, University of Connecticut, 2014

A Thesis

Submitted in Partial Fulfillment of the

Requirements for the Degree of

Master of Science

At the

University of Connecticut

2016

APPROVAL PAGE

Master of Science Thesis

Mechanical Behavior of Hybrid Glass/Steel Reinforced Epoxy Composites

Presented by

Amanda K. McBride, B.S. Civil Engineering

Major Advisor _____
Dr. Arash E. Zaghi

Associate Advisor _____
Dr. Michael Accorsi

Associate Advisor _____
Dr. Richard Christenson

University of Connecticut

2016

ACKNOWLEGEMENTS

The University of Connecticut has received funding in support for this research from PFI:AIR-TT National Science Foundation Grant #1500293. I would like to thank the United States Department of Education for providing me with the GAANN Fellowship, allowing me to pursue this research and degree.

I would first like to thank my major advisor, Dr. Arash E. Zaghi, for his continued encouragement and support throughout my time here at the University of Connecticut. I extend my thanks to my associate advisors, Dr. Richard Christenson and Dr. Michael Accorsi. I would also like to thank Dr. Kelly Burke and Dr. Richard Parnas of the Institute of Materials Science for their expertise and assistance.

I would like to thank Philip Lucas from Hexion, Amol Vaidya and Rob Jack from Owens Corning, and Veerle Van Wassenhove and Henk Cornelus from Bekaert (Belgium) for providing materials and technical support for this research. I would also like to thank Peter Glaude, Robert Bouchard, and Matthew Beebe of the School of Engineering machine shops.

The unwavering support of my colleagues and friends Kevin McMullen, Lexi Hain, Dominic Kruszewski, Caitlin O'Brien, Masoud Mehr, Kevin Zmetra, Ned Eskew, Kelly Bertolaccini, and Alicia Echevarria is very much appreciated. I would like to express my gratitude to my undergraduate research assistant and friend, Samuel Turek, for his significant contributions. Lastly, I would like to thank my family for their continued love and support throughout this process.

TABLE OF CONTENTS

LIST OF FIGURES

LIST OF TABLES

ABSTRACT

Our nation's deteriorating infrastructure demonstrates the need for a new class of multifunctional materials that alleviate the shortcomings of traditional materials. Conventional fiber-reinforced polymer (FRP) composites have served as an alternative material in civil structures for the past three decades. They offer high strength and stiffness, low weight, and corrosion resistance, however, lack ductility and the ability to absorb energy before failure.

To address these shortcomings for structural composites, research was conducted to investigate the capabilities of fiber hybridization. Varying volume fractions of thin steel reinforcement were introduced into typical glass fiber reinforced epoxy composites. This hybrid FRP may address the limitations by combining the best characteristics of metal and nonmetal fiber reinforcement and polymeric resin. Three different epoxy resins were tested to compare the strength and ductility in order to guide design of the composite specimens. Three different types of metal reinforcements were explored: 1) small-diameter ductile steel fibers, 2) fine wire steel mesh, and 3) thin perforated steel sheets. Non-hybrid and hybrid composite specimens were manufactured. Coupons with and without holes were tested under monolithic and half-cyclic tensile loading to obtain stress-strain relationships, hysteresis behavior, and failure mechanisms. Failure specimens were examined to understand the damage progression due to the interaction of glass and steel reinforcement. A bilinear hysteresis model was used to predict hybrid fiber reinforced composite cyclic behavior. Incorporating steel fibers into glass/epoxy composites may offer a significant improvement in energy absorption prior to failure and material re-centering capabilities, while maintaining a high strength-to-weight ratio.

1 CHAPTER ONE – BACKGROUND

1.1 Introduction

Our nation's deteriorating infrastructure demonstrates the need for a new class of multifunctional materials that alleviate the shortcomings of traditional materials. Structural materials must provide strength, ductility, and long-term durability under every day service use, as well as performance under natural and man-made hazardous events. Conventional fiber-reinforced polymer (FRP) composites have served as an alternative material in civil structures for the past three decades. They offer high strength and stiffness, low weight, and corrosion resistance, however, lack ductility and the ability to absorb energy before failure. To address this shortcoming for structural composites, research was conducted to investigate the capabilities of fiber hybridization.

The versatility in design and manufacturing of hybrid composites can enable the tailoring of a multifunctional material for a variety of structural design requirements. To this end, varying volume fractions of thin steel reinforcement were introduced into typical glass fiber reinforced epoxy composites. This hybrid FRP may address the limitations by combining the best characteristics of metal and nonmetal fiber reinforcement and polymeric resin. Three different epoxy resins were tested to compare the strength and ductility in order to guide design of the composite specimens. Three different types of metal reinforcements were explored: 1) small-diameter ductile steel fibers, 2) fine wire steel mesh, and 3) thin perforated steel sheets. Non-hybrid and hybrid composite specimens were manufactured. Composite coupons with and without holes were subjected to monolithic and half-cyclic tensile testing to obtain stress-strain relationships, hysteresis behavior, and failure mechanisms. Open-hole testing was used to assess

the vulnerability of the composites to stress concentrations. Failure specimens were examined to understand the damage progression due to the introduction of glass and steel reinforcement. A bilinear hysteresis model was used to predict hybrid fiber reinforced composite cyclic behavior. Characterizing the material properties of this hybrid composite was performed to explore the applicability of the composites in structural engineering.

1.2 Literature Review

This section contains a review of previously conducted studies that serves as the foundation of this research.

1.2.1 Conventional Fiber Reinforced Composites

Fiber-reinforced polymer (FRP) composites are commonly comprised of glass or carbon elastic fibers, and provide a high-strength and lightweight material for a variety of industries, such as automotive, aerospace and sporting equipment. Structural composites are typically comprised of thermosetting polymers including vinyl-esters, epoxies, and polyesters as they do not creep as much thermoplastic resins under elevated temperatures. Not only does the resin act as the binder between the fibers but it also protects the fibers in harsh environments. FRP composites have been utilized in civil engineering as reinforcing bars and also in the repair of reinforced concrete (RC) and steel beams and bridge decks [1]. Recently, FRP jackets have been used as a form of seismic retrofit of reinforced concrete columns.

Composites can provide crash energy absorption, which is favorable in cars that are designed for progressive collapse to reduce the forces felt by passengers [2]. However, elastic fibers are inherently brittle and have a limited energy absorption capacity *prior* to failure. Civil structures are not designed for complete failure and thus the composite energy absorption capacity will not be utilized. This prohibits the use of FRPs in certain applications, specifically

in critical structural elements that may be subjected to extreme events, *during which* energy absorption is crucial. For example, concrete-filled glass FRP tubes (CFFT) have been studied for structural column applications [3]. In 2012, the American Association of State Highway and Transportation Officials (AASHTO) released design guide specifications for CFFTs [4]. However, it specified that CFFT members shall not be used as ductile earthquake resisting members, highlighting the current design limitations.

Researchers have studied various ways to improve composite ductility including polymer matrix toughening via silica nanoparticles or through the use of more ductile polymeric (polypropylene) or natural fibers (flax) [5-7]. However, these methods may compromise the composite strength and stiffness.

1.2.2 Metal Fiber Reinforced Composites

Metal fiber reinforcement has traditionally been used in the form of continuous steel cords in rubber tires [8] or short fibers in engineered cementitious composites (ECC) [9], respectively. Advancements in the manufacturing of metal fibers have introduced a unique class of annealed ultra-thin stainless steel fibers (<100μm), possessing both a high stiffness and failure strain. These fibers are typically used for electromagnetic interference protection in plastics, filtration media, and heat resistant textiles [10]. However, recent studies at KU Leuven, Belgium have been performed on the tensile and impact behavior of unidirectional (UD) and cross-ply polymer composites utilizing these particular steel fibers [11-16]. These studies have investigated the effect of brittle and ductile matrices, fiber architecture, and modified fiber/matrix adhesion. It was shown that composites comprised of stainless steel fibers exhibited failure strains of more than three times that of typical carbon or glass composites. This research

has shown the potential of these fibers to enhance structural performance of composites in terms of failure strain and energy dissipation.

1.2.3 Hybrid Composites

The concept of fiber hybridization was introduced to provide both strong and ductile reinforcement while also alleviating material cost and weight. One class of hybrids, known as fiber metal laminates (FML), consist of alternating layers of thin metal sheets and FRP [17] and is shown in Figure 1-1a. They are commonly layered with aluminum sheets and glass (GLARE) or Aramid (ARALL) FRP and used as an alternative material for airframe structures with enhanced fatigue resistance [18, 19]. GLARE has been commercially implemented in the fuselage of the Airbus A380 [20]. Rubio-González et al. studied residual strength of FMLs after fatigue damage through open-hole testing [21]. The other class of hybrid composites that will be studied herein consists of multiple types of fibers within a matrix (Fig. 1-1b).

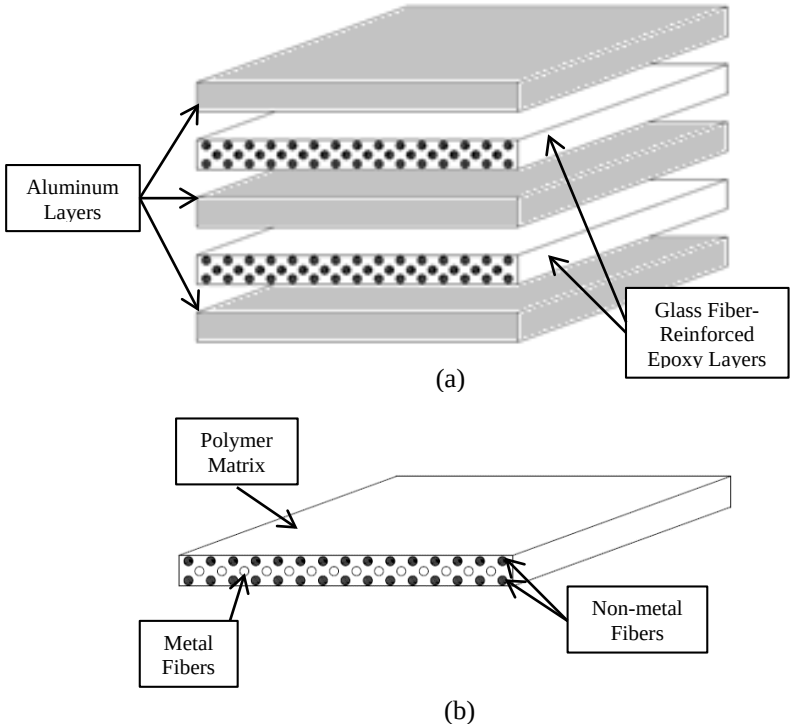

Figure 1-1 Hybrid composite type cross-sections
(a) Fiber Metal Laminate (FML) ex. GLARE; (b) Hybrid Fiber Reinforced Composite

1.2.4 The Hybrid Effect

A state-of-the-art review of the mechanical properties and predictive models of *non-metal* hybrid fiber-reinforced composites has been presented by Kretsis and more recently by Swolfs et al., who briefly incorporated metal fibers [22, 23]. The 'hybrid effect' was investigated by Hayashi and defined as the apparent failure strain enhancement of the low elongation fiber (carbon) in a carbon/glass hybrid composite [24]. In composites with elastic fibers, longitudinal material properties such as stiffness (E_c) and strength (σ), can be estimated based on the Voigt model or "equal strain" assumption leading to the Rule of Mixtures (ROM) [25],

$$E_c = E_f v_f + E_m v_m \quad \text{(Eq. 1.1)}$$

where f = fiber, m = matrix, and v = volume fraction. Marom et al. defined the hybrid effect as the deviation of mechanical properties from the Rule of Mixtures [26], expanding Hayashi's definition of the hybrid effect to other properties beyond failure strain. Therefore, if the experimental property was greater than the predicted value, it was said to have a *positive* hybrid effect, shown in Fig. 1-2.

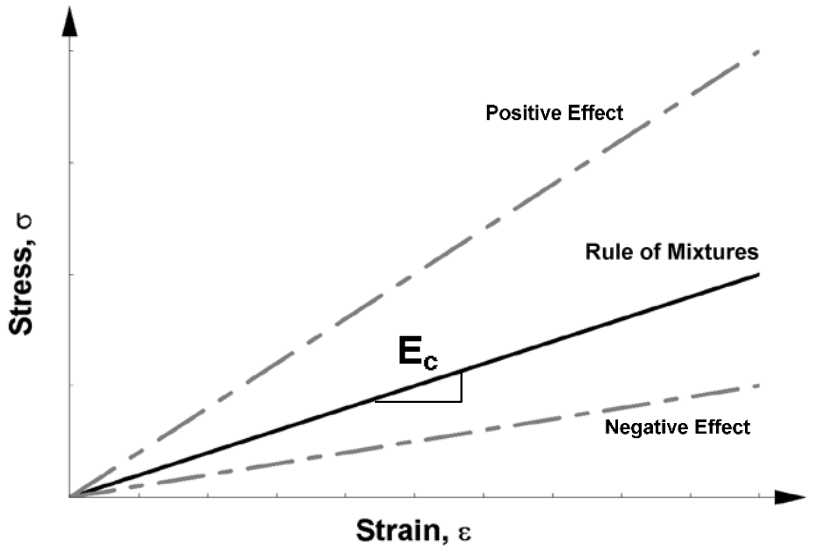

Figure 1-2 Marom et al. definition of the hybrid effect; the deviation of mechanical properties from the rule of mixtures

When incorporating inelastic fibers, the rule of mixtures may still be valid for stiffness because it is calculated in the elastic region. However, the equal strain assumption is no longer valid when incorporating inelastic fibers such as steel; therefore the prediction of the hybrid composite properties using the ROM becomes inaccurate outside the elastic region. Thus, more research is needed to understand the mechanical behavior of nonmetal-metal reinforced hybrid composites as the literature is limited.

1.2.5 Non-metal – Metal Fiber Reinforced Composites

The demand of structural design requirements has posed a need for multifunctional materials [27], and thus, increased composite use. Incorporating metal fibers into composites has previously been studied in terms of non-structural benefits such as electrical conductivity. For example, Breuer et al. investigated a carbon/steel fiber hybrid composite as a lightweight material for use in aerospace applications [28]. However, it was realized that composite mechanical properties can be further tailored using metal fibers. Ahmed studied composite multifunctionality by considering the impact and flexural behavior of the hybridization of glass and steel reinforcement [29]. Satish et al. studied the tensile and compressive behavior of a steel/nylon fiber reinforced polyester composite [30]. Thysen studied the effect of lay-up and fiber ratios on the tensile strength and failure strain of glass/steel composites in epoxy and nylon (PA-6) matrices [31]. Acoustic emission was used to record high-energy events to observe where individual fibers failed relative to the final failure of the entire composite. It was concluded that an epoxy matrix allowed for enough delamination of fibers from the interface. After an elastic fiber failed, the ductile fibers lowered the stress concentration factor of the neighboring fibers, thus increasing failure.

1.3 Objectives and Scope of Work

The goal of this research was to characterize the mechanical properties of a next-generation hybrid composite material through a series of experiments. This paper presents the results of an experimental investigation on the mechanical properties, energy dissipation capacity, and strain restoration ability of composites comprised of unidirectional glass and steel reinforcement in an epoxy matrix. Three different types of metal reinforcements were explored: 1) small-diameter ductile UD steel fibers, 2) fine wire steel mesh, and 3) thin perforated steel sheets. Coupons with and without holes were tested under monolithic and half-cyclic tensile loading. The behavior after damage, energy dissipation during loading, and re-centering capabilities of the different hybrids were of interest to ascertain the applicability of the composites in structural engineering.

1.4 Document Layout

The next chapter discusses the details the testing of the raw materials performed in order to find the mechanical properties for the desired composite material. Both the matrix and reinforcement was studied.

Chapter Three presents the design, manufacturing, and testing of the hybrid composites, comprised of both non-metal and metal reinforcement within the matrix.

Chapter Four provides a comparison of the non-hybrid and hybrid fiber composites in terms of tensile and cyclic behavior. It presents failure mechanisms as well as a predictive hysteresis model.

Chapter Five summarizes the content of the document, presents final conclusions, and recommends future work.

2 CHAPTER TWO – BEHAVIOR OF RAW MATERIALS

2.1 Introduction

The characterizations of the raw materials in this study are detailed within this chapter. This chapter will describe the research design considerations, materials used, specimen manufacturing process, test setup, loading protocols, and experimental results of both the matrix and reinforcement materials that constitute the hybrid composites.

2.2 Matrix

Three different polymeric resins were studied in order to compare the mechanical properties and guide the design of the composites. Five specimens of each resin type were manufactured and cured at room temperature. An additional five specimens of one resin type were manufactured and cured at elevated temperatures. Monolithic tensile testing was performed as ultimate strength and failure strain were of interest in this investigation.

2.2.1 Types of Resin

All resins were two-part thermosetting (bisphenol A-based) epoxy systems and provided by Hexion (Fig. 2-1). For structural applications, thermosets are preferred over thermoplastic resins for increased creep resistance over a wider range of temperatures. The curing agent EPIKURE 3055, an aliphatic amidoamine hardener, was used because it was compatible with all resins. It has a low viscosity with extended pot life, which improves the workability of the matrix. This allows for a faster impregnation of reinforcement in composites during hand lay-up.

The first resin studied was EPON 326 epoxy, a low viscosity, light colored resin that is commonly used in fiber reinforced composites. The second matrix system was EPON 828 epoxy resin. EPON 828 has become a widely used industry resin because of its mechanical versatility and high resistance to a broad range of chemicals. The third matrix system was EPIKOTE 874L-

X-90 epoxy resin. It is typically used in industrial protective coatings and marine applications. The high flexibility of this resin was of particular interest. The epoxies were mixed with a manufacturer-recommended resin-to-hardener weight ratio of 100:50 to obtain optimal polymer cross-linking. The respective volume ratios were calculated using the densities. The epoxy properties provided by the manufacturer are presented in Table 2-1. Complete material data sheets can be found in Appendix A.

Table 2-1 Epoxy properties per manufacturer

Epoxy Type	Weight per Epoxide (g/eq)	Density at 77°F (g/mL)	Viscosity at 77°F (P)
EPON 826	178-186	1.16	65-95
EPON 828	185-192	1.16	110-150
EPIKOTE 874L-X-90	230-270	1.07-1.17	21-23
EPIKURE 3055 Hardener	449-473	0.94	1.5-3.0

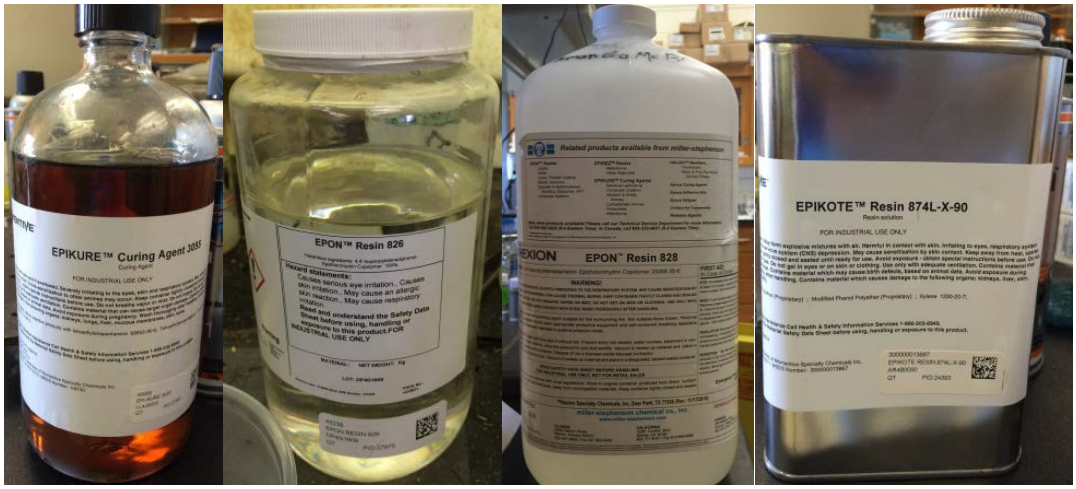

(a) (b) (c) (d)

Figure 2-1 Resin and Hardener Types (supplied by Hexion)
(a) EPIKURE 3055; (b) EPON 826; (c) EPON 828; (d) EPIKOTE 874L-X-90

2.2.2 Manufacturing of Specimens

An aluminum mold with five dogbone-shaped specimens was used as recommended by ASTM D638, shown in Figure 2-2. The mold was coated in Sprayon® thin film release spray prior to epoxy injection for easy sample removal (Fig. 2-3).

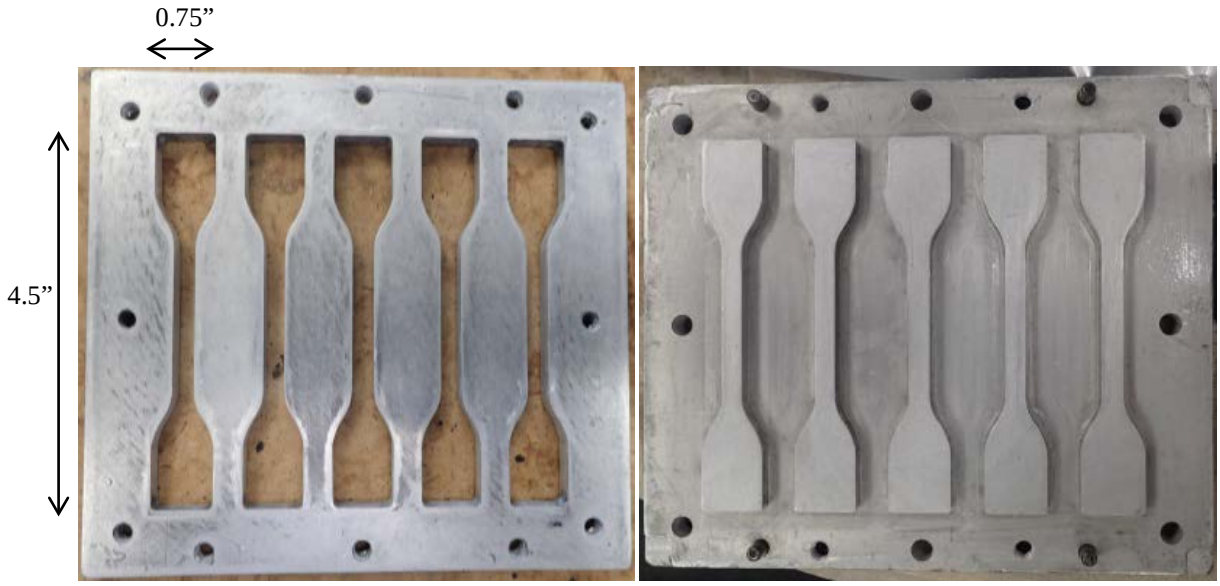

Figure 2-2 Top and bottom pieces of aluminum dog bone mold

Figure 2-3 Mold Release Spray Application

The respective volumes of the resin and hardener were measured and mixed together. Due to the small quantities required, 60mL syringes were used (Fig. 2-4a). The two-part resin system was mixed thoroughly to ensure full polymer cross-linking (Fig. 2-4b). After mixing the resin and hardener, the epoxy was placed into the mold (Fig. 2-4c). Each dogbone was filled with 6.5 mL of epoxy (Fig. 2-4d). The mold was then placed inside a vacuum oven for 20 minutes at 86°F (30°C) and a pressure of 20 in-Hg to remove air bubbles (Fig. 2-4e). The time

in the vacuum oven was dictated by the resin working and gel time. As per the manufacturer, the dog bones were cured at room temperature, 77°F (25°C), for 24 hours under an enclosed hood. The specimens were then carefully removed from the mold. After removal from the mold, some residue from the mold release remained on the specimens (Fig. 2-4f). Therefore specimens were polished on a round sanding wheel to smooth the edges (Fig. 2-4g-h). The final specimens were labeled and dimensions were recorded. Each specimen was 4.5” long, 0.75” wide, and 0.15” thick (114mm×19mm×3.8mm). The gauge length was 1.75” and the gauge width was 0.25” (45mm×6.3mm). Five specimens of each type of epoxy were manufactured in this fashion. There were tiny air bubbles seen in some specimens, and they were noted. The presence of these air pockets can cause premature failure.

Figure 2-4 Epoxy Specimen Manufacturing Process Cured at Room Temperature
(a) Measuring out two-part epoxy with syringe, (b) Thorough mixture of the epoxy, (c) Injecting the epoxy into the dog bone mold with syringe, (d) Complete epoxy-filled dog bone mold, (e) Vacuum oven to de-gas epoxy, (f) Specimens with mold release residue, (g) Polishing dog bone specimens on round sanding wheel, (h) Finalized dog bone specimens

Additional samples of EPON 828 were manufactured using a different curing method in order to see the effects on the mechanical performance. These specimens were cured using the compression molding method in a hot press for 2 hours at 200°F (93°C) under a load of 5,000lbs and pressure of 104psi (7 bars) (Fig. 2-5a-c). The top and bottom platen of the press were heated to the desired temperature and the pressure was applied by hydraulically raising the bottom platen with a lever (Fig. 2-5d-e). Aluminum foil lined the press to avoid any epoxy spillage. The samples were cooled for 30 minutes under no pressure before removal from the mold.

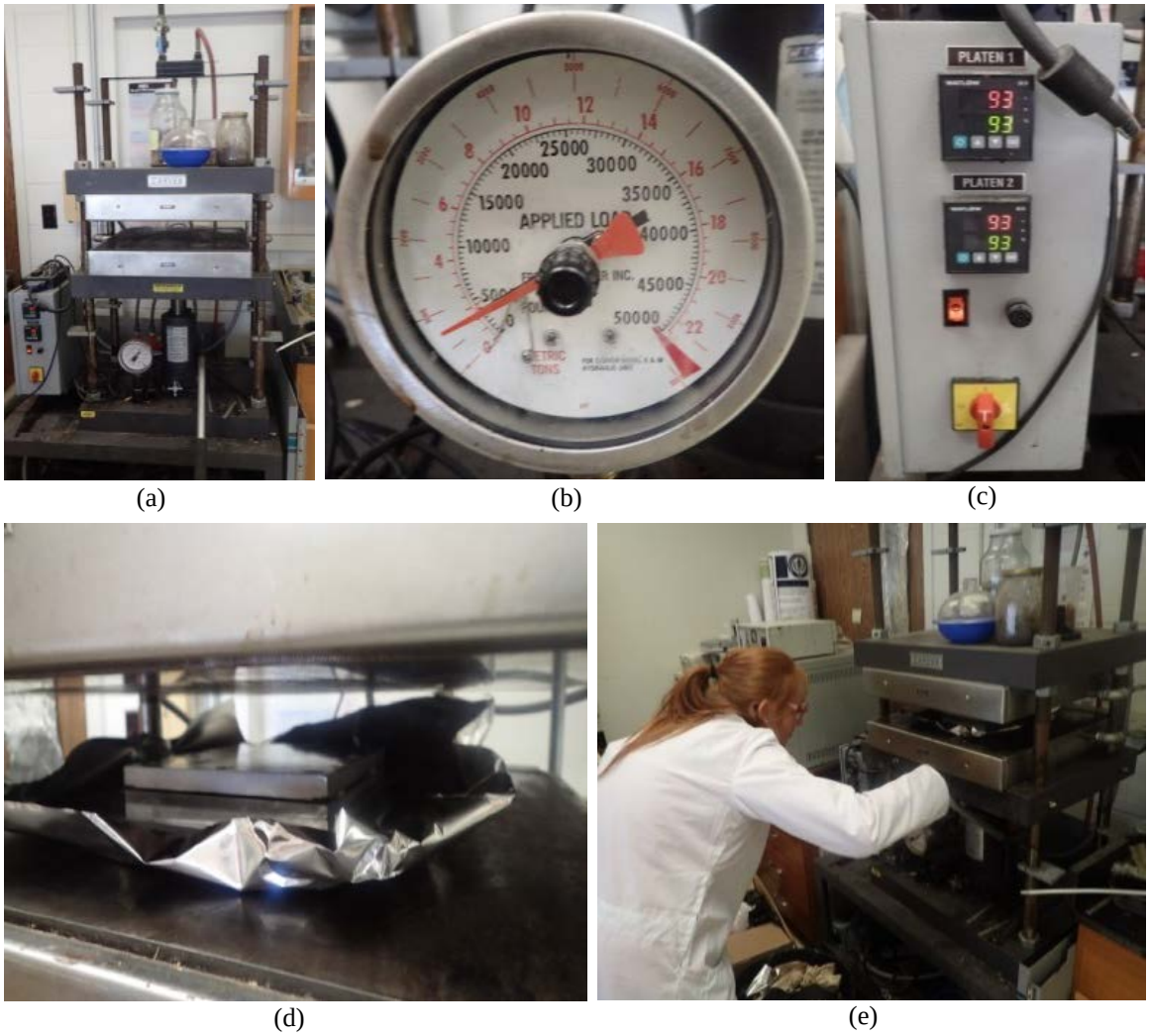

(a) (b) (c)

(d) (e)

Figure 2-5 Epoxy Specimen Manufacturing Process Cured at Elevated Temperatures
(a) Hot press, (b) Applied load gage reading, (c) Top and bottom platen temperature reading, (d) Dog bone mold between platens, (e) Closing platens for applied pressure

2.2.3 Experimental Methodology

Monolithic tensile testing was performed as per ASTM D638 *Standard Test Method for Tensile Properties of Plastics*. The testing was conducted on an Instron 5869 testing machine with a 50-kN (11.-kip) load cell (Fig. 2-6a). The displacement was applied at 0.078 in/min (2 mm/min) and the longitudinal strain was measured using an Instron extensometer with a 1-inch (25.4-mm) gauge length (Fig. 2-6b). End tabs were not necessary because the reduced cross-sectional area of the specimen dictated failure location. Five samples of each epoxy type cured at room temperature, along with five samples of one epoxy type heat-cured, 20 total, were tested. The applied load, machine displacement, and strain data was collected using Instron Bluehill software. All tests were conducted under standard laboratory conditions (73.4 ± 3.6°F). Testing was conducted weeks after manufacturing, thus an incomplete cure would not play a role in the mechanical properties. The tests were documented using photographs and videos. Figure 2-6c displays a complete schematic of the test setup. A failure specimen is shown in Fig. 2-6d. Notice the failure occurred within the gauge length. All failure locations were noted.

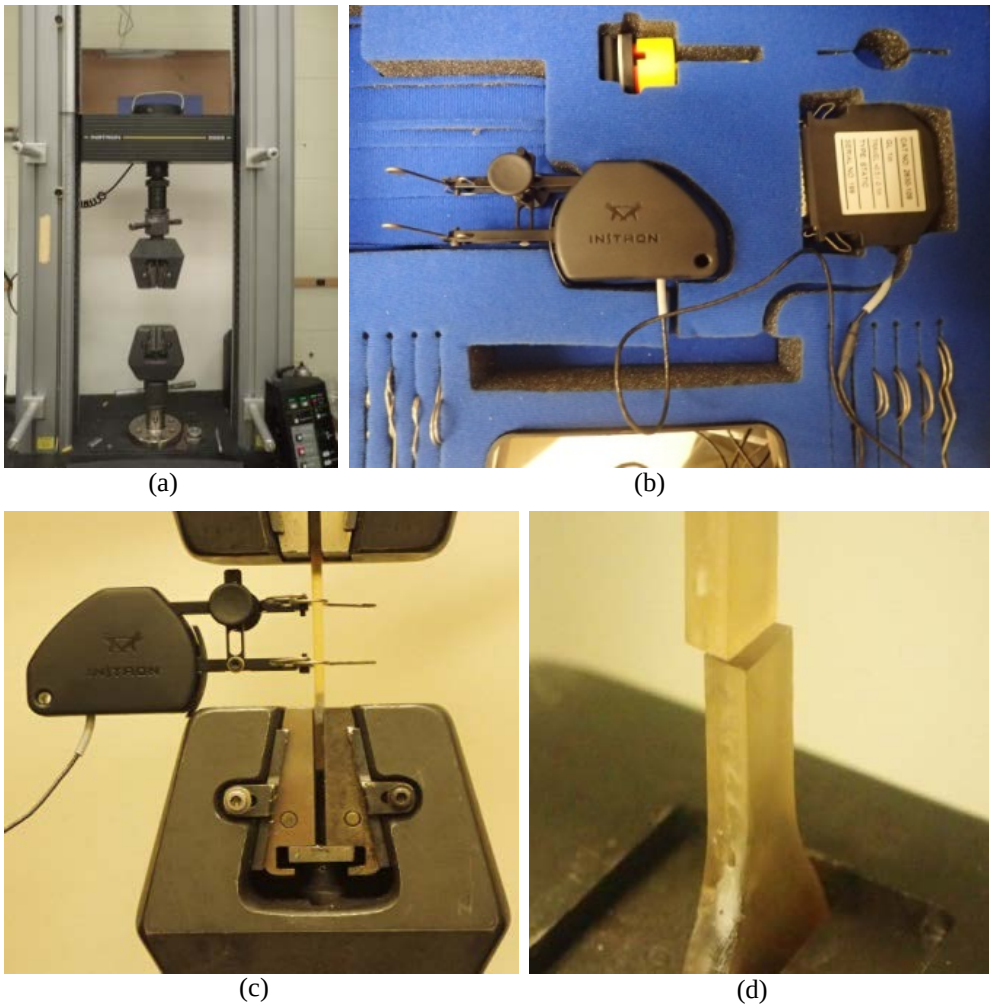

(a) (b)

(c) (d)

Figure 2-6 Epoxy Monolithic Tensile Testing
(a) Instron 5869 testing machine (50-kN load cell), (b) 1-inch gauge length Instron extensometer, (c) Schematic of specimen in test set-up, (d) Post-failure specimen

2.2.4 Results and Observations

The average results of the monolithic tension tests of the room temperature-cured epoxy samples are presented in Table 2-2. At least four out of five specimens of each epoxy type failed within the gauge length of the extensometer. Any sample that failed outside of the gauge length or prematurely due to voids was not included in the average tensile properties.

Table 2-2 Monolithic tensile properties of epoxy specimens cured at room temperature

Epoxy Type	Ultimate Tensile Strength ksi (MPa)	Ultimate Strain (%)	Young's Modulus ksi (GPa)
EPON 826	6.98 (48.1)	2.30	392 (2.70)
EPON 828	7.19 (49.6)	2.71	381 (2.63)
EPIKOTE 874L-X-90	4.11 (28.3)	3.46	208 (1.43)

Figure 2-7 displays the average stress-strain relationships of the three epoxy types cured at room temperature subjected to monolithic tensile testing. EPON 826 had the highest stiffness (392 ksi) of the three epoxy types. EPIKOTE 874 had the lowest stiffness but highest ultimate failure strain (3.46%). EPON 828 had the optimal balance of stiffness (381 ksi), strength (7.2 ksi) and ductility (2.71%) and thus was chosen as the epoxy type to be used in the composites studied herein. This epoxy is also widely used in industry and other literature.

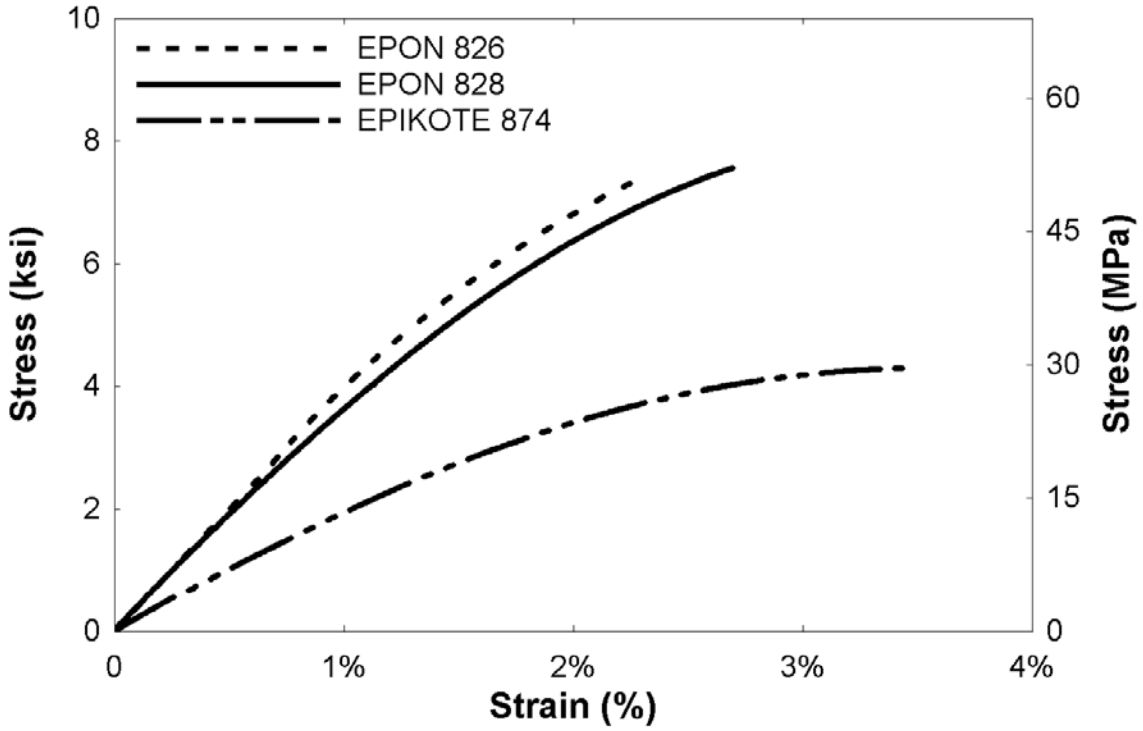

Figure 2-7 Stress-strain relationship of room temperature-cured epoxy types subjected to monolithic tensile testing

Additional samples of EPON 828 epoxy manufactured under elevated temperatures were subjected to monolithic tensile testing in order to observe the difference in mechanical properties and guide the manufacturing process of the composites. Table 2-3 shows the tensile properties of EPON 828 under both room temperature- and heat- cured conditions.

Table 2-3 Tensile properties of EPON 828 epoxy under different curing conditions

Curing Method	Ultimate Tensile Strength ksi (MPa)	Ultimate Strain (%)	Young's Modulus ksi (MPa)
Room Temperature	7.19 (49.6)	2.71	381 (2.63)
Heat Cured	8.25 (56.9)	4.13	372 (2.56)

Figure 2-8 shows the average stress-strain relationship of EPON 828 under different curing conditions. The EPON 828 cured under an elevated temperature of 200°F (93°C) displayed a consistently higher ultimate tensile strength (8.25 ksi) as well as failure strain (4.13%). The manufacturing process had no significant effect on the stiffness. These results confirmed that the hybrid composite manufacturing process would be compression molding under elevated temperature.

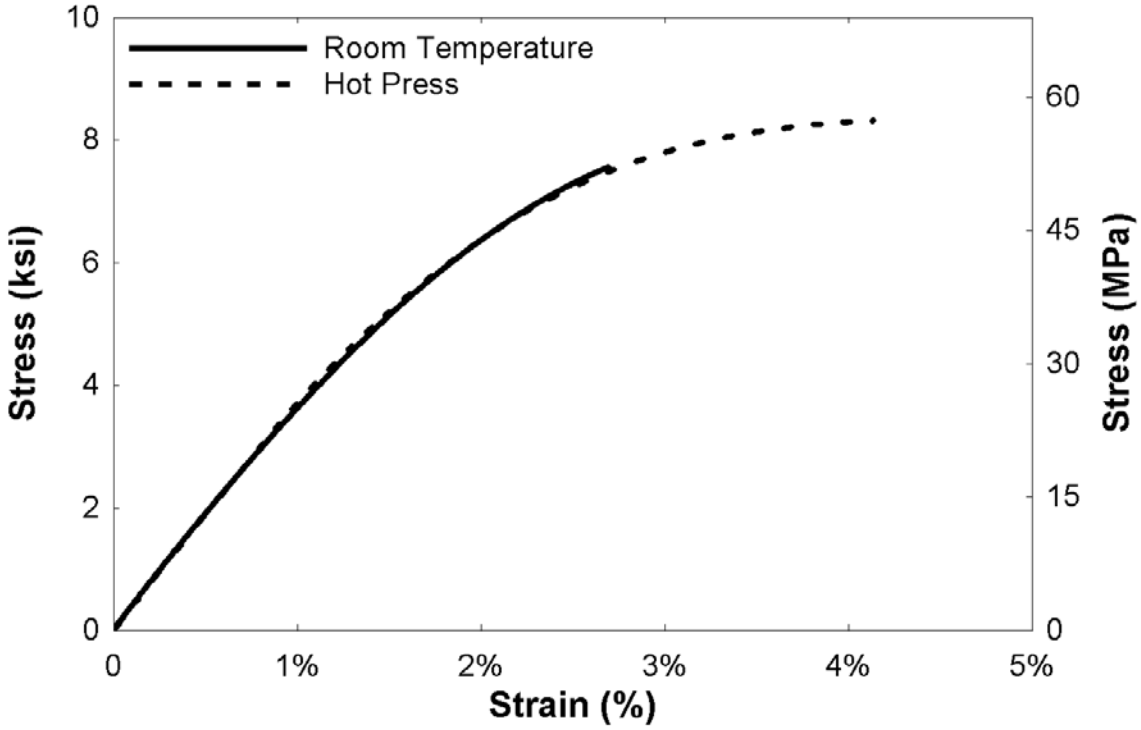

Figure 2-8 Stress-strain relationship of EPON 828 under different curing conditions

2.3 Reinforcement

Both non-metal and metal composite reinforcement was studied for the incorporation into hybrid composites. The non-metal reinforcement type was continuous E-CR glass fibers. The metal reinforcement studied included 1) continuous stainless steel fibers, 2) fine wire steel mesh, and 3) thin perforated steel sheets. The reinforcement mechanical properties were studied through epoxy matrix composites to observe how the hybrid constituents will behave. These composites also served as a baseline against the hybrid composites and the results will be

compared in Chapter Four. Table 2-4 presents a summary of the non-hybrid composites manufactured. Monolithic tensile testing was performed as ultimate strength and failure strain were of interest in this investigation. Open-hole monolithic and half-cyclic tensile testing was performed to study the vulnerability of the composites to stress concentrations. Both open-hole monolithic and half-cyclic tensile testing were conducted.

Table 2-4 Breakdown of Manufactured and Tested Non-hybrid Composites

Composite	Total specimens	Tensile specimens	Open-hole monolithic tensile specimens	Open-hole half-cyclic tensile specimens
UD Glass	6	4	1	1
UD Steel Fiber	8	4	2	2
Steel Mesh	6	4	1	1
Perforated Steel	4	2	1	1

2.3.1 Reinforcement Types

2.3.1.1 Non-metal Reinforcement

Figure 2-9 depicts the nonmetal reinforcement, a quasi-UD woven roving consisting of continuous Advantex® E-CR glass fibers in the warp (0°) direction provided by Owens Corning. These fibers combine the benefits of typical electrical grade E-glass and the corrosion resistance of C-R glass. On average, 98% of the fibers are in the warp direction, thus the fibers in the weft (90°) direction are only present to bind the fiber bundles together and do not contribute to the mechanical properties. The fabric has an areal density of 9.6 oz/yd^3 (327 g/m^2). Per the manufacturer, the glass fibers have an average diameter of 10μm, density of 2.62 g/cm^3, and young's modulus of 82 GPa. Advantex® is a boron-free, material that is recommended for use in acidic environments.

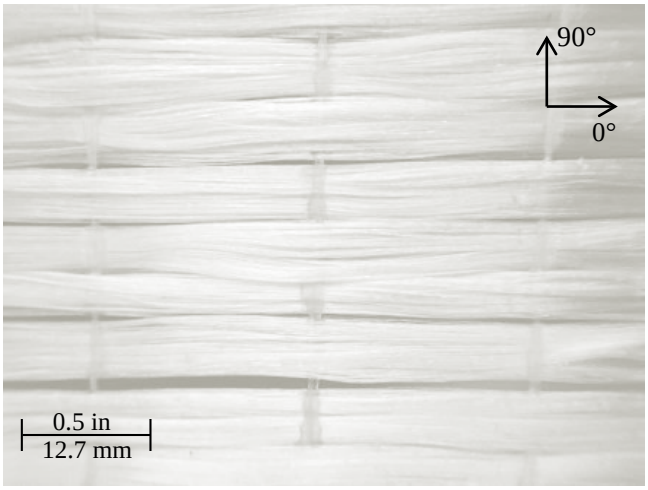

Figure 2-9 Unidirectional glass fibers

2.3.1.2 Metal Reinforcement

Figure 2-10 presents the three types of metal reinforcement. These forms of reinforcement were chosen in an effort to obtain composite homogeneity through complete embedment in the matrix, as opposed to FMLs. This is important for materials exposed to harsh environmental conditions.

The first type of metal reinforcement studied was a quasi-UD weave consisting of stainless steel fibers (Fig. 2-10a) in the warp direction and white polyethylene succinate (PES) cross yarns to hold the weave together provided by N.V. Bekaert S.A. (Belgium) [10]. The steel fibers have a diameter of 30μm and are made of a 316 stainless steel alloy. The density of the fibers is 7.87 g/cm^3 and a young's modulus of 193 GPa, per the manufacturer. The PES fiber has an average diameter of 15μm and the contribution to the mechanical properties of the fabric is negligible. The weave has an areal density of 16.8 oz/yd^3 (570 g/m^2). Bekaert manufactured these fibers using a bundle drawing technique [32] and annealing at >1472°F (800 °C) to ensure high strain-to-failure without compromising stiffness. In this patented bundle drawing process, several copper-coated wires are first bundled into a tube which is drawn through a die to further reduce its diameter. The covering tube and copper are then dissolved in acid, resulting in

individual long ultra-thin metal fibers. The exact chemical composition of the stainless steel was determined using Inductively Coupled Plasma (ICP) Spectrometry and can be seen in the Table 2-5. These fibers were then woven into a fabric as received. Currently, this particular fiber fabric has limited industry application, if any. It was first manufactured for research purposes.

Table 2-5 UD steel fiber chemical composition (provided by Bekaert)

Fe	Cr	Ni	Mo	Mn	Si	Cu	V	Co
65.4%	20.2%	10.5%	2.4%	0.57%	0.49%	0.17%	0.14%	0.10%

The second type of metal reinforcement studied was a plain fine wire 0°/90° mesh (Fig. 2-10b) consisting of 304 stainless steel wire. This particular mesh size is 30×30, indicating the amount of openings per square inch. The mesh has an areal density of 35.5 oz/yd^3 (1204 g/m^2) and an open area of 40.8%. The fine wire has a diameter of 0.012 in (300μm).

The third type of metal reinforcement studied was a thin perforated steel sheet (Fig. 2-10c). This sheet is made of 22-gauge cold rolled steel. The holes are staggered with a 0.109-in (2.77-mm) center-to-center spacing and have a diameter of 0.078 in (1.98 mm). The open area is 45% and has a sheet thickness of 0.03 in (0.76 mm). This perforated steel sheet may act as a 0°/90° type reinforcement as well.

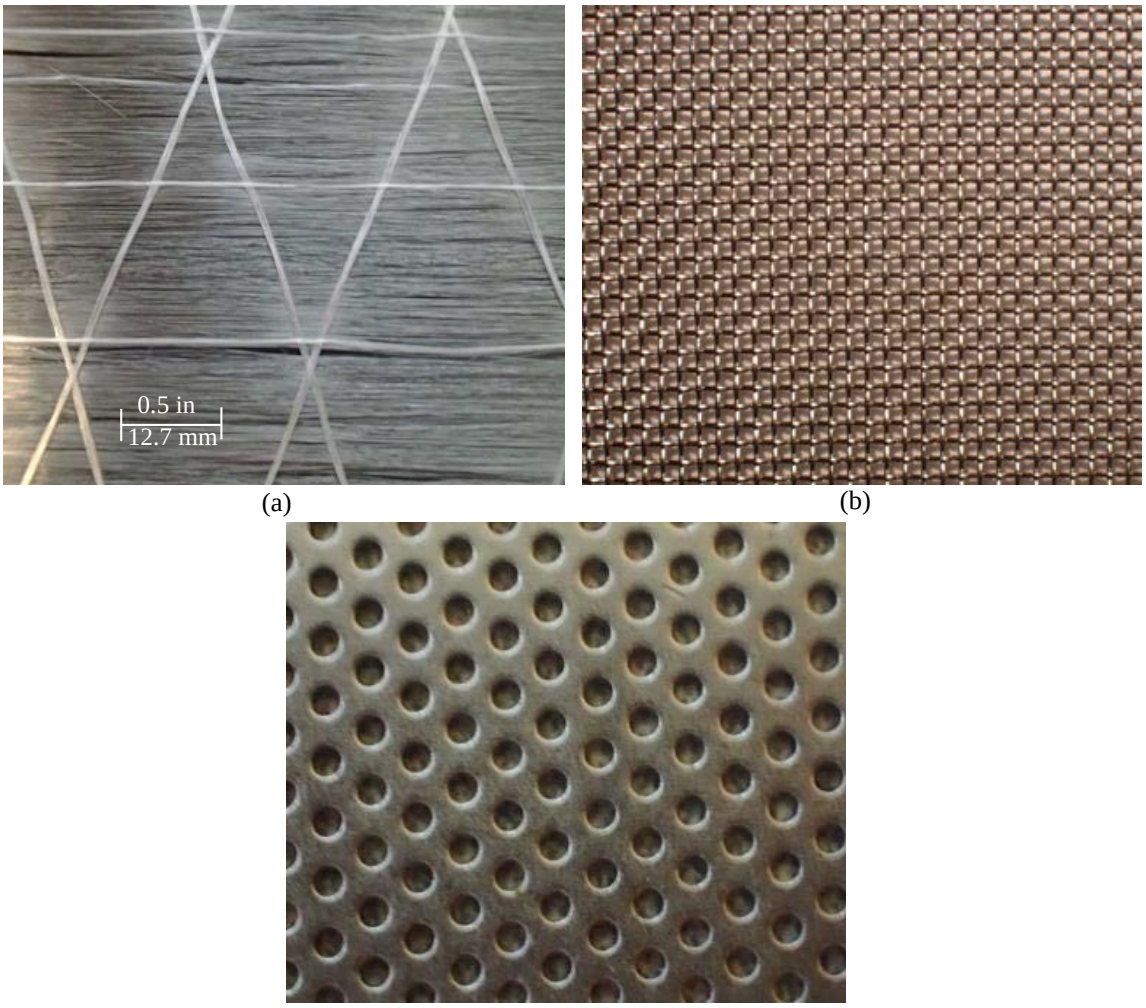

Figure 2-10 Metal reinforcement types
(a) Unidirectional thin stainless steel fibers, (b) Fine wire steel mesh, (c) Thin perforated steel sheet

2.3.2 Manufacturing of Specimens

A mold was designed for the composite plates to be manufactured in. The design of the mold allowed for repeated use, flexibility in reinforcement lay-up, and easy cleaning. It consisted of (2) 12”×12” steel plates and a frame with a thickness matching the design thickness of the composite plate, 0.07” (1.8 mm). The frame was machined with tight tolerances for consistent manufacturing. The top plate had notched corners to allow for leverage upon removing the plate from the mold as highlighted in Fig. 2-11a. The bottom plate had release hex screws that allowed for additional separation of the frame from the plate using an Allen wrench (not pictured). The frame border was 1 inch wide, thus the composite plates were 10”×10”. A

notch was etched into the frame as displayed in Fig. 2-11b to allow excess epoxy to flow out under applied pressure during curing.

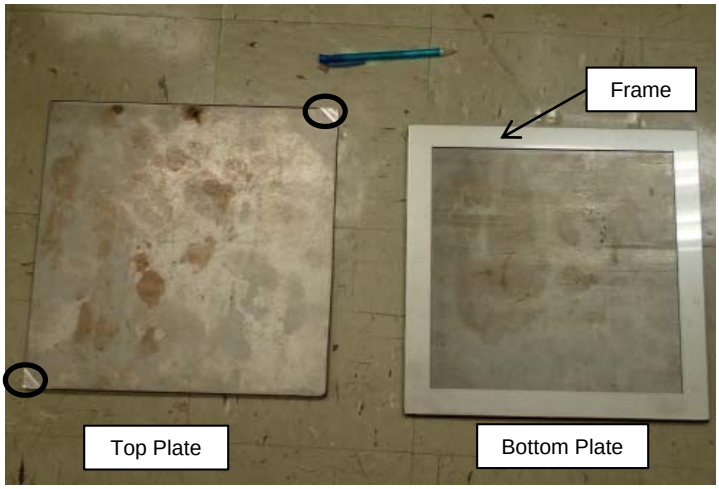

(a)

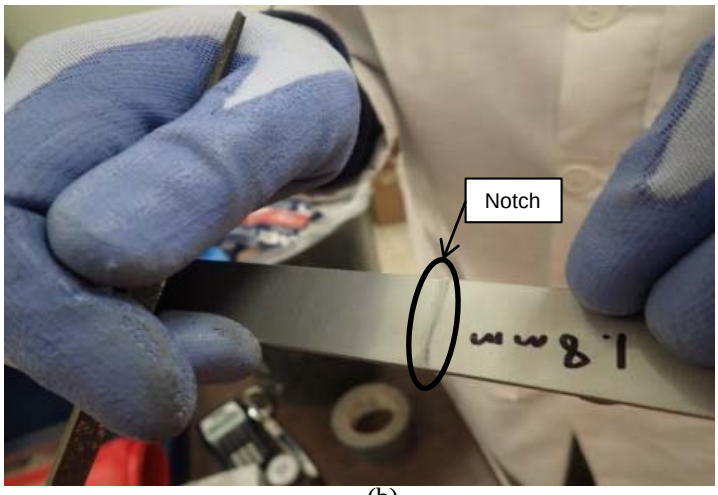

(b)

Figure 2-11 Composite plate manufacturing
(a) Composite plate mold; (b) Notched frame

Before the manufacturing process began, the reinforcement had to be cut to size in order to fit in the mold. The UD glass fiber fabric was on a 36-in wide roll (Fig. 2-12a-b). The UD steel fiber fabric was on a 22-in wide roll (Fig. 2-12c-d). The steel mesh (Fig. 2-12e) and perforated steel (Fig. 2-12f) were also cut to size from larger sheets. The amount of reinforcement to cut was determined by volume fraction calculations, seen in Table 2-6.

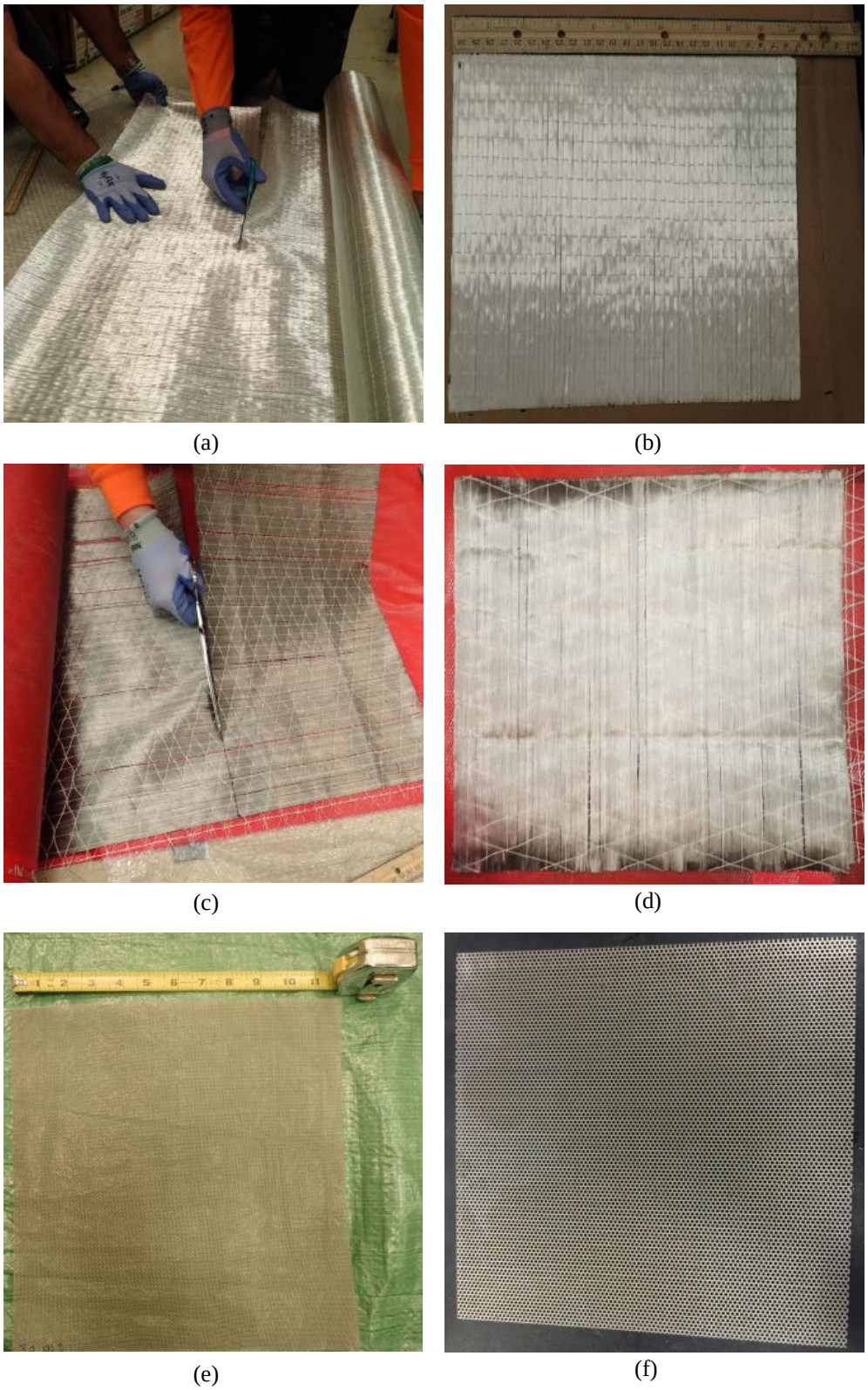

(a) (b)

(c) (d)

(e) (f)

Figure 2-12 Cutting reinforcement types
(a) UD glass fiber roll; (b) Glass fiber fabric cut to size; (c) UD steel fiber roll; (d) Steel fiber cut to size; (e) Steel mesh cut to size; (f) Perforated steel cut to size

The mold was thoroughly cleaned with acetone before each use (Fig. 2-13a). Sprayon® thin film release spray was applied to the plates and frame to allow for easy removal of the composite plate after curing (Fig. 2-13b). EPON 828 epoxy resin was mixed with EPIKURE 3055 hardener as described in Section 2.2.2 (Fig. 2-13c). Unlike the resin dogbone specimens, for composite manufacturing, the resin was not placed in a vacuum oven to de-gas. This decision was made based on the manufacturing process and the potential application in large-scale structures. In wetting the fibers during hand lay-up, air bubbles would become inevitable. The epoxy was instead mixed slowly and thoroughly to avoid creating large air pockets.

The reinforcement was then oriented on the mold within the frame to be saturated with epoxy as shown in Fig. 2-13d. Using the volume of the mold and desired volume fraction, the volume of epoxy needed was calculated. The epoxy was carefully injected using syringes and was spread evenly around and in between layers using spatulas and rollers. An excess of epoxy was added in order to ensure full saturation. The top of the mold was then closed. The composite plates were cured using the compression molding technique. Aluminum foil lined the hot press to avoid any epoxy spillage. Curing was executed at 200°F (93°C) for 2 hours as per the manufacturer's recommendation and under a pressure of 104 psi (7 bars) in order for the excess resin to bleed out while reaching the desired thickness (Fig. 2-13e). The plates were then cooled for approximately 30 minutes under no pressure before removal from the frame. Figure 2-13f depicts a completed UD glass fiber/epoxy composite plate. The same procedure was followed for the UD steel fiber, steel mesh, and perforated steel composite plates.

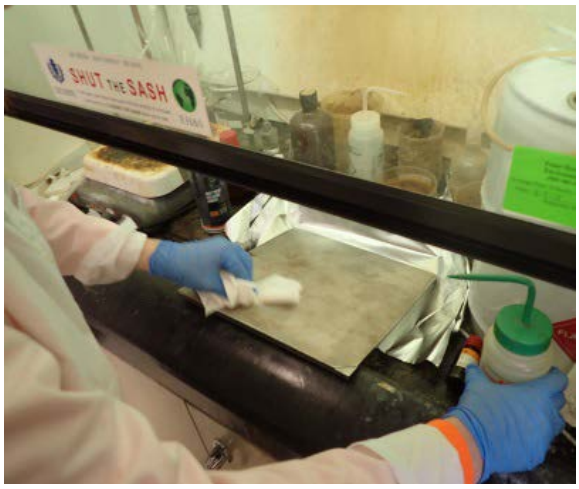

(a)

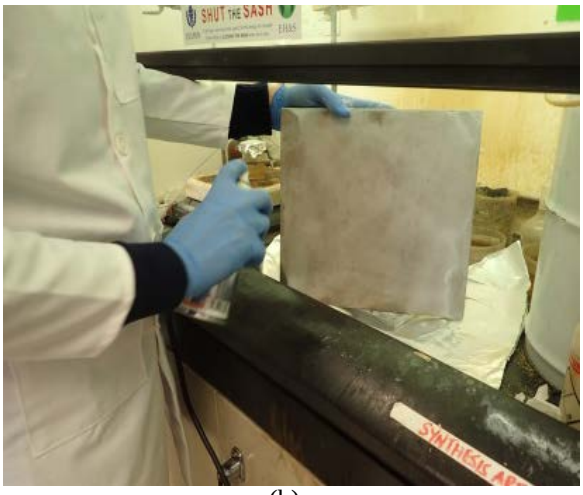

(b)

(c)

(d)

(e)

(f)

Figure 2-13 Non-hybrid composite plate manufacturing process
(a) Cleaning mold with acetone, (b) Applying mold release spray, (c) Mixing epoxy, (d) Orienting fibers and injecting epoxy, (e) Plate curing in hot press, (f) Complete UD glass/epoxy composite plate

E-glass fibers are well known to have a strong bond with epoxy and thus allows for complete stress transfer from the matrix to the elastic reinforcement. However, a hypothesis was tested to see if inelastic steel fibers should have a weaker bond with the resin to allow for debonding and yielding of the fibers. As one of the ultimate goals of this hybrid composite is ductility, the maximum yielding potential of the steel was desired. To test this hypothesis, CRC Silicone mold release agent was applied to the steel fibers and mesh (not perforated sheet) before being embedded in the epoxy (Fig. 2-14a-b). Just as the spray allows the release of epoxy from the steel mold, the same concept was applied to the steel reinforcement.

As the UD steel fiber and mesh composites were manufactured, it was split in half within the mold. One half of the composite contained bonded reinforcement and the other half contained silicone-coated debonded reinforcement. Two different spatulas were used to spread the epoxy to keep the two sides clear from contamination as shown in Fig. 2-14c and 2-14d.

(a) (b)

(c) (d)

Figure 2-14 Application of debonding agent to steel fibers
(a) CRC Silicone Mold Release Spray; (b) Applying silicone to steel fibers; (c) Manufacturing UD steel fiber composite with one bonded half and one debonded half; (d) Complete UD steel composite plate

After manufacturing was complete, 2-inch G10 fiberglass beveled end tabs were applied using Loctite 4014 instant adhesive (Fig. 2-15a-b). This was a medical grade, instant cure adhesive. The edges of the plates were sanded down to provide a rougher surface for the adhesive used for attachment. The end tabs were necessary to avoid premature failure due to stress concentrations at the testing grips. The plates were then cut into 1-inch (25.4-mm) wide by 10-inch long coupons using a water-jet tile saw with a carbide blade (Fig. 2-15c). A hole was drilled in the direct center of the specimens specified in Table 2-4 with a diameter equal to $\frac{1}{6}$ of

the coupon width, per ASTM specifications. Prior to testing, specimens were inspected to ensure there was no damage surrounding the hole. A complete schematic of coupon dimensions is provided in Fig. 2-15d. Each composite type was given an alphabetical letter and each sample a number for simplicity in the lab. For example, UD Glass was given the letter 'A' and each sample of this composite type was labeled A1, A2, etc. Each metal composite type with debonded fibers was given a different letter than its bonded counterpart. The order of the letters represents the order in which the plates were manufactured and do not represent any other significant meaning.

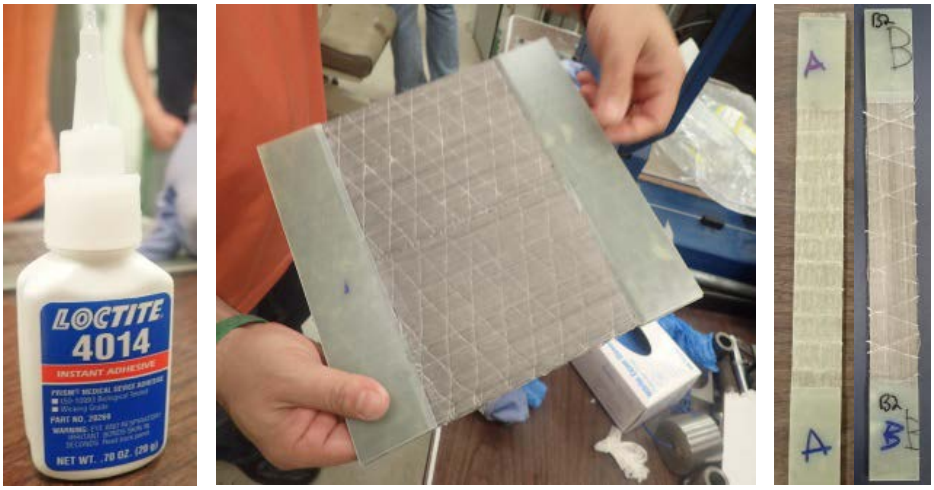

(a) (b) (c)

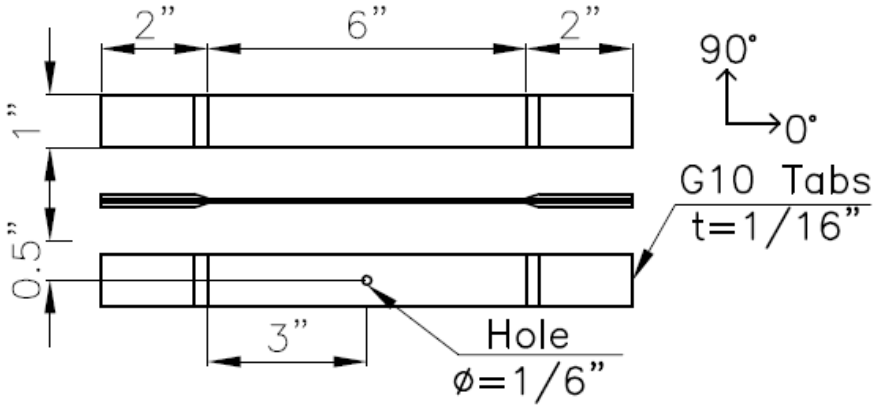

(d)

Figure 2-15 Preparation of specimens for testing
(a) Loctite 4014 instant adhesive; (b) Applying G10 end tabs; (c) Composite coupons; (d) Coupon dimensions

The composites were designed so that the total reinforcement volume fractions (v_f), and thus the results, were comparable. Table 2-6 presents a summary of the volume fractions of the non-hybrid composites manufactured in this study. The layer notation is as follows: G = glass fiber, S = steel fiber, M = steel mesh and P = perforated steel. As all continuous fibers were oriented in the 0° direction, the fiber direction is omitted from the layer notation. For the purpose of this study, all loading was in the 0° direction. In the non-hybrid composites, repeated layers are shown using subscripts. For example, $[G]_5$ represents 5 layers of UD glass fiber fabric. The lab letter notation is also listed in the table. The UD steel fiber and steel mesh composites have both bonded and debonded letters, respectively. The targeted volume fractions were determined based on the composite thickness, material density, and fabric areal density using Equation 2.1,

$$v_f = \frac{n*A_w}{\rho*t} \quad \text{(Eq. 2.1)}$$

where n = number of reinforcement layers; A_w = the areal weight of the reinforcement; ρ = reinforcement density; t = composite thickness. The perforated steel volume fraction was calculated using the open area percentage. The matrix volume, v_m, needed for each plate was calculated using Equation 2.2.

$$v_m = 1 - v_f \quad \text{(Eq. 2.2)}$$

After the composite coupons were cut, measurements were recorded. The volume fractions were recalculated based on the actual thickness of each specimen. The averages are presented in Table 2-6.

Table 2-6 Manufactured Non-hybrid Composites

Non-Hybrid Composite Type	Lab Letter Notation	Layer Notation	Glass Fraction	Steel Fraction	Total Volume Fraction
UD Glass	A	$[G]_5$	34.7 ± 0.1%	--	34.7 ± 0.1%
UD Steel Fiber	B,C	$[S]_8$	--	30.9 ± 0.5%	30.9 ± 0.5%
Steel Mesh	N,P	$[M]_4$	--	28.8 ± 0.5%	28.8 ± 0.5%
Perforated Steel	T	$[P]_1$	--	21.6 ± 0.1%	21.6 ± 0.1%

2.3.3 Experimental Methodology

Composite coupons were first tested under monolithic tensile loading in order to observe the ultimate tensile strength (σ_{ult}) and failure strain (ε_{ult}) of different non-hybrid composites. The testing was conducted on a hydraulic MTS 810 test machine (Fig. 2-16a) and performed according to ASTM D3039 *Standard Test Method for Tensile Properties of Polymer Matrix Composite Materials*. The displacement was applied at 0.078 in/min (2 mm/min), the load was recorded using a 20-kip load cell, and the longitudinal strain was measured using a strain-gauge based extensometer with a 4-inch (102 mm) gauge length and a 350-Ω resistance (Fig. 2-16b). Failure inside the gauge length, away from the grips, was successfully achieved in nearly all specimens. A schematic of a tensile test is shown in Fig. 2-16c.

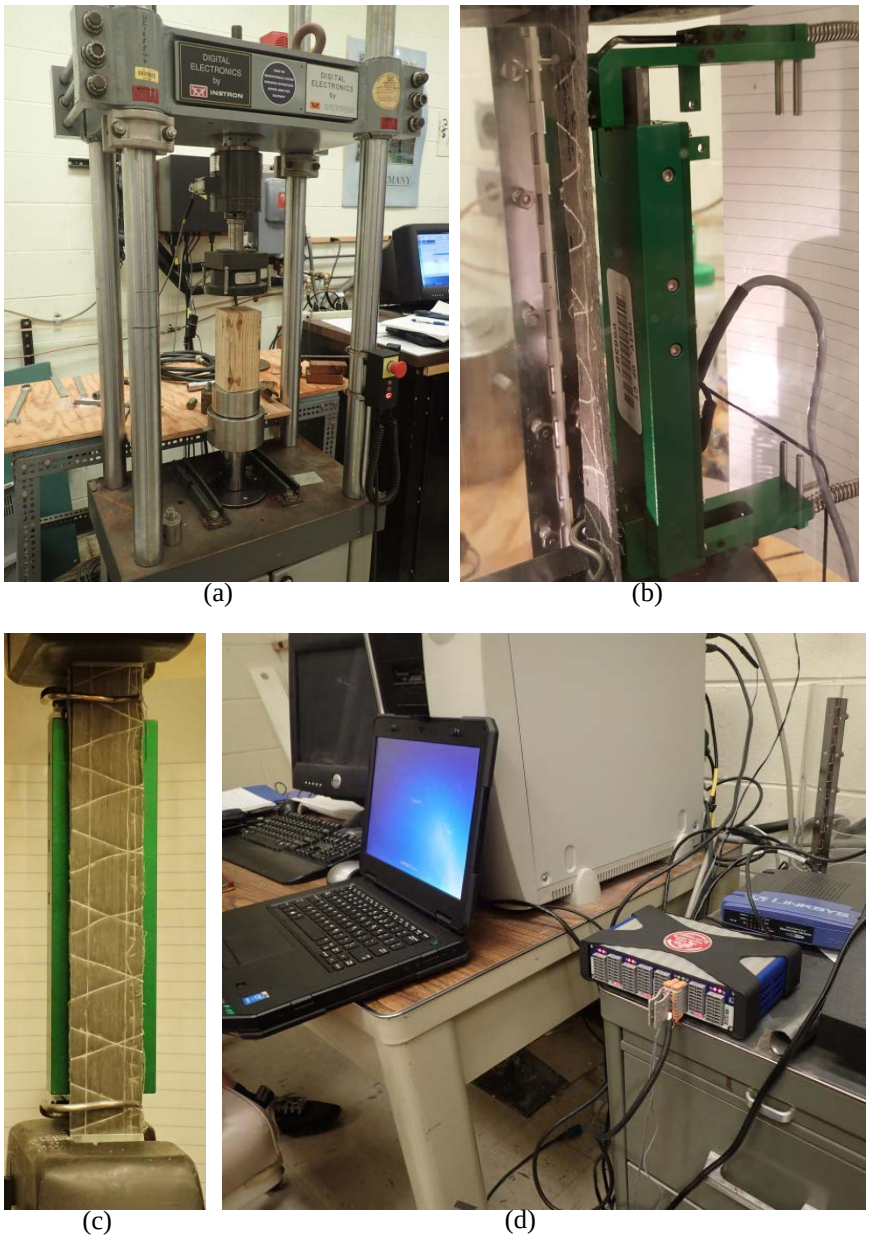

(a) (b)

(c) (d)

Figure 2-16 Composite Tensile Testing
(a) MTS 810 Testing Machine, (b) 4-inch gauge extensometer, (c) Tensile specimen testing setup, (d) HBM Data Acquisition System

In order to explore energy dissipation and re-centering capabilities of this hybrid material, open-hole monolithic and half-cyclic tensile tests were performed on specimens. The open hole simulates realistic stress concentrations that can be found in the material due to bolt holes for structural connections or general accumulated damage. First, monolithic open-hole tensile (OHT) testing was performed on each coupon according to ASTM D5766 *Standard Test*

Method for Open-Hole Tensile Strength of Polymer Matrix Composite Laminates to obtain the open-hole ultimate tensile strength. Per the standard, this is calculated using the gross cross-sectional area, disregarding the presence of the hole. The true strength (σ_{true}) was calculated adjusting for reduced area. Next, open-hole half-cyclic (OHC) tensile testing was performed. The loading protocol began and returned to a benchmark of 100 lbs as the applied load was increased by $0.1\sigma_{ult}$ (σ_{ult} found in the OHT tests) for each cycle at a constant load rate of 25 lb/s until failure (Fig. 2-17). All data output was collected via an HBM data acquisition system (Fig. 2-16d). All tests were conducted under standard laboratory conditions (73.4 ± 3.6°F).

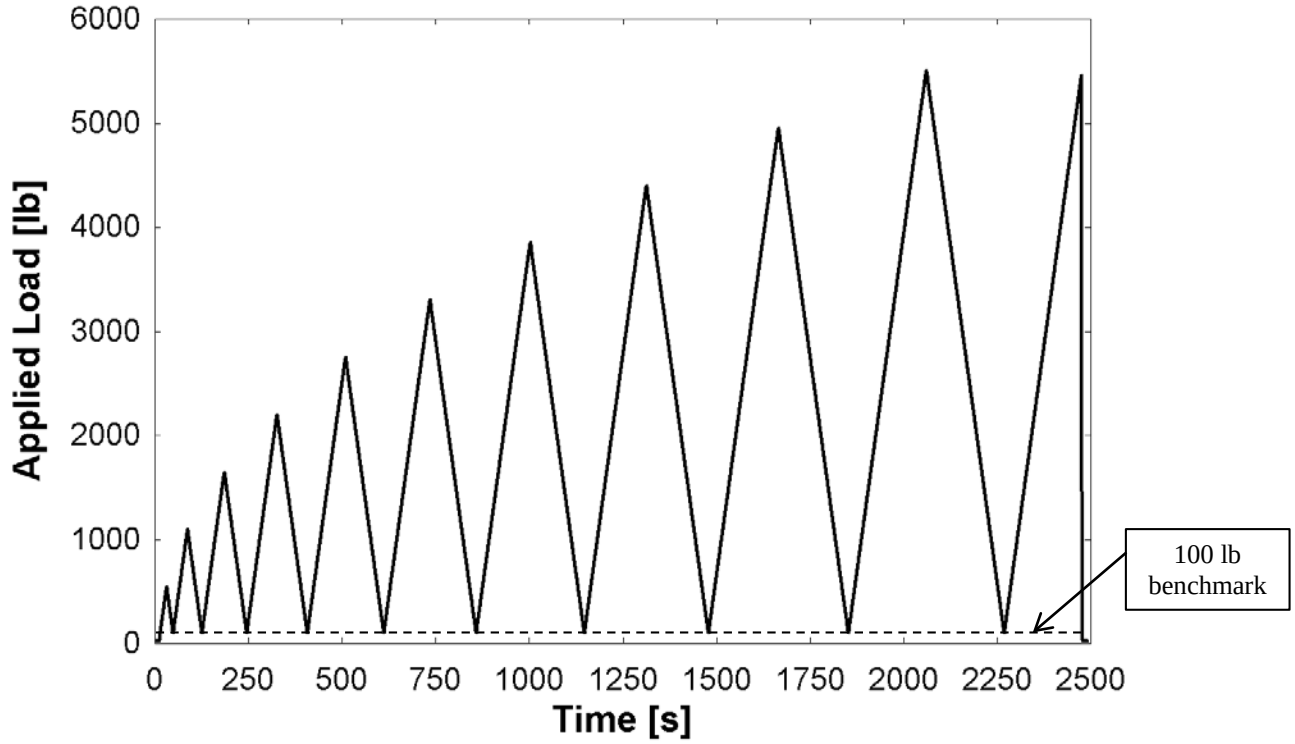

Figure 2-17 Example Loading Protocol for open-hole half-cyclic tensile (OHC) testing

2.3.4 Results and Observations

Average results of non-hybrid monolithic and half-cyclic tensile tests are presented in Table 2-7. Figures 2-18, 2-19, 2-20, and 2-21 present the stress-strain relationships of the

respective non-hybrid composites under monolithic tension, open-hole tension (OHT) and open-hole half-cyclic (OHC) testing.

Table 2-7 Results of no-hole and open-hole monolithic and half-cyclic tensile testing of non-hybrid composites

	No-Hole		Open-Hole Tension				Open-Hole Cyclic	
Composite	σ_{ult}, ksi (MPa)	ε_{ult}	σ_{ult}, ksi (MPa)	ε_{ult}	σ_{true}, MPa (ksi)	$\frac{\sigma_{true}}{\sigma_{ult,no\ hole}}$	σ_{ult}, ksi (MPa)	ε_{ult}
$[G]_5$	96.8 (667.4)	2.50%	68.7 (473.8)	2.55%	82.5 (568.6)	0.852	65.9 (454.7)	2.46%
$[S]_8$	27.0 (186.2)	12.03%	23.4 (161.1)	4.50%	27.0 (186.2)	1.000	24.5 (168.9)	3.32%
$[M]_4$	15.3 (105.5)	3.75%	12.7 (87.3)	1.90%	15.2 (104.9)	0.994	12.7 (87.3)	1.90%
$[P]_1$	7.5 (51.9)	0.83%	6.2 (42.6)	0.79%	7.4 (50.8)	0.978	6.2 (42.7)	0.42%

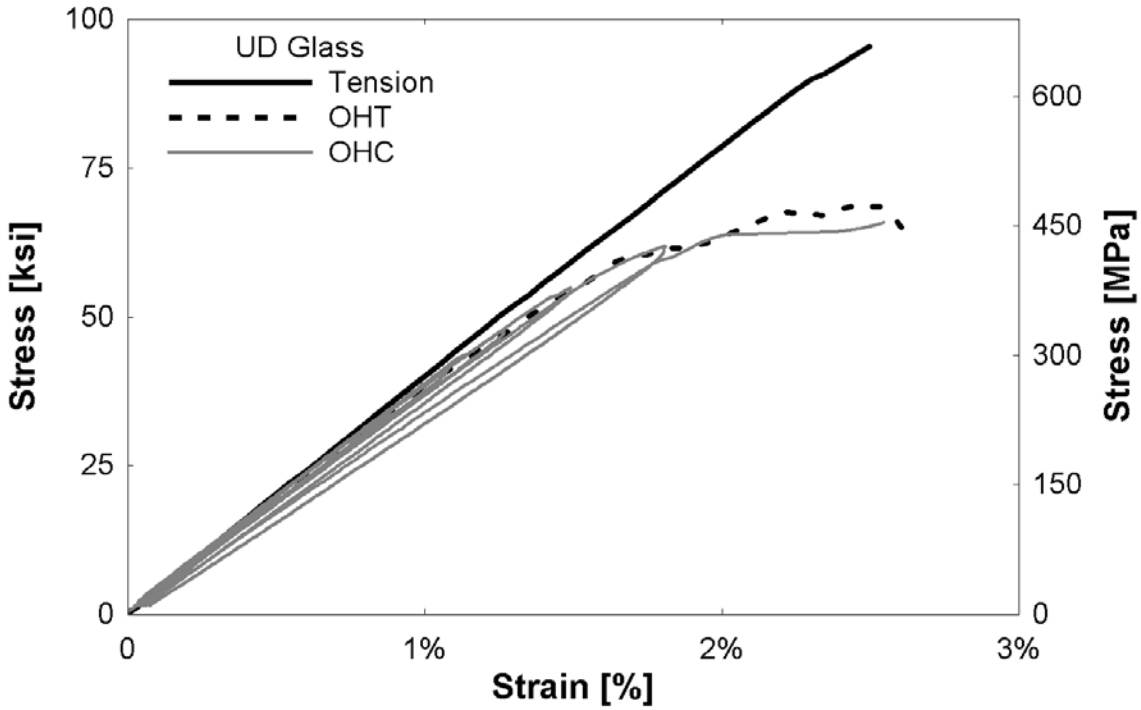

Figure 2-18 UD Glass composite $[G]_5$ no-hole monolithic tensile, open-hole tensile (OHT), and open-hole half-cyclic (OHC) testing stress-strain relationships

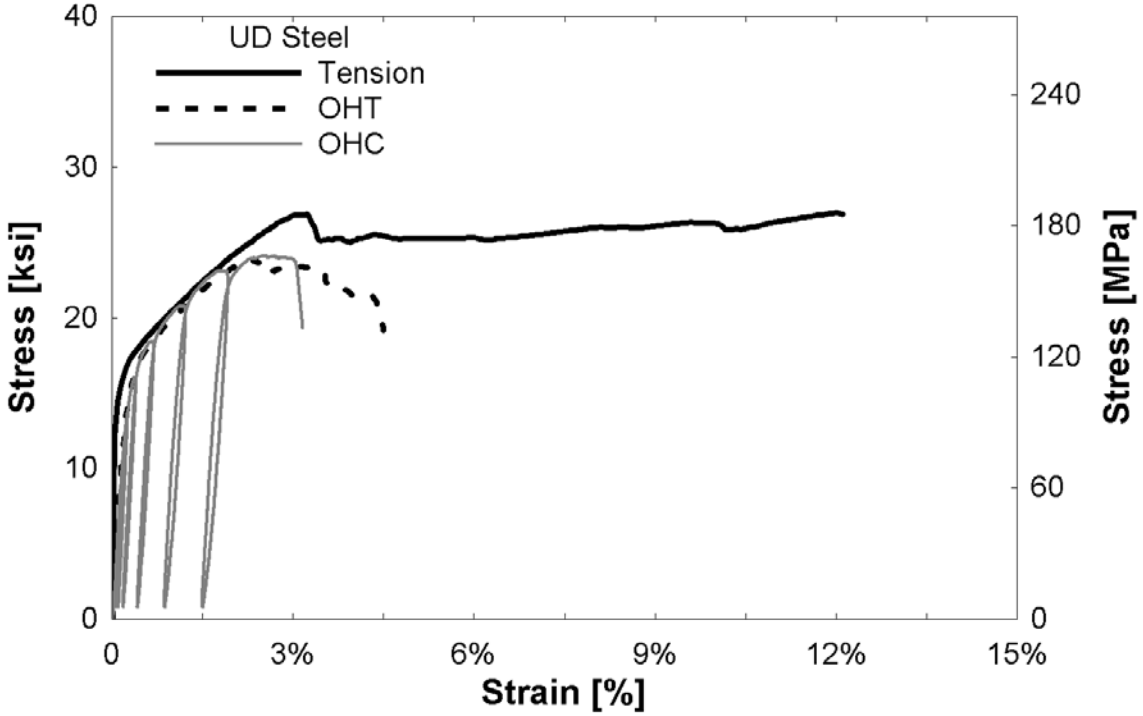

Figure 2-19 UD Steel composite $[S]_8$ no-hole monolithic tensile, open-hole tensile (OHT), and open-hole half-cyclic (OHC) testing stress-strain relationships

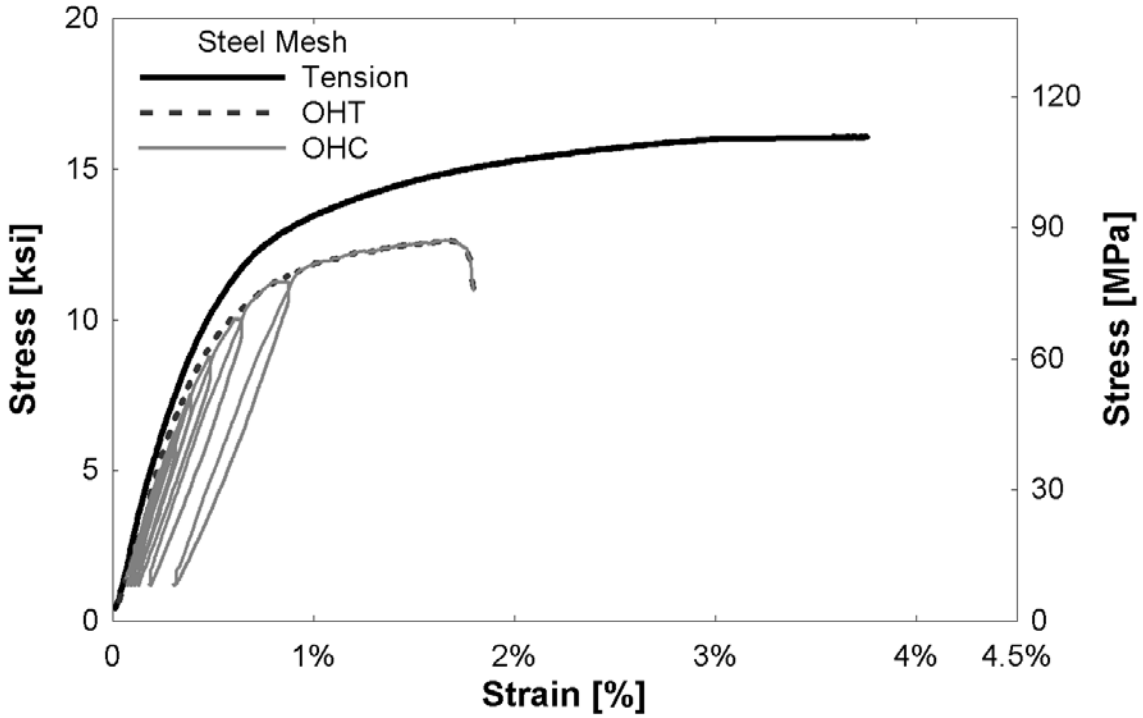

Figure 2-20 Steel Mesh $[M]_4$ composite no-hole monolithic tensile, open-hole tensile (OHT), and open-hole half-cyclic (OHC) testing stress-strain relationships

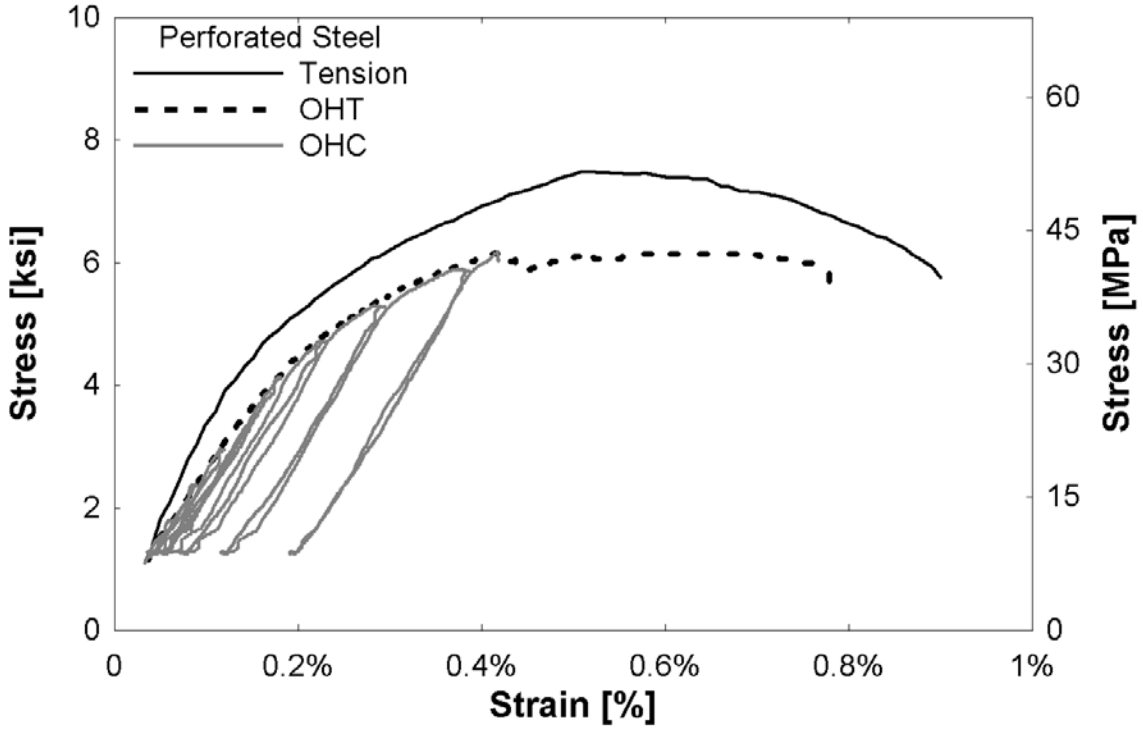

Figure 2-21 Perforated Steel $[P]_1$ composite no-hole monolithic tensile, open-hole tensile (OHT), and open-hole half-cyclic (OHC) testing stress-strain relationships

After analyzing all data, it was realized that the specimens including the debonded steel reinforcement did not show any significant results to the bonded steel specimens. Therefore, the bonded and debonded specimens were averaged together to yield the final results. More research is needed to study the role of fiber-matrix bonding for metal reinforcement.

The UD glass composite, $[G]_5$, had the highest ultimate strength at 96.8 ksi (667.4 MPa) and a failure strain of 2.50%. The UD steel fiber composite performed the best out of the metal reinforcement. The UD steel fiber composite, $[S]_8$, had a significantly higher failure strain of 12.03%, and ultimate strength of 27 ksi (186.2 MPa). The mesh composite, $[M]_4$, and the perforated steel composite, $[P]_1$, had significantly lower ultimate strengths at 15.3 ksi (105.5 MPa) and 7.5 ksi (51.9 MPa), respectively. For the two latter composites, it is realized that only half of the reinforcement is in the direction of loading, and thus contributing to the axial tensile

performance. Figure 2-22 presents a comparison of all non-hybrid composites under monolithic tension (no-hole).

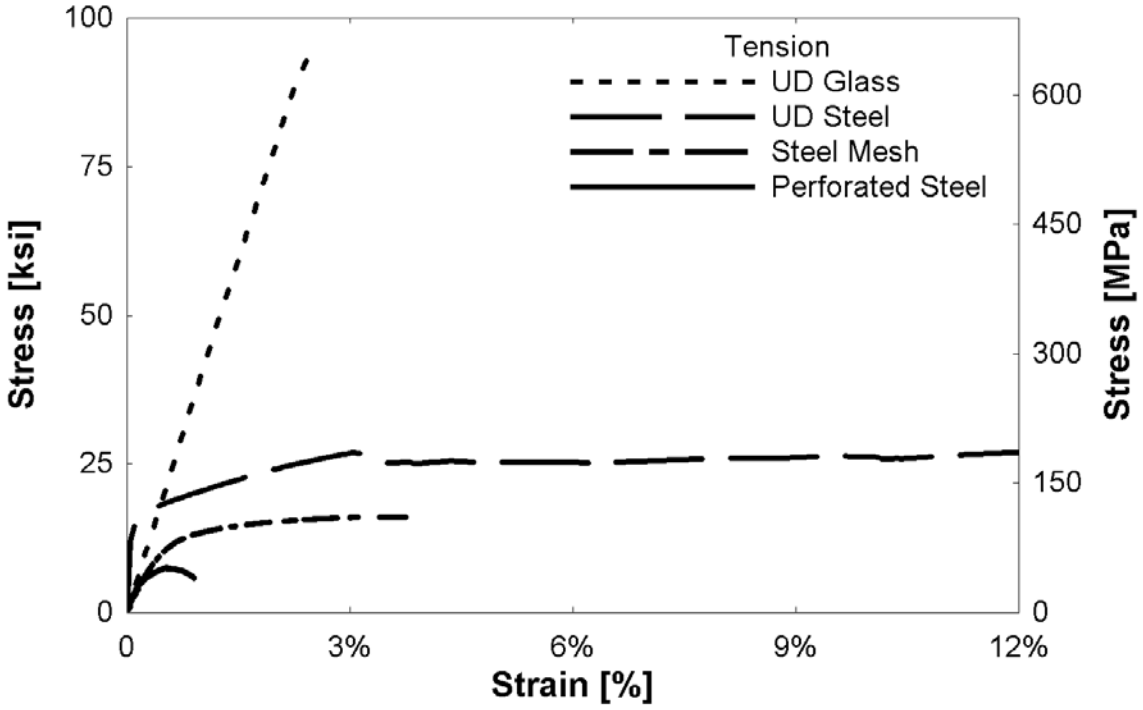

Figure 2-22 Non-hybrid no-hole composite monolithic tensile testing stress-strain relationships

Figure 2-23 presents a comparison of no-hole vs. open-hole monolithic tensile stress-strain relationships. It can be seen that the presence of a hole in the specimen lowered the ultimate strength. The $[G]_5$ specimen displayed the largest decrease. As per ASTM, the open-hole ultimate strength is calculated with the gross cross-sectional area. The true stress was calculated with the net cross-sectional area and a ratio was found. It is reflected in the ratios that the UD glass specimen showed the largest vulnerability to a stress concentration. The steel helped retain more strength; this may be beneficial when incorporating into hybrid composites. There also exists a decrease in failure strain, most notably in the $[S]_8$ composite, as the failure was more localized to the location of the hole.

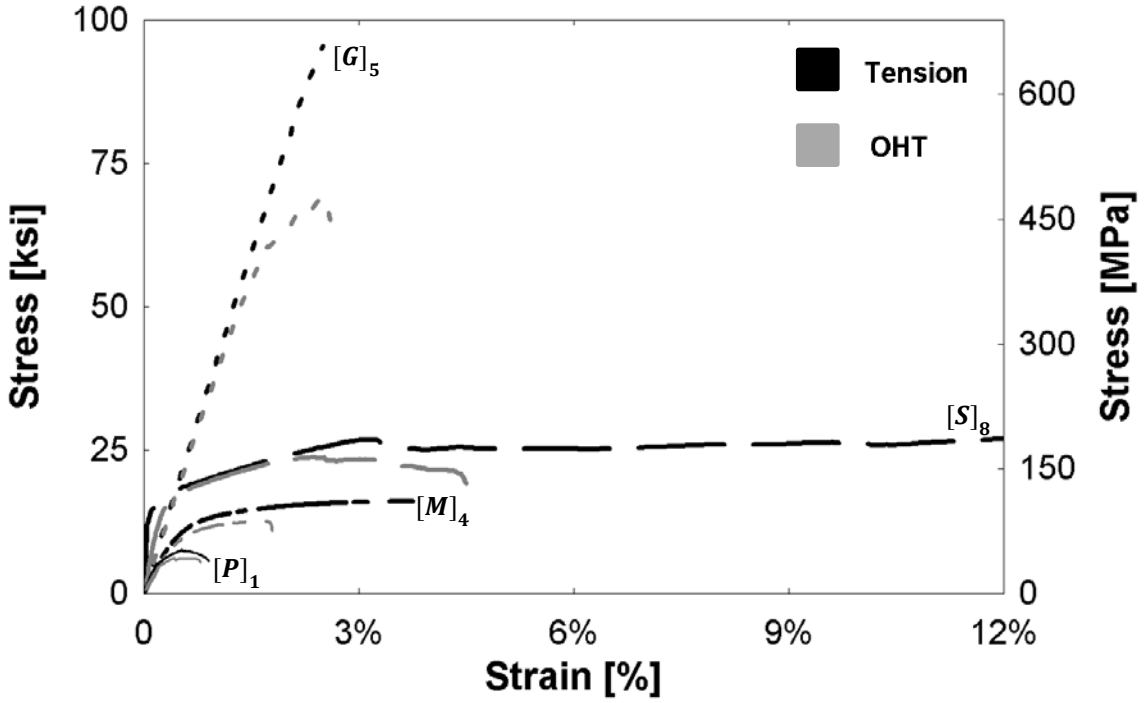

Figure 2-23 Non-hybrid no-hole vs. hole composite monolithic tensile testing stress-strain relationships

Figure 2-24 presents a comparison of open-hole monolithic vs. half-cyclic tensile stress-strain relationships. The backbones of the cyclic curves are presented. The OHT tests were displacement-controlled and the OHC tests were load-controlled. The strengths were comparable between the two tests. It can be seen that the presence of damage, or the prior cycles of loading and unloading, does not have a large effect on the composite behavior. This is beneficial in structural elements subjected to continuous loading and unloading. It displays a level of fatigue resistance.

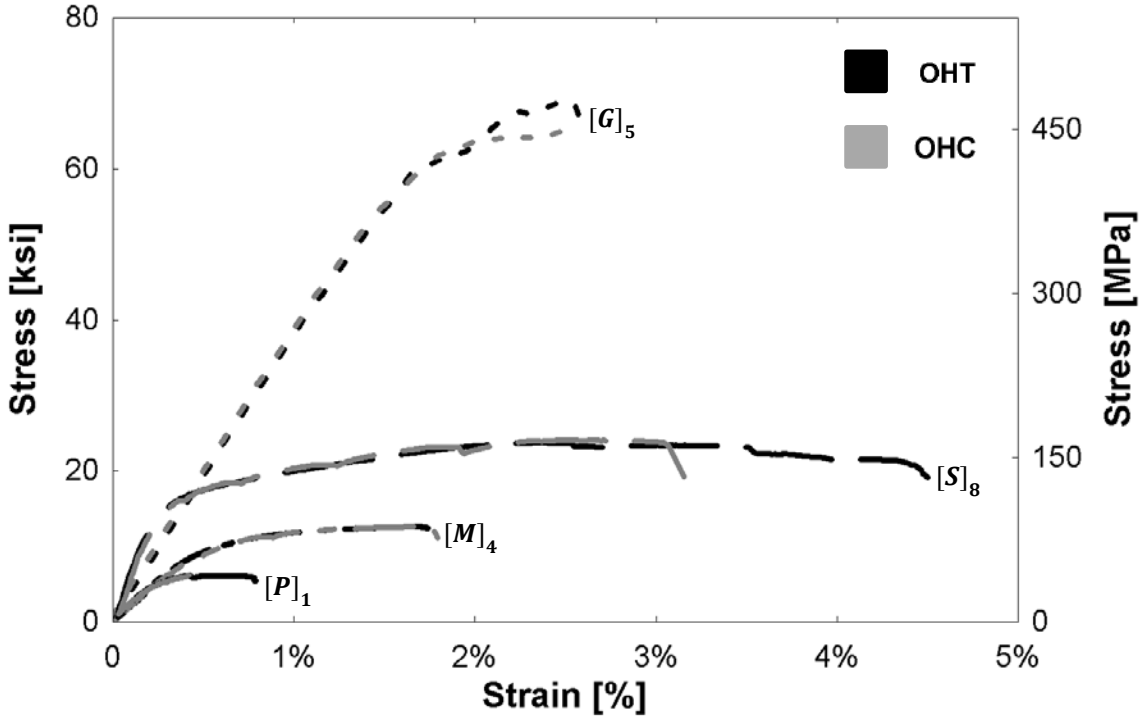

Figure 2-24 Non-hybrid composite open-hole monolithic vs. half-cyclic tensile testing stress-strain relationships

3 CHAPTER THREE – HYBRID COMPOSITES

3.1 Introduction

The metal-nonmetal hybrid composite tests performed as part of this study are detailed within this chapter. This chapter will describe the research design considerations, materials used, specimen manufacturing process, test setup, loading protocols, and experimental results of the hybrid composites.

3.2 Research Methodology

Both the non-metal and metal composite reinforcement discussed in the Chapter Two will be combined for incorporation into hybrid composites. The mechanical properties of five hybrid composites were characterized. Table 3-1 presents a summary of the hybrid composites manufactured and tested. The three fiber-reinforced hybrids were designed to have anticipated glass-to-steel ratios of 70:30 [SGGGGS], 50:50 [SGSGSGS], and 30:70 [SSSGSSS]. The anticipated mesh and perforated steel glass-to-steel ratios were 50:50. The overall fiber fractions were kept relatively close in order to compare results. Monolithic tensile testing was performed as ultimate strength and failure strain were of interest in this investigation. Open-hole testing was performed to study the vulnerability of the composites to stress concentrations. Both open-hole monolithic and half-cyclic tensile testing were conducted.

Table 3-1 Breakdown of Manufactured and Tested Hybrid Composites

Composite	Total specimens	Anticipated Fiber Ratio		Tensile specimens	Open-hole monolithic tensile specimens	Open hole half-cyclic tensile specimens
		Glass	Steel			
Fiber Hybrid 1	6	70	30	2	2	2
Fiber Hybrid 2	8	50	50	4	2	2
Fiber Hybrid 3	8	30	70	4	2	2
Mesh Hybrid	7	50	50	4	2	1
Perforated Hybrid	4	50	50	2	1	1

3.3 Raw Materials

The non-metal and metal reinforcement discussed in Chapter Two along with EPON 828 epoxy comprised the hybrid composites to be discussed herein. Each hybrid composite will comprise of UD glass fibers along with one of the following forms of metal reinforcement: 1) UD steel fibers, 2) fine wire steel mesh, 3) thin perforated steel sheet.

3.4 Manufacturing of Specimens

The same mold discussed in Section 2.3.2 was utilized to manufacture the hybrid composite plates. It produced 10”×10” composite plates with a thickness of 0.07 inches. Before the manufacturing process began, the reinforcement had to be cut to size in order to fit in the mold. The amount of reinforcement to cut was determined by volume fraction calculations as shown in Table 3-2. The layer notation is as follows: G = glass fiber, S = steel fiber, M = steel mesh, and P = perforated steel. The fiber direction is omitted from the layer notation, as they were all unidirectional (0°). The mold was thoroughly cleaned with acetone before each use and mold release spray was applied to the steel plates and frame to allow for easy removal of the composite after curing. EPON 828 epoxy resin was mixed with EPIKURE 3055 hardener as described in Section 2.2.2. For all hybrid composite manufacturing, the resin was not placed in a vacuum oven to de-gas. The reinforcement was then oriented on the steel plate within the frame to be saturated with epoxy. Using the volume of the mold and desired volume fraction, the volume of epoxy needed was calculated.

The lay-ups of the hybrids were chosen to ensure all composites were symmetric so as not to introduce any bending-extension coupling. Edge effects are also less prominent in symmetric composites. However, the impact of lay-up on the mechanical properties was not explicitly studied.

Table 3-2 Manufactured Hybrid Composites

Composite Type	Lab Letter Notation	Layer Notation	Glass Fraction	Steel Fraction	Total Volume Fraction
Fiber Hybrid 1	V	[SGGGGS]	28.2 ± 0.1%	8.2%	36.4 ± 0.1%
Fiber Hybrid 2	D, E	[SGSGSGS]	20.3 ± 0.2%	15.7 ± 0.2%	36.0 ± 0.4%
Fiber Hybrid 3	L, M	[SSSGSSS]	6.5%	22.8 ± 0.1%	29.3 ± 0.2%
UD Glass/Steel Mesh	J, K	[MGGM]	12.5 ± 0.3%	15.1 ± 0.4%	27.6 ± 0.7%
UD Glass/ Perforated Steel	U	[GPG]	12.7%	21.3%	34.0%

The epoxy was carefully injected using syringes and was spread evenly around and in between layers using spatulas and rollers (Fig. 3-1). An excess of epoxy was added in order to ensure full saturation. The top of the mold was then closed. The composite plates were cured using the compression molding technique. Aluminum foil lined the press to avoid any epoxy spillage. Curing was executed at 200°F (93°C) for 2 hours as per the manufacturer's recommendation and under a pressure of 104 psi (7 bars) in order for the excess resin to bleed out while reaching the desired thickness. The plates were then cooled for approximately 30 minutes under no pressure. The same procedure was followed for all hybrid composite plates.

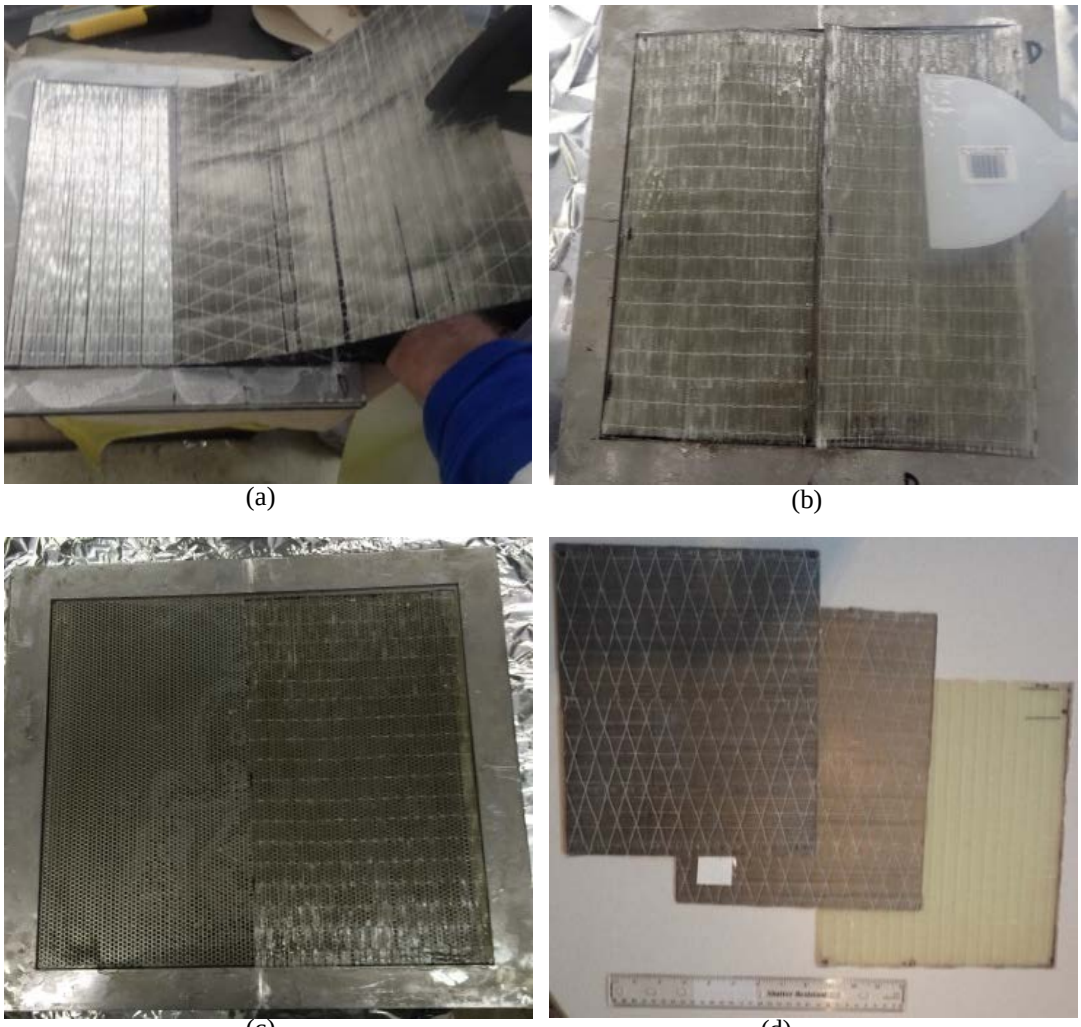

(a) (b)

(c) (d)

Figure 3-1 Manufacturing of hybrid composites
(a) Glass-steel fiber composite; (b) Glass-steel mesh composite; (c) Glass-perforated steel composite; (d) Completed composite plates

The hybrids were subjected to half-plate debonding of steel reinforcement as described in Section 2.3.2. G10 fiberglass beveled end tabs were added and specimens were cut to size as shown in Fig. 2-15d. Holes were drilled in the specimens specified in Table 3-1. All specimen measurements were recorded.

3.5 Experimental Methodology

Hybrid composite coupons were first tested under monolithic tensile loading in order to observe the ultimate tensile strength (σ_{ult}) and failure strain (ε_{ult}). The testing was conducted on a

hydraulic MTS 810 test machine and performed according to ASTM D3039. The displacement was applied at 0.078 in/min (2 mm/min), the load was recorded using a 20-kip load cell, and the longitudinal strain was measured using a strain-gauge based extensometer with a 4-inch (102 mm) gauge length and a 350-Ω resistance. Failure inside the gauge length, away from the grips, was successfully achieved in most specimens.

Monolithic open-hole tensile (OHT) testing was then performed on each coupon according to ASTM D5766 to obtain the open-hole ultimate tensile strength. The true strength (σ_{true}) was calculated adjusting for reduced area. Next, open-hole half-cyclic (OHC) tensile testing was performed. The loading protocol was identical to that of the non-hybrid tests. All data output was collected via an HBM data acquisition system. All tests were conducted under standard laboratory conditions (73.4 ± 3.6°F).

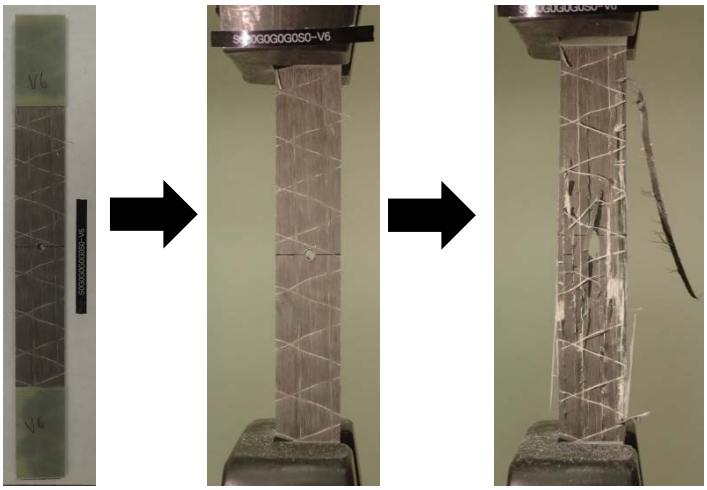

Figure 3-2 Pre- and post-failure tensile test specimens of fiber-reinforced hybrid composite

3.6 Results and Observations

Average results of non-hybrid monolithic and half-cyclic tensile tests are presented in Table 3-3. Figures 3-3, 3-4, 3-5, 3-6, and 3-7 present the stress-strain relationships of hybrid composites under monolithic tensile and open-hole tension (OHT) and half-cyclic (OHC) loading.

Table 3-3 Results of no-hole and open-hole monolithic and half-cyclic testing of hybrid composites

	No-Hole		Open-Hole Tension				Open-Hole Cyclic	
Composite	σ_{ult}, ksi (MPa)	ε_{ult}	σ_{ult}, ksi (MPa)	ε_{ult}	σ_{true}, ksi (MPa)	$\frac{\sigma_{true}}{\sigma_{ult,no\ hole}}$	σ_{ult}, ksi (MPa)	ε_{ult}
[SGGGGS]	93.1 (641.6)	2.90%	76.8 (529.5)	3.68%	86.8 (598.1)	0.932	75.5 (520.6)	2.68%
[SGSGSGS]	68.0 (468.9)	2.71%	48.3 (333.1)	2.26%	58.6 (422.01)	0.862	50.5 (348.1)	2.31%
[SSSGSSS]	40.1 (276.4)	2.71%	31.6 (218.1)	2.25%	37.7 (260.1)	0.940	32.6 (224.8)	2.34%
[MGGM]	41.7 (287.5)	2.24%	27.4 (188.9)	1.59%	36.1 (248.8)	0.866	27.2 (187.5)	1.43%
[GPG]	31.6 (217.9)	2.06%	27.6 (190.3)	1.75%	31.0 (213.9)	0.982	25.9 (178.6)	1.41%

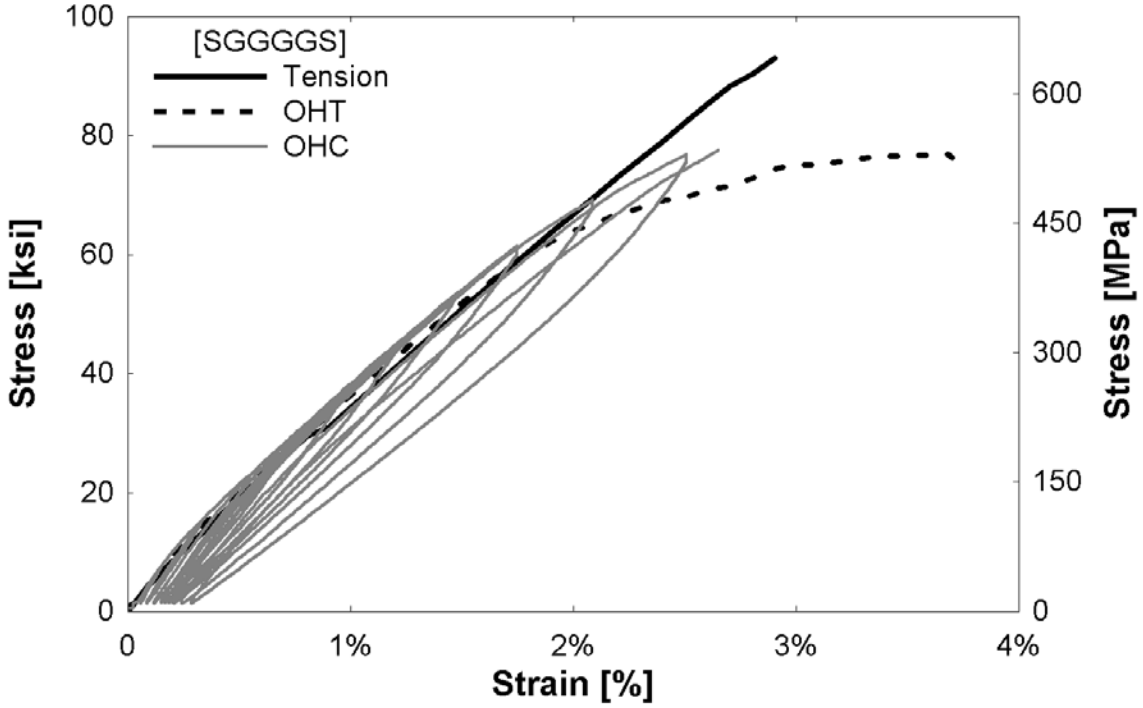

Figure 3-3 [SGGGGS] composite no-hole monolithic tensile, open-hole tensile (OHT), and open-hole half-cyclic (OHC) testing stress-strain relationships

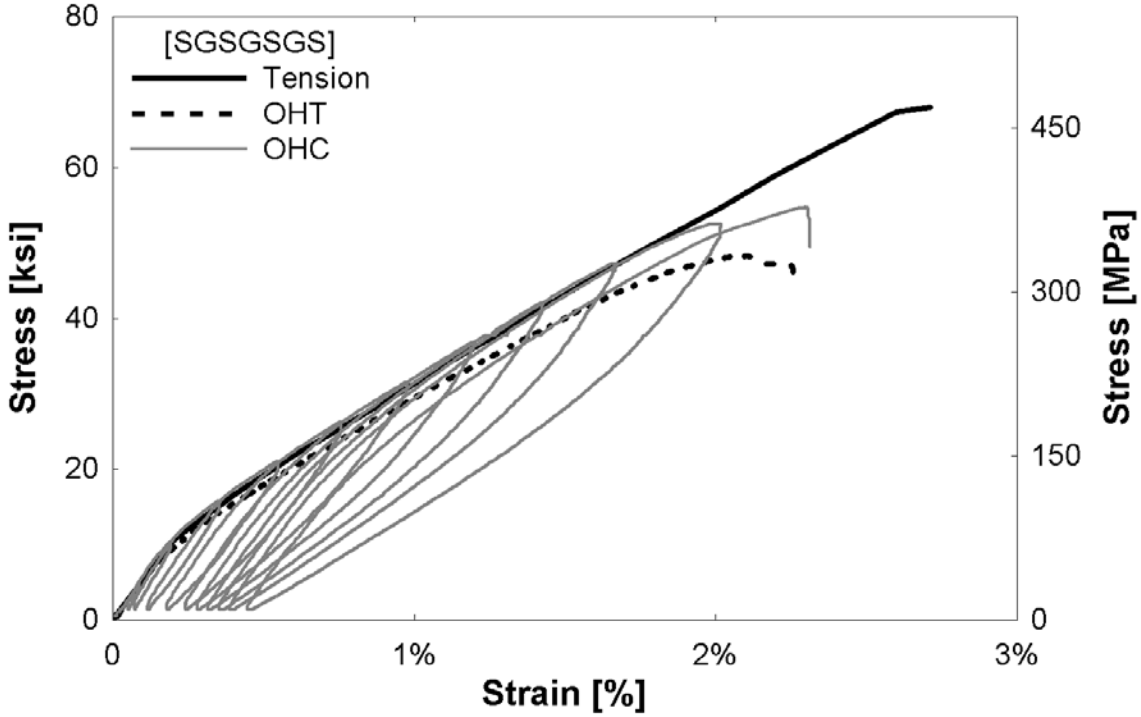

Figure 3-4 [SGSGSGS] composite no-hole monolithic tensile, open-hole tensile (OHT), and open-hole half-cyclic (OHC) testing stress-strain relationships

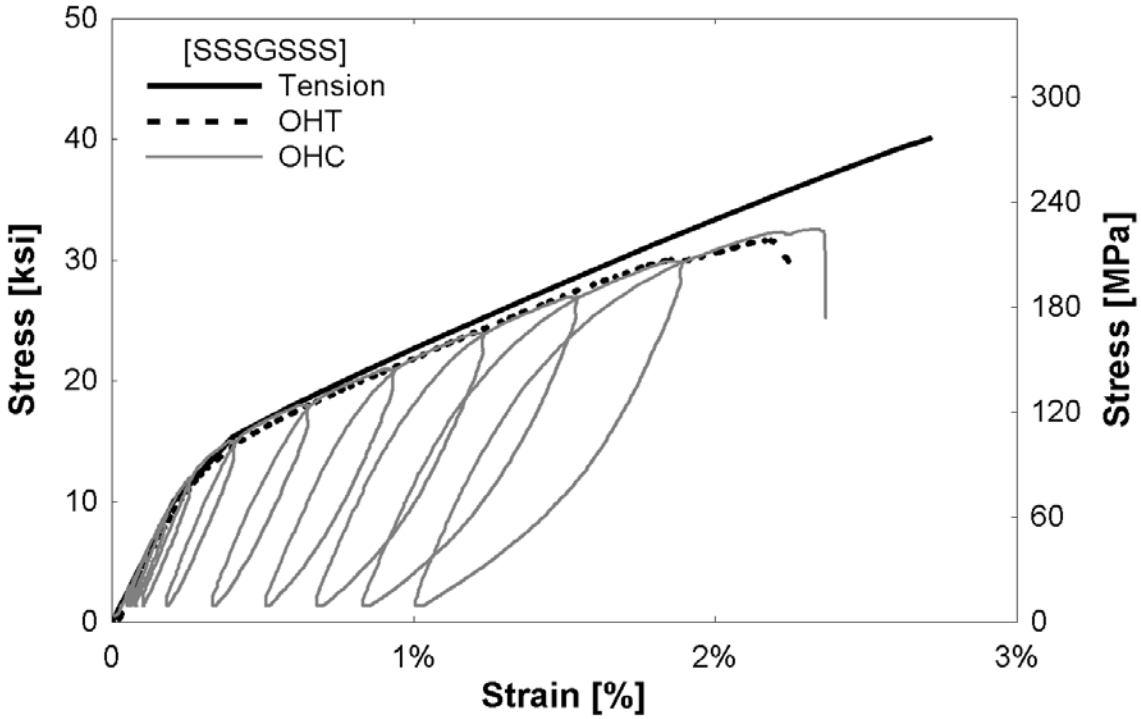

Figure 3-5 [SSSGSSS] composite no-hole monolithic tensile, open-hole tensile (OHT), and open-hole half-cyclic (OHC) testing stress-strain relationships

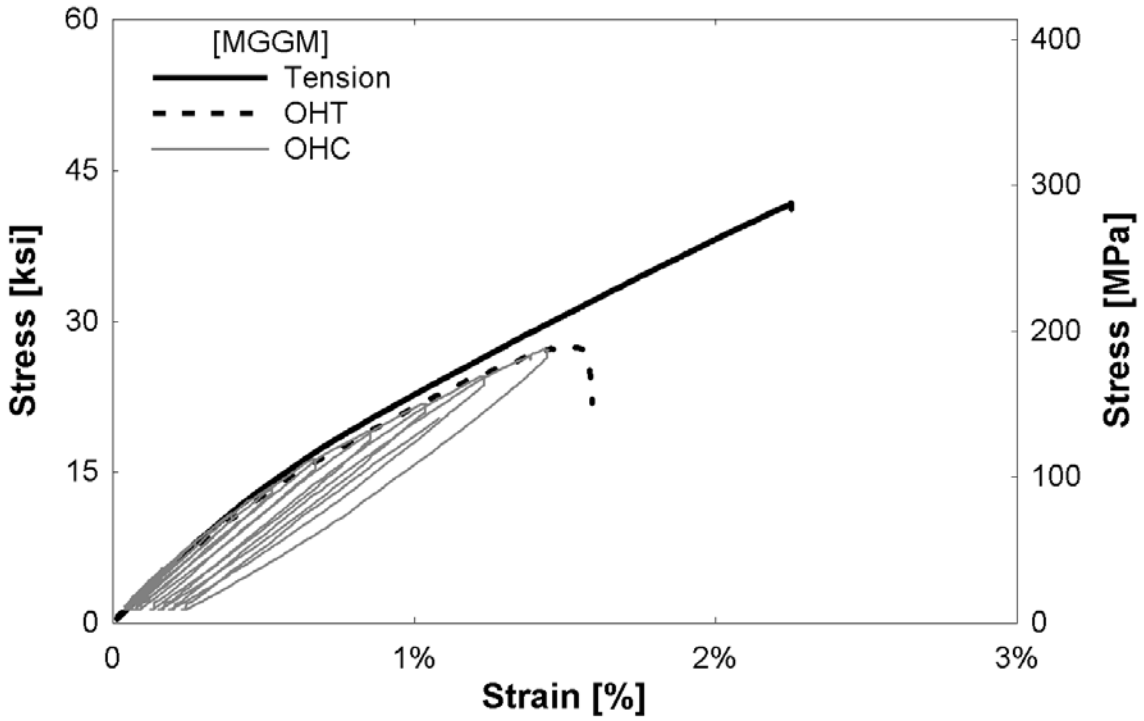

Figure 3-6 [MGGM] composite no-hole monolithic tensile, open-hole tensile (OHT), and open-hole half-cyclic (OHC) testing stress-strain relationships

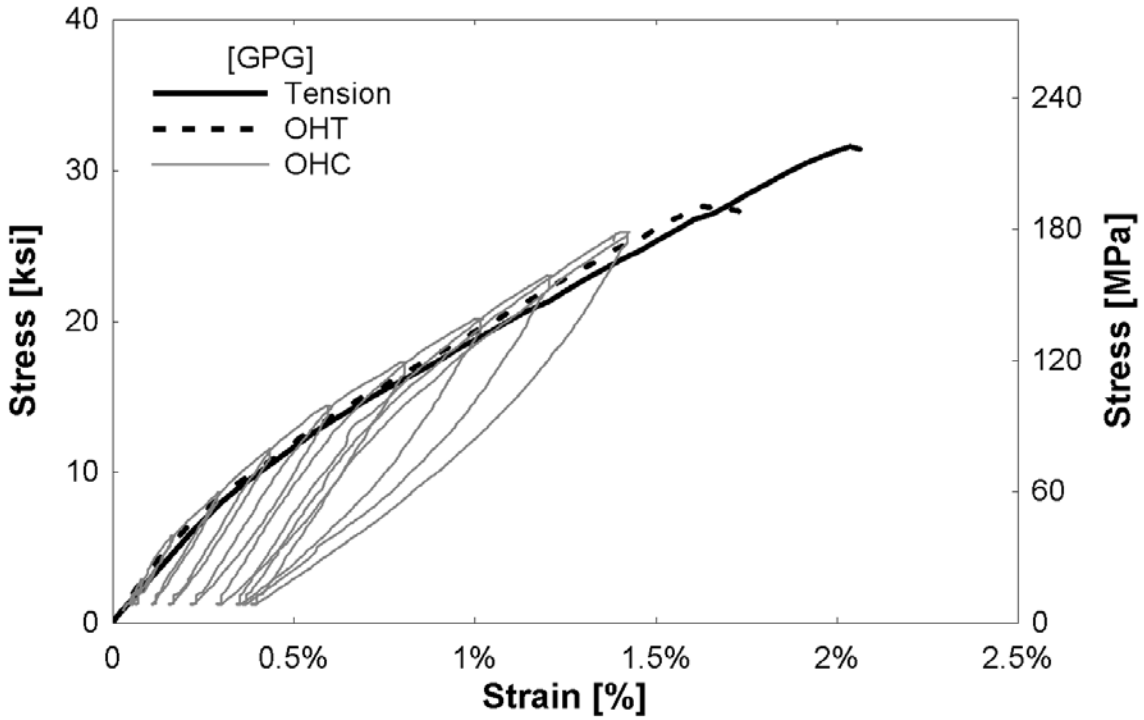

Figure 3-7 [GPG] composite no-hole monolithic tensile, open-hole tensile (OHT), and open-hole half-cyclic (OHC) testing stress-strain relationships

Similar to the non-hybrid specimens, the bonded and debonded specimens were averaged together to yield the final results. Overall, the hybrids comprised of steel fibers performed better than steel mesh and perforated steel. The [SGGGGS] composite (70G:30S) had the highest ultimate strength at 93.1 ksi (641.6 MPa) and a failure strain of 2.90%. The [SGSGSGS] composite (50G:50S) had strength of 68.0 ksi (468.9 MPa) and failure strain of 2.71%. The [SSSGSSS] composite (30G:70S) had an ultimate strength of 40.1 ksi (276.4 MPa). It was seen that the full strain capacity of the steel fibers was not fully utilized. However, yielding was present before failure, which presents a structural benefit. Future research may explore fiber layup to capitalize on increased steel ductility. The mesh hybrid composite, [MGGM] and the perforated steel hybrid composite, [GPG] had ultimate strengths of 41.7 ksi (287.5 MPa) and 31.6 ksi (217.9 MPa), respectively. For the two latter composites, it is realized that only half of the reinforcement is in the direction of loading, and thus contributing to the axial tensile performance. Figure 3-8 presents a comparison of all non-hybrid composites under monolithic tension (no-hole).

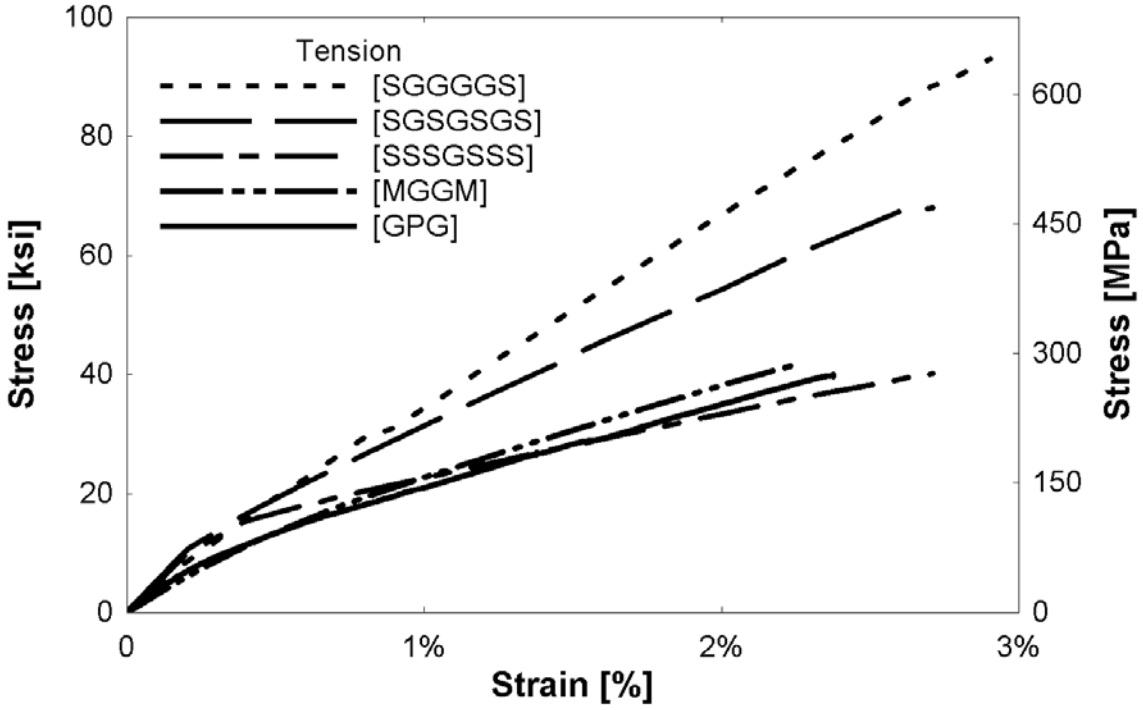

Figure 3-8 Hybrid no-hole composite monolithic tensile testing stress-strain relationships

Figure 3-9 presents a comparison of hybrid no-hole vs. open-hole monolithic tensile stress-strain relationships. It can be seen that the presence of a hole in the specimen lowered the ultimate strength. The fiber composite with the largest percentage of glass displayed the largest decrease, showing the largest vulnerability to a stress concentration; this pattern was seen in the non-hybrid composites as well. All forms of steel reinforcement helped retain more strength with a hole.

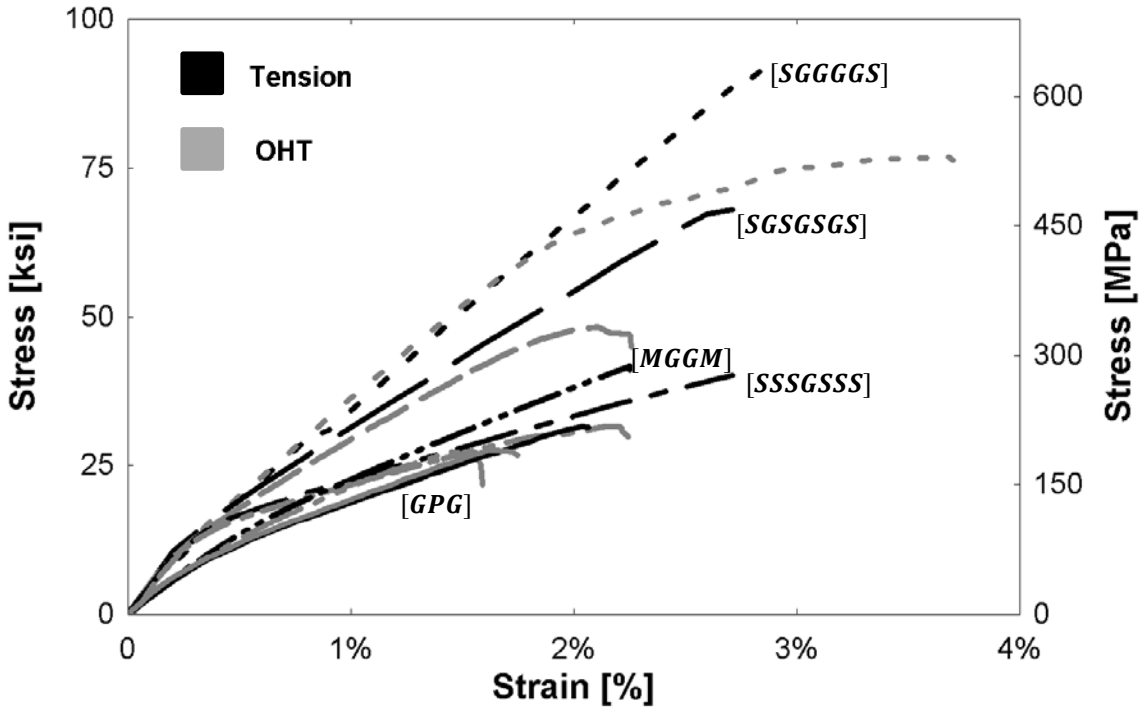

Figure 3-9 Hybrid no-hole vs. hole composite monolithic tensile testing stress-strain relationships

Figure 3-10 presents a comparison of open-hole monolithic vs. half-cyclic tensile hybrid stress-strain relationships. The backbones of the cyclic curves were presented. The OHT tests were displacement-controlled and the OHC tests were load-controlled. It can be seen that the presence of damage, or the prior cycles of loading and unloading, does not have a large effect on the composite behavior.

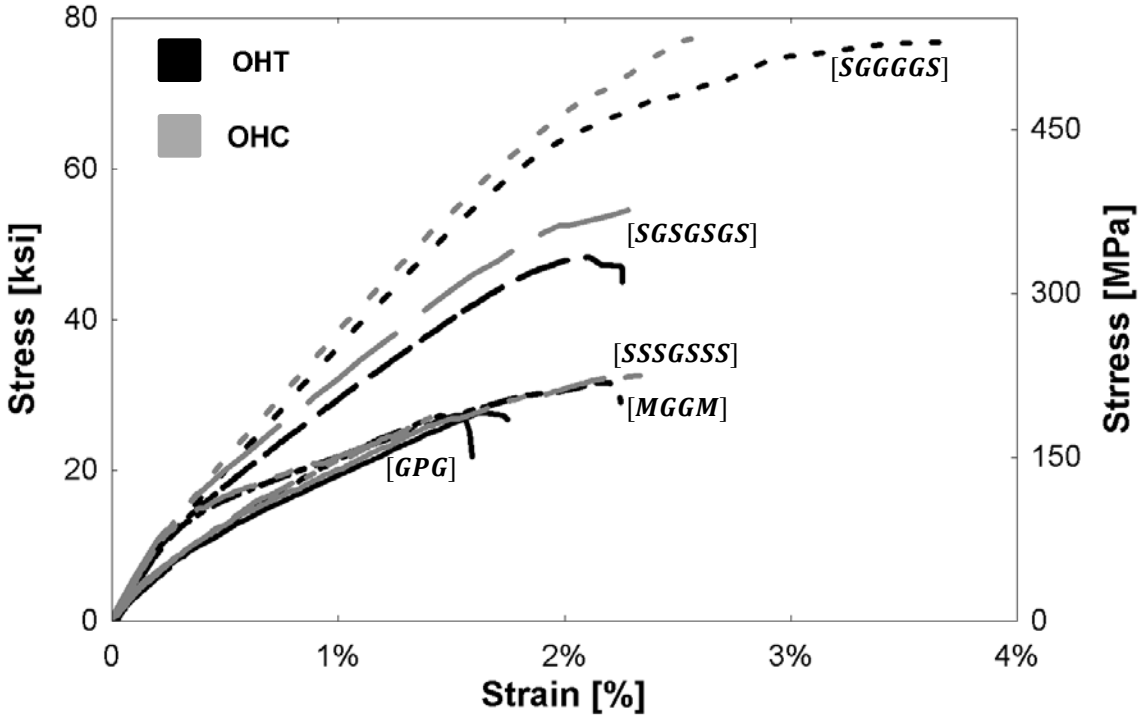

Figure 3-10 Hybrid composite open-hole monolithic vs. half-cyclic tensile testing stress-strain relationships

Overall, the mesh and perforated steel composites did not perform as well as fiber-reinforced composites. The thickness of these forms of reinforcement seemed to cause debonding of layers during loading. Therefore, only the comparison of non-hybrid and hybrid fiber-reinforced composites will be presented in Chapter Four.

4 CHAPTER FOUR –COMPARISONS OF PERFORMANCE OF NON-HYBRID AND HYBRID FIBER COMPOSITES

4.1 Introduction

This chapter will present the failure mechanisms of all tested composites. The remaining sections will be comparing the performance of only composites containing small-diameter glass and steel fibers. Based on previous data analysis, it was decided that the steel mesh and perforated steel sheets do not prove viable reinforcement for the desired hybrid properties. The tensile properties, cyclic properties, and a predictive hysteresis model will be presented. Steps taken to account for errors in data collection instruments were also discussed.

4.2 Failure Mechanisms

The failure mechanisms are investigated to further understand the mechanical behavior of the composite specimens. All samples tested of like composite types exhibited similar failure patterns. A complete set of failure specimens is presented in Appendix C. The general failure mechanism of the UD glass composites, $[G]_5$, can be described as a “brooming” effect as described by Harik et al. [33], and seen in Fig. 4-1. This is a result of scattered fiber breakage and debonding from the matrix. As observed from the stress-strain relationship, the failure was sudden and brittle. This random brooming effect confirms the stochastic failure and high energy release of the fibers at multiple locations.

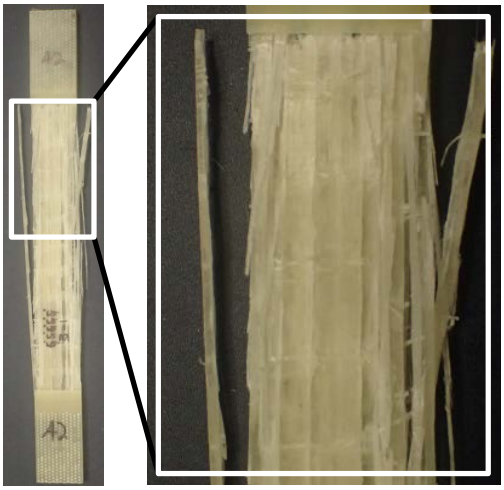

Figure 4-1 UD glass composite failure specimen

The UD steel fiber composites, $[S]_8$, exhibited failure nearly perpendicular to the direction of loading as shown in Fig. 4-2a. The fracture cross-section was not in-plane, indicating there was fiber pullout and necking. At the presence of a matrix crack, the fibers start to yield and therefore produce a more localized failure, visible in the microscope image in Fig. 4-2b. The steel fibers were able to maintain the integrity of the composite after the matrix cracks started forming. This is also evident as the composite continues to yield beyond the failure strain of the epoxy. This composite showed high ductility and the failure strain of 12.03% was more than 2 times that of the pure epoxy previously tested (5%).

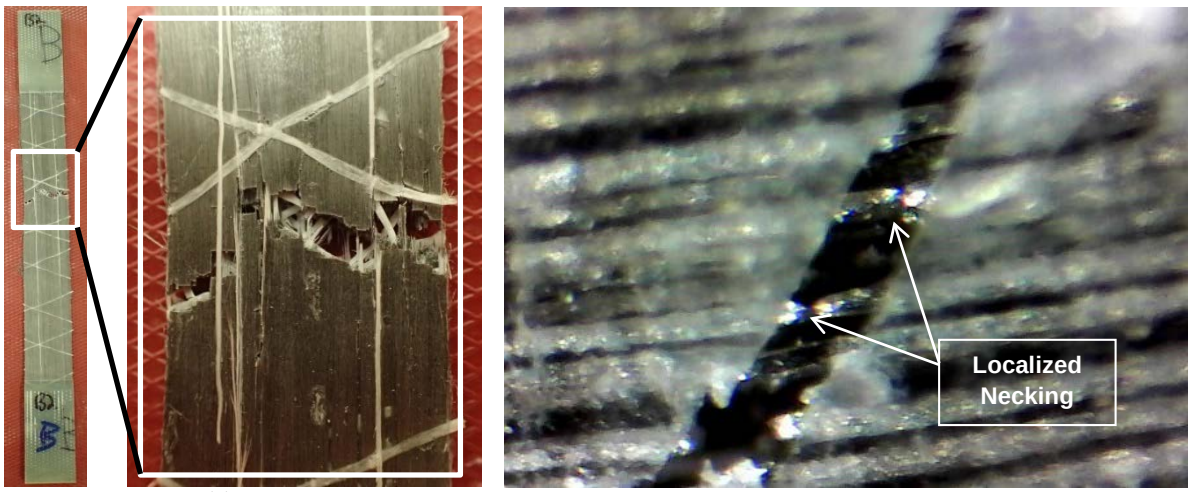

(a) (b)

Figure 4-2 UD steel composite failure specimen

The three different hybrid fiber-reinforced composite failure patterns can be seen in Fig. 4-3.

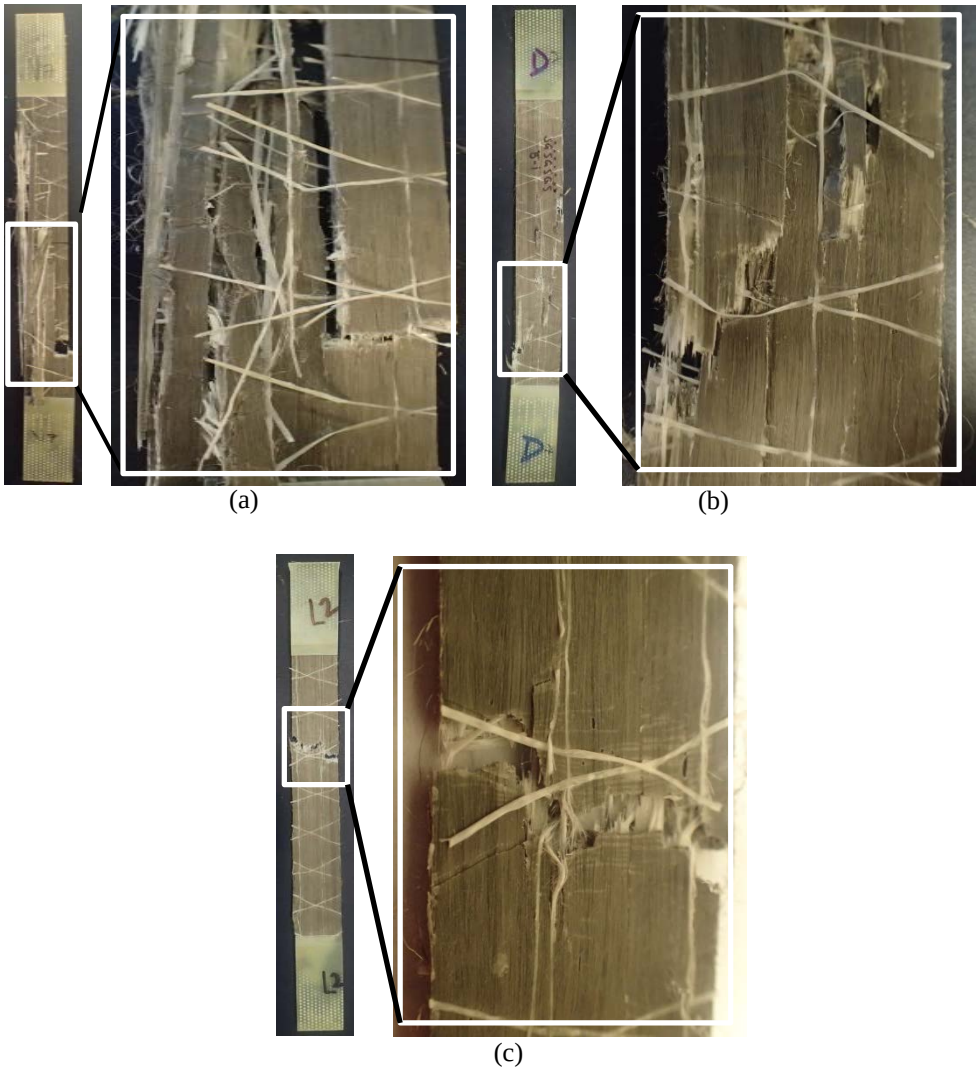

Figure 4-3 Hybrid fiber-reinforced composite failure specimens
(a) [SGGGGS]; (b) [SGSGSGS]; (c) [SSSGSSS]

It was observed that there was a failure type spectrum ranging from all glass to all steel (Fig. 4-4). The hybrid failure patterns lay within the spectrum depending on the respective fiber fractions. The hybrids with higher percentages of glass exhibited similar failures to $[G]_5$ where failure was distributed along the length. Assuming the glass fibers fail first in a random pattern, the stress must be transferred to the neighboring steel fibers at many different locations along the gauge length. It is clear that the failure is distributed more vertically; this resulted in

larger failure strains. This represents a spread of plasticity along the length of the specimen. In contrast, hybrids with higher percentages of steel resembled the localized $[S]_8$ failure more. Although the failure strain of the composites was not nearly as high as the $[S]_8$ composite, the presence of any yielding of the steel can offer warning to potential structural failure.

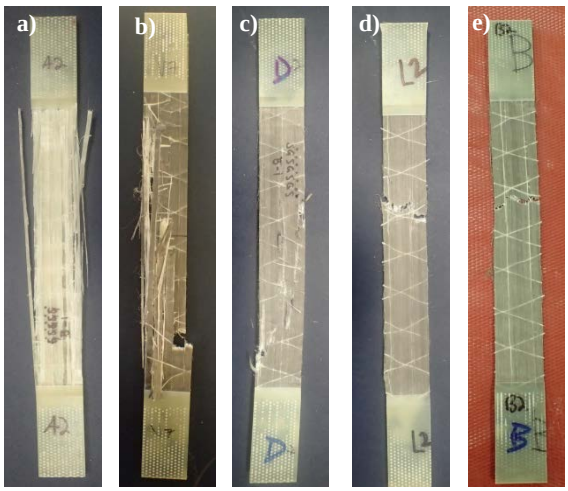

Figure 4-4 Failure spectrum in order of increasing steel percentage
(a) $[G]_5$, (b) [SGGGGS], (c) [SGSGSGS], (d) [SSSGSSS], (e) $[S]_8$

The steel mesh and perforated steel non-hybrid composites failed in a nearly identical fashion, perpendicular to the applied load as seen in Fig. 4-5. It was evident that when the epoxy filled in the openings of the reinforcement, it did not allow for global yielding throughout the length. Thus the failure was horizontal and localized at a matrix crack. Necking is evident at the fracture cross-sections. The low stiffness of the mesh hybrid can be attributed to the stress concentrations due to ondulations of the fine wires.

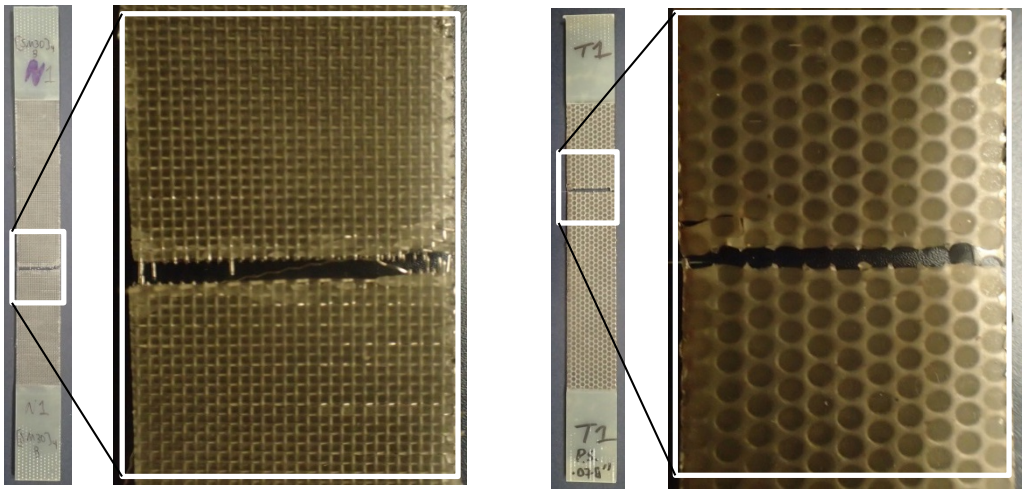

(a) (b)

Figure 4-5 Steel mesh and perforated steel non-hybrid composite failure specimens
(a) $[M]_4$; (b) $[P]_1$

In [MGGM], the steel was on the outside, thus containing the brooming effect of the broken glass fibers on the inside (Fig. 4-6a). This brooming effect is more evident on the [GPG] as the glass was on the outside. Another failure mechanism that was not seen in the other composites is partial and complete delamination of the layers around the failure surface. One explanation for this would be that these two forms of reinforcement allowed the composite to act more like FMLs made of different layers adhered together, thus being less homogenous than fibers. The thickness of the metal may have played a role in the poor adhesion of the fiber to the matrix and had a negative effect on the overall composite mechanical properties. After the glass fibers failed, complete delamination occurred and the composite was no longer intact. This failure mechanism confirms that these two forms of metal reinforcement are not viable choices for the desired hybrid composite applications.

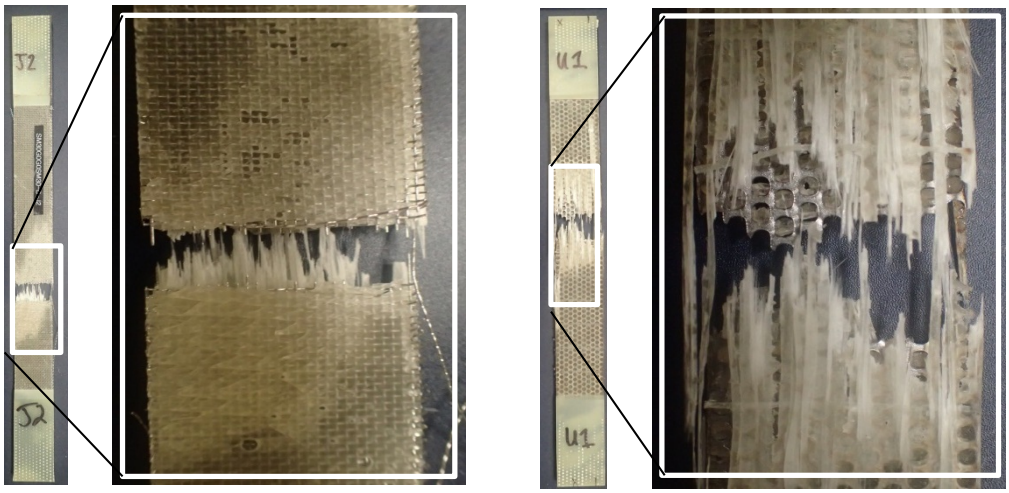

(a) (b)

Figure 4-6 Steel mesh hybrid and perforated steel hybrid composite failure specimens
(a) [MGGM]; (b) [GPG]

4.3 Tensile Properties

The ultimate nominal tensile strength (σ_{ult}), failure strain (ε_{ult}), and true tensile strength (σ_{true}) are reported for each specimen in Table 4-1. Figure 4-7 shows the no-hole monolithic tensile stress-strain relationships of the fiber-reinforced composites.

Table 4-1 Results of no-hole and open-hole specimen tensile tests

	No-Hole		Open-Hole Tension				Open-Hole Cyclic	
Composite	σ_{ult}, ksi (MPa)	ε_{ult}	σ_{ult}, ksi (MPa)	ε_{ult}	σ_{true}, ksi (MPa)	$\frac{\sigma_{true}}{\sigma_{ult,no\ hole}}$	σ_{ult}, ksi (MPa)	ε_{ult}
$[G]_5$	96.8 (667.4)	2.50%	68.7 (473.8)	2.46%	82.5 (568.6)	0.852	65.9 (454.7)	2.55%
[SGGGGS]	(93.1) 641.6	2.90%	76.8 (529.5)	3.68%	86.8 (598.1)	0.932	75.5 (520.6)	3.41%
[SGSGSGS]	68.0 (468.9)	2.71%	48.3 (333.1)	2.25%	58.6 (422.01)	0.900	50.5 (348.1)	2.83%
[SSSGSSS]	40.1 (276.4)	2.71%	31.6 (218.1)	2.25%	37.7 (260.1)	0.941	32.6 (224.8)	2.34%
$[S]_8$	30.1 (207.7)	12.03%	23.4 (161.1)	4.50%	28.1 (193.6)	0.932	24.5 (168.9)	3.32%

The fiber composites ultimate strengths are listed in decreasing order: $[G]_5$, [SGGGGS], [SGSGSGS], [SSSGSSS], and $[S]_8$. It can be seen that the composite tensile strengths decrease as more steel is added. However, the addition of steel added slightly more ductility to the hybrids.

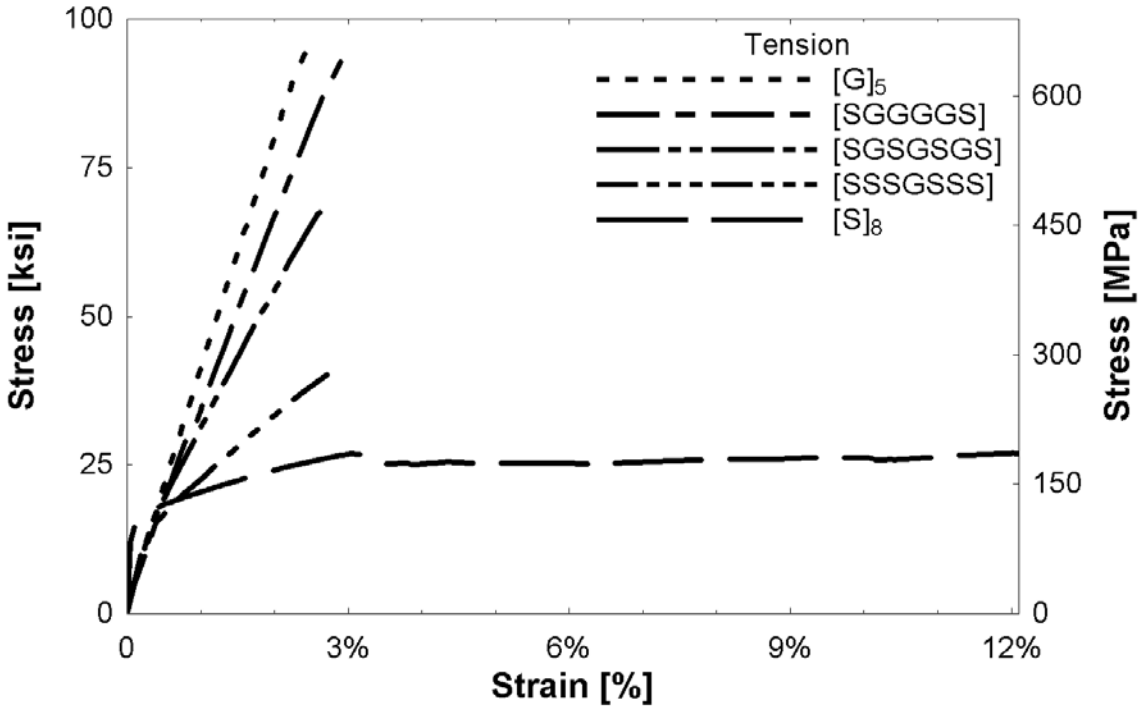

Figure 4-7 Hybrid no-hole composite monolithic tensile testing stress-strain relationships

Figure 4-8 presents a comparison of the monolithic tensile stress-strain relationships of composites with and without a hole. The stiffness of the open-hole (OHT) specimens remains unaffected while there is a decrease in the ultimate tensile strength caused by the reduction in cross-sectional area. The true stress using the reduced area and a ratio of the true stress to the ultimate no-hole nominal tensile stress, $\frac{\sigma_{true}}{\sigma_{ult,no\ hole}}$, is presented in Table 4-1. The presence of steel decreased the vulnerability of the composites to stress concentrations, as indicated by higher ratios. This highlights another shortcoming of conventional FRPs comprised of brittle fibers. The addition of steel fibers into the glass/epoxy composite was successful in retaining the ultimate strength even with a stress concentration present.

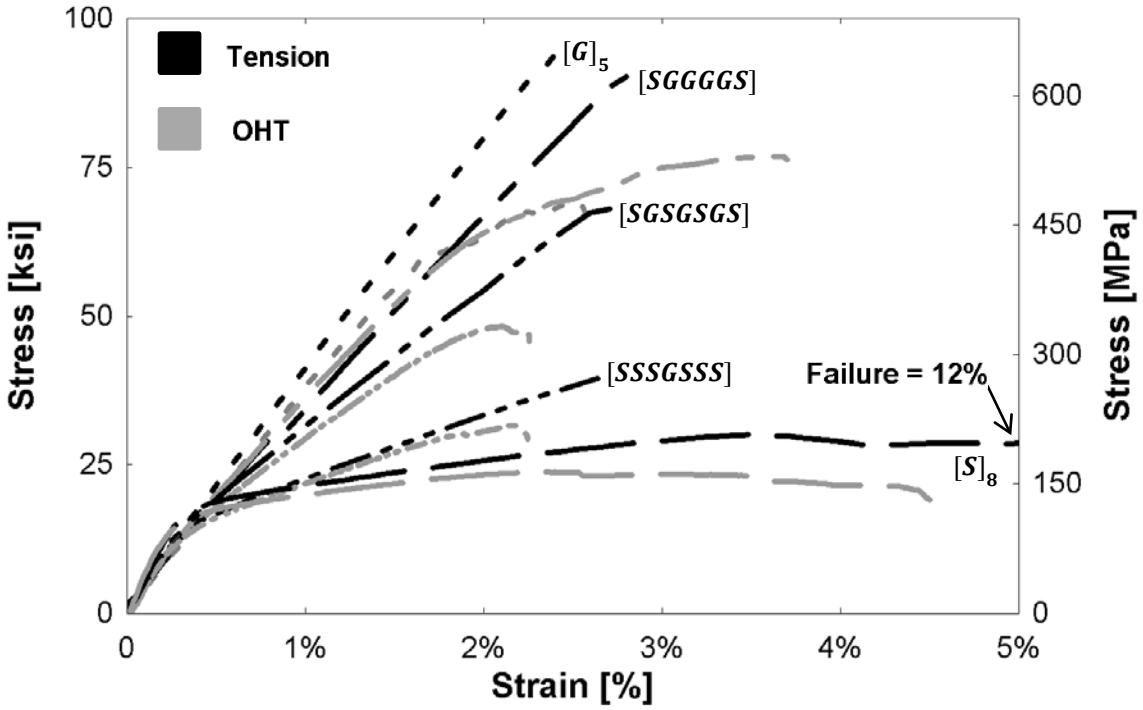

Figure 4-8 Tensile stress-strain relationships of specimens with and without holes

Figure 4-9 presents open-hole specimen stress-strain relationships. The tensile curves (OHT) and the backbone of the half-cyclic curves (OHC) are shown for all composites. The ultimate strength and failure strains are presented in Table 4-1. The OHT tests were displacement-controlled and the OHC tests were load-controlled. The stress-strain behavior during tensile and half-cyclic loading remained fairly consistent. This may signify that the accumulated damage from loading/unloading below the ultimate stress does not have a significant effect on the composite mechanical properties.

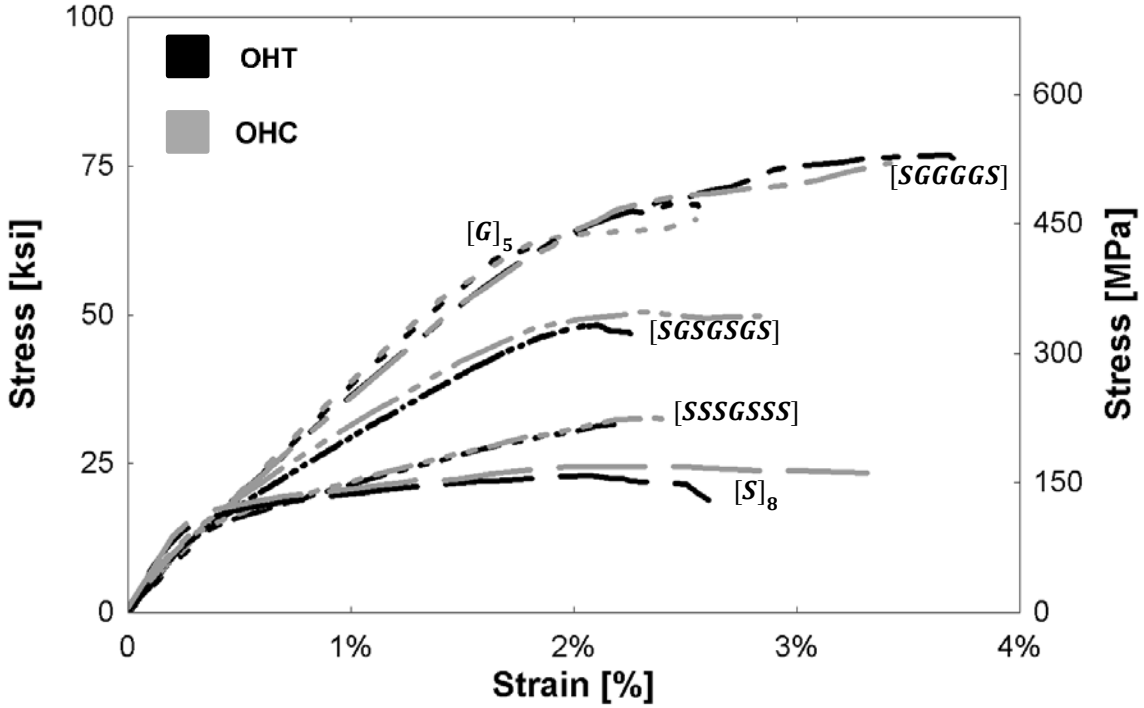

Figure 4-9 Stress-strain relationships of specimens with holes during monolithic tensile and half-cyclic loading

4.3.1 Rule of Mixtures Curve Synthesis

Figures 4-10, 4-11, and 4-12 depict tensile stress-strain relationships of curves synthesized using the rule of mixtures (ROM); this sums the stresses of individual constituents based on volume fraction of the hybrid composites. The figure also presents the actual experimental curve. The glass and steel curves were obtained by subtracting the contribution of epoxy. Epoxy is shown as its own entity. The close-up of the linear region of the curves confirms that the ROM was valid in the elastic region, as seen by the prediction of the stiffness. Slight differences between curves can be attributed to fiber misorientation or volume fraction measurement inaccuracies. After the steel begins to yield at approximately 0.2%, the rule of mixtures slightly over predicts the stress-strain relationship. The experimental curve is consistently 92-95% of the theoretical synthesized curve in the plastic region. The failure strain

of the experimental hybrid is consistently greater than the synthesized value for all hybrids. This confirmed that there was a positive effect on failure strain due to hybridization.

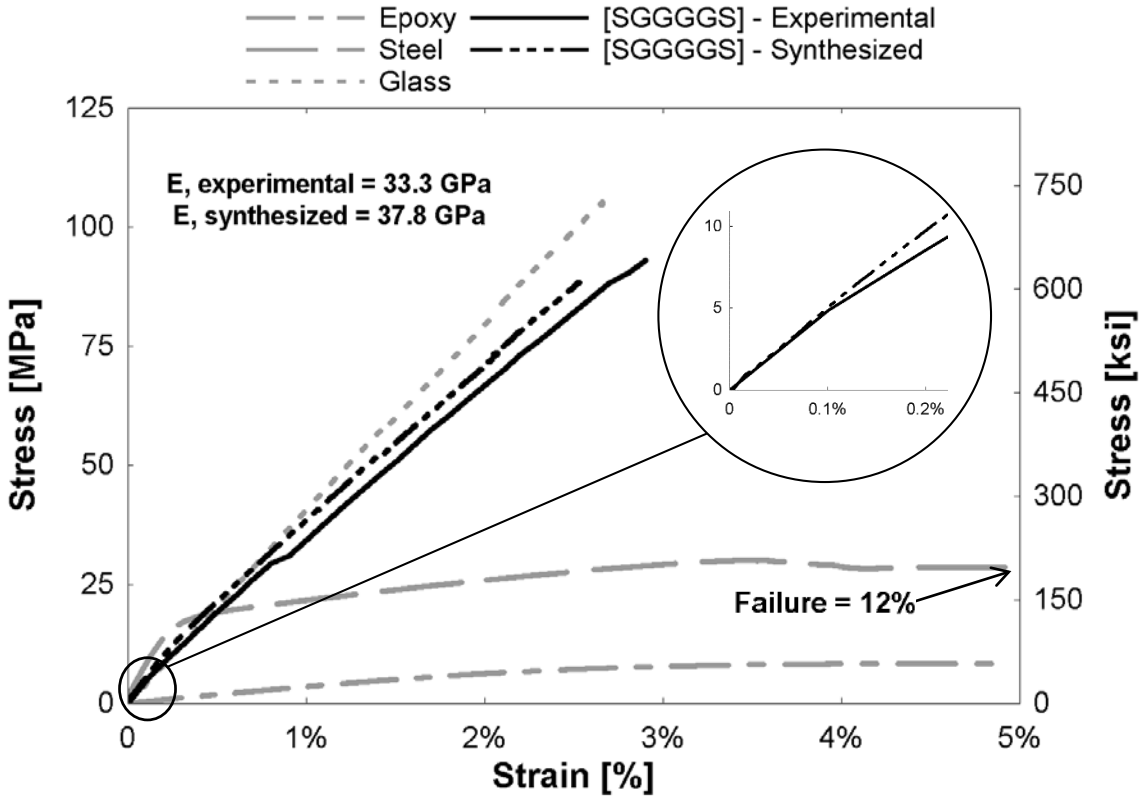

Figure 4-10 [SGGGGS] hybrid composite curve synthesis

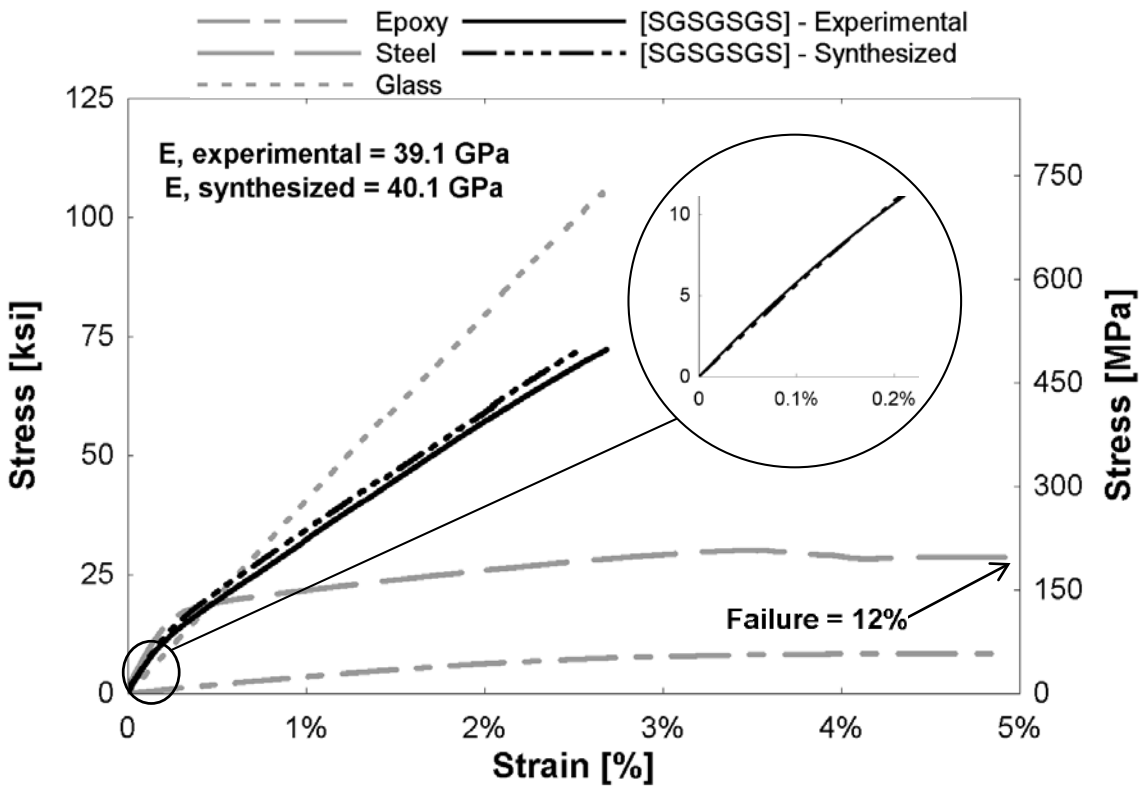

Figure 4-11 [SGSGSGS] hybrid composite curve synthesis

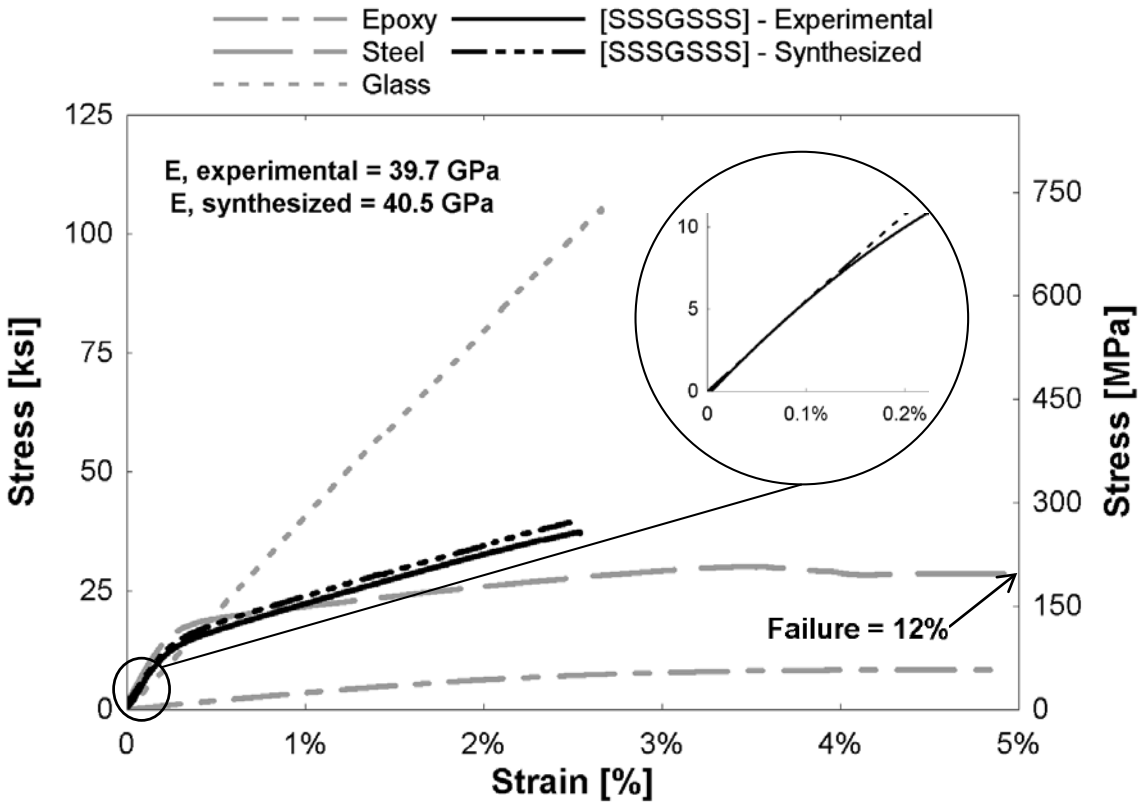

Figure 4-12 [SSSGSSS] hybrid composite curve synthesis

4.4 Cyclic Properties

Figure 4-13 shows a sample of stress-strain behavior after half-cyclic tensile loading of an open-hole specimen, [SSSGSSS]. The maximum stress and strain at the 7th cycle, $0.7\sigma_{ult}$, is indicated on the figure to show how energy dissipation was found at the end of each loading cycle. The area under the curve is hatched to signify the amount of energy absorbed up to this loading cycle. Residual strain caused from plastic deformation was assumed to be the strain at the end of each unloading cycle.

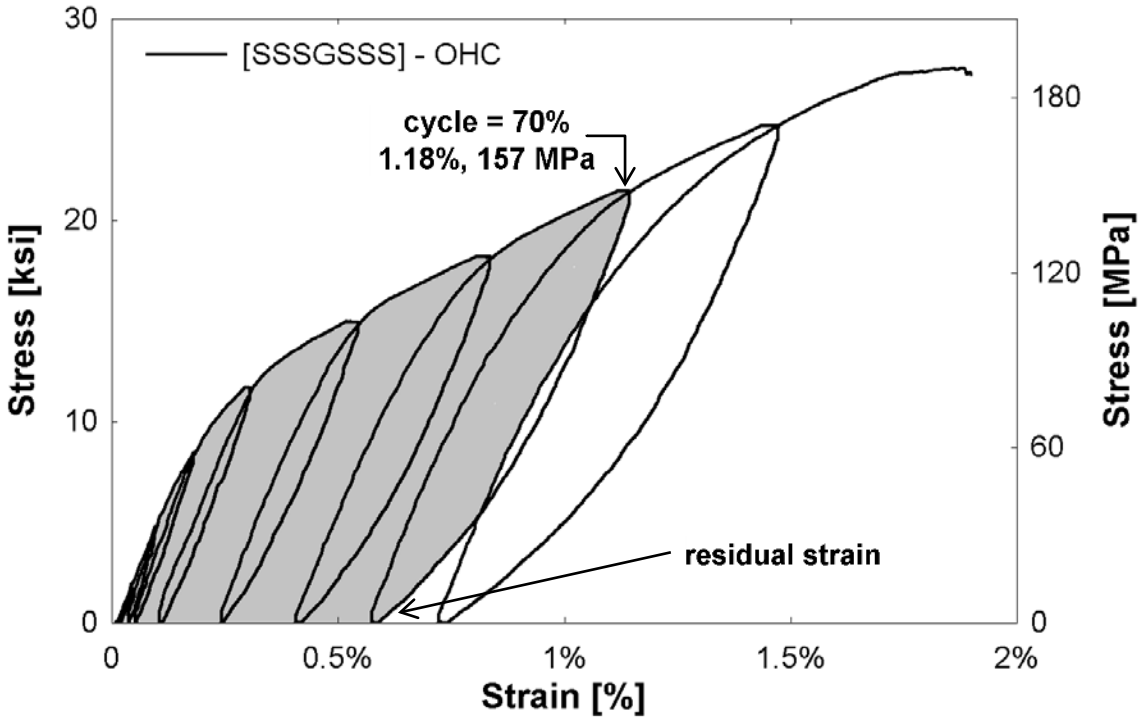

Figure 4-13 Area under the curve of half-cyclic loading for [SSSGSSS]

Figure 4-14a shows the amount of energy dissipated during open-hole half-cyclic loading of the composites. The percentage adjacent to each curve represents the total volume fraction of steel within the composite. The x-axis represents the maximum strain reached at each cycle prior to unloading. The y-axis represents the energy dissipated during each loading cycle found by integrating the stress-strain curve. For a perfectly elastic material with no permanent

deformation, the energy dissipated will be near zero prior to failure as the material unloads along the same linear path. This was evidenced by specimen $[G]_5$. Plastic materials will dissipate energy due to yielding during loading. This leads to warning before failure, which is ideal in structural design. A composite comprised of high strength elastic glass fibers and ductile steel fibers will have a large area under the stress-strain curve, indicating a high amount of energy dissipated. The [SGGGGS] hybrid dissipated the most energy, consisting of only 8.2% steel. Since the strength of the glass is significantly higher than the steel fibers, this hybrid does not need a large amount of steel to achieve high energy dissipation. Figure 4-14b displays a normalized energy value per 1% of steel present in the composite. It remained consistent that the less steel present in the hybrids, the more energy that was dissipated. This may sound counter-intuitive. However, the random failure of glass spread the plasticity throughout the specimen and allowed more steel to be engaged.

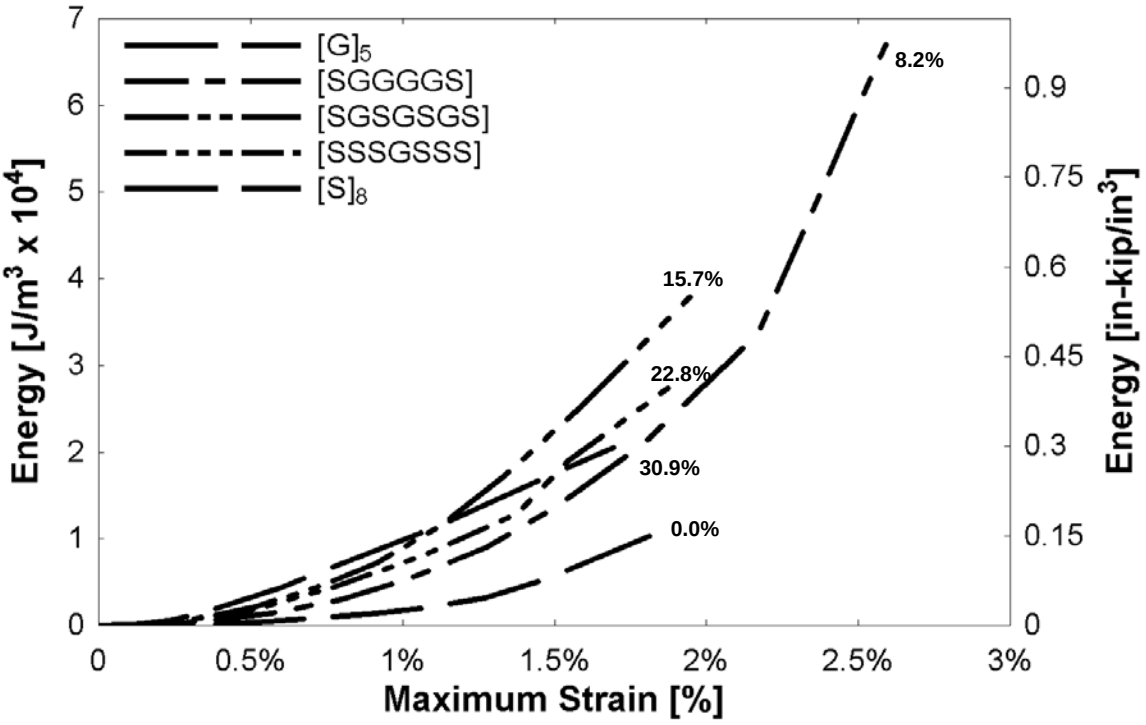

(a)

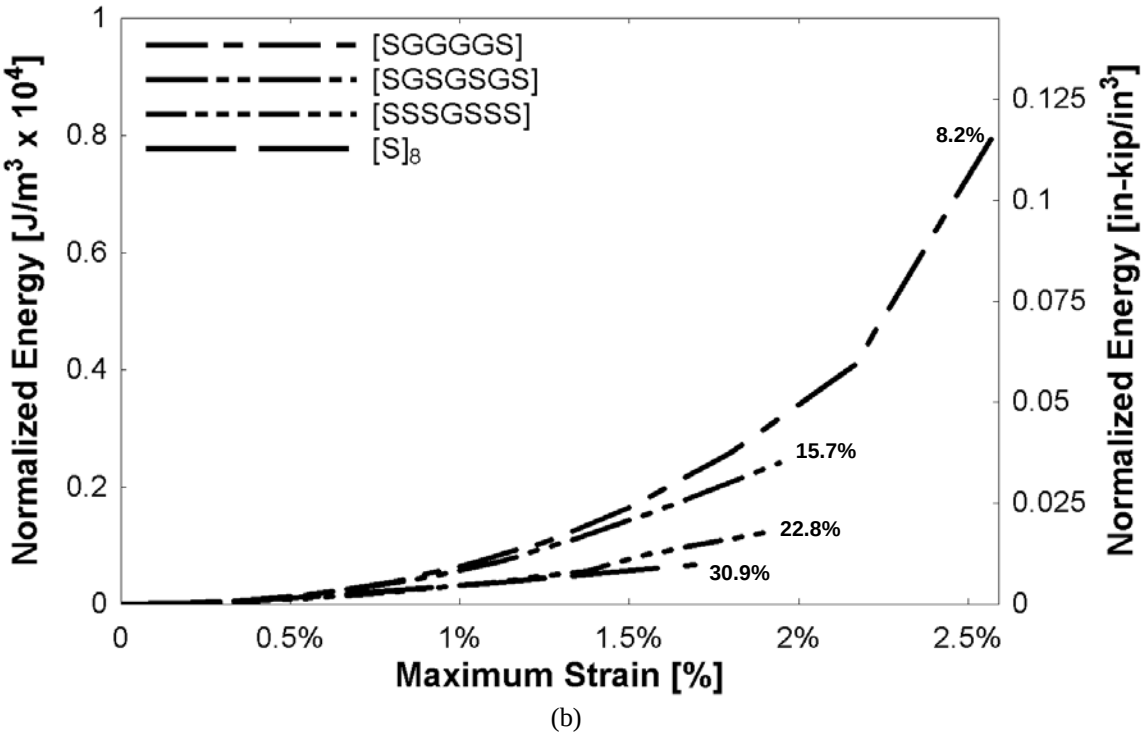

(b)

Figure 4-14 Energy dissipation of composites during open-hole half-cyclic loading
(a) Calculated Energy Values; (b) Normalized energy values per 1% of steel

The main goal of this nonmetal-metal hybrid composite is to improve ductility and energy absorption prior to failure. However, ductility causes permanent deformation and residual strain over the material lifecycle. A material that has re-centering capabilities after loading and unloading is appealing for both strength and serviceability limit states. Figure 4-15 shows the residual strain behavior after open-hole half-cyclic loading. The x-axis represents the maximum strain reached at each cycle prior to unloading. The y-axis represents the residual strain ratio, which is calculated as the residual strain at the end of a loading cycle over the cycle's maximum strain. The closer the ratio is to zero, the better re-centering capabilities the material has. For a perfectly elastic material with no plastic deformation, the residual strain ratio will be near zero. This behavior was seen in the $[G]_5$ specimen. In contrast, an inelastic material has a ratio closer to one, as seen in the $[S]_8$ specimen. Of the three hybrid composites, the one with the lowest percentage of steel, [SGGGGS], had the lowest residual strain ratio, plateauing around 0.12. This signifies very good re-centering capabilities. The other hybrids also had more favorable re-centering capabilities with relatively low ratios that plateaued as well. A material that has a low and consistent residual strain ratio along loading cycles represents stability.

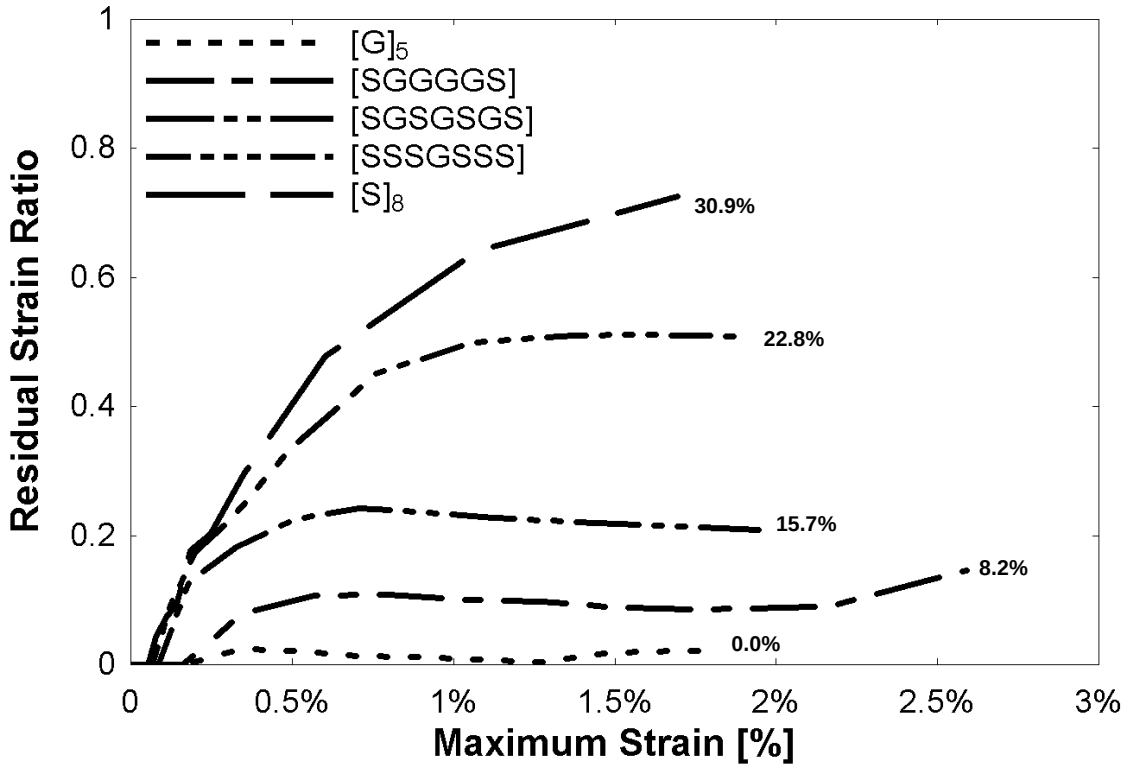

Figure 4-15 Residual strain ratio of composites during open-hole half-cyclic loading

4.5 Predictive Hysteresis Model

To validate the experimental data, a theoretical model was used to further analyze the hybrid composite cyclic behavior. The combination of an elastic and plastic material presents a unique hysteresis behavior. Under half-cyclic testing, it was observed that the hybrid composites resemble the behavior of lead-rubber bearings (LRBs), commonly used as base isolators in structural seismic applications [34]. The LRB is another elastic-inelastic system and the novelty in this system lies in the re-centering force. This hybrid composite behavior may be predicted using the bilinear hysteresis model seen in Fig. 4-16. Point 1 begins at (0, 0) and the x-value of Point 2 is located at the yield strain of the steel fibers, ε_Y. The slope of line 1-2, or the elastic slope, represents young's modulus of the hybrid composite in the elastic region. The slope of line 2-3, or the hardening slope, is equivalent to the modulus of the glass and epoxy constituents, as

well as the post-yielding slope of the steel. The post-yielding slope was determined by bilinearization of the $[S]_8$ stress-strain relationship using equal areas (Fig. 4-17). This hardening slope is what dictates the return path at the unloading of each cycle. The x-value of point 3 represents the maximum strain attained at that respective cycle. The slopes of line 3-4 and line 5-6 are equal to that of line 1-2 and the vertical distance is equivalent to $2\sigma_Y$. Point 7 represents a targeted design strain. The 7-8-9-10 parallelogram signifies the outermost boundary of the ideal bilinear hysteresis behavior.

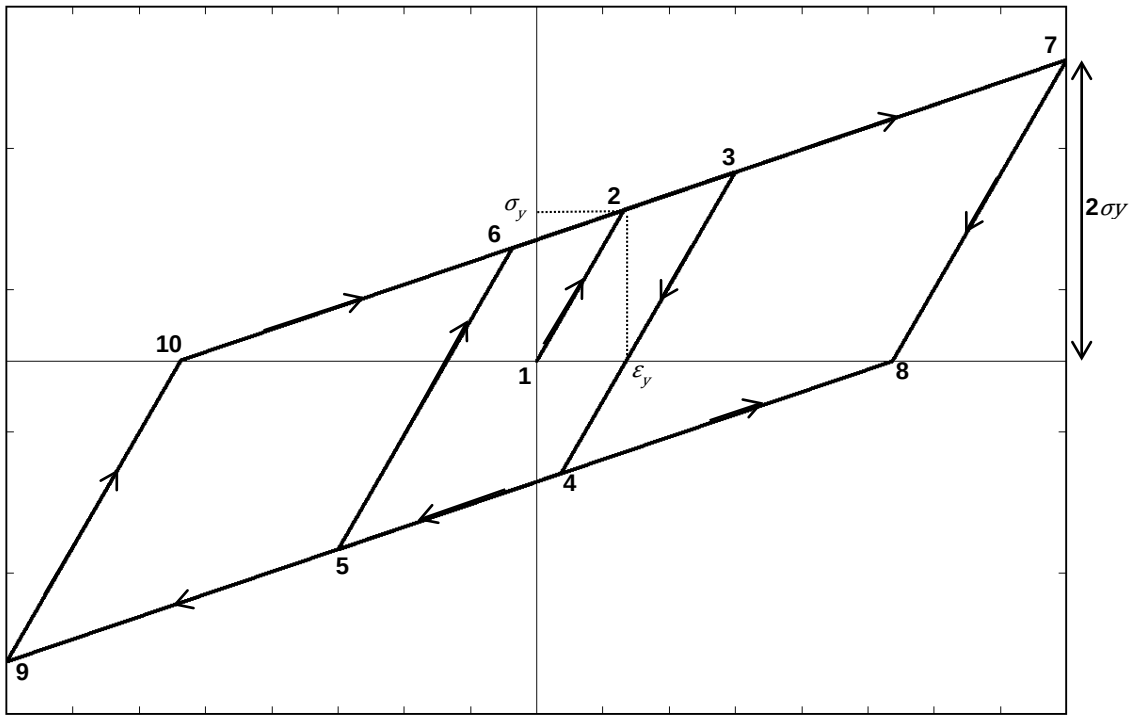

Figure 4-16 Lead-rubber bearing (LRB) ideal bilinear hysteresis behavior

This ideal hysteresis model was applied to the hybrid composites, [SGGGGS], [SGSGSGS] and [SSSGSSS], along with the steel composite, $[S]_8$ (Fig. 4-18). Although only half-cyclic testing was performed, the complete hysteresis behavior may be predicted because the stress-strain curve follows a kinematic hardening behavior. The dashed portion of the bilinear

model followed each tensile loading and unloading cycle. The black solid portion of the curve serves as an extension for full-cycle behavior by extending into the compression region. This bilinear model predicted the hysteresis behavior of all hybrid composites within a reasonable amount of accuracy; composites with a higher fraction of steel were predicted more closely. The calculated elastic and hardening slopes align with the paths of the experimental hysteresis behavior. If the hybrid composite cycles lay within the ideal parallelogram, it signifies material stability. Once the stress reaches greater than $2\sigma_Y$, the steel fibers will yield in compression. This leads to later loading cycles yielding and becoming more unstable over time. The area under each idealized loading cycle was found and the energy dissipation followed the same trend as the experimental values. As this model is an idealized shape, it can be seen how it can under- or over-predict the actual energy dissipation of the composite depending on the curve fit.

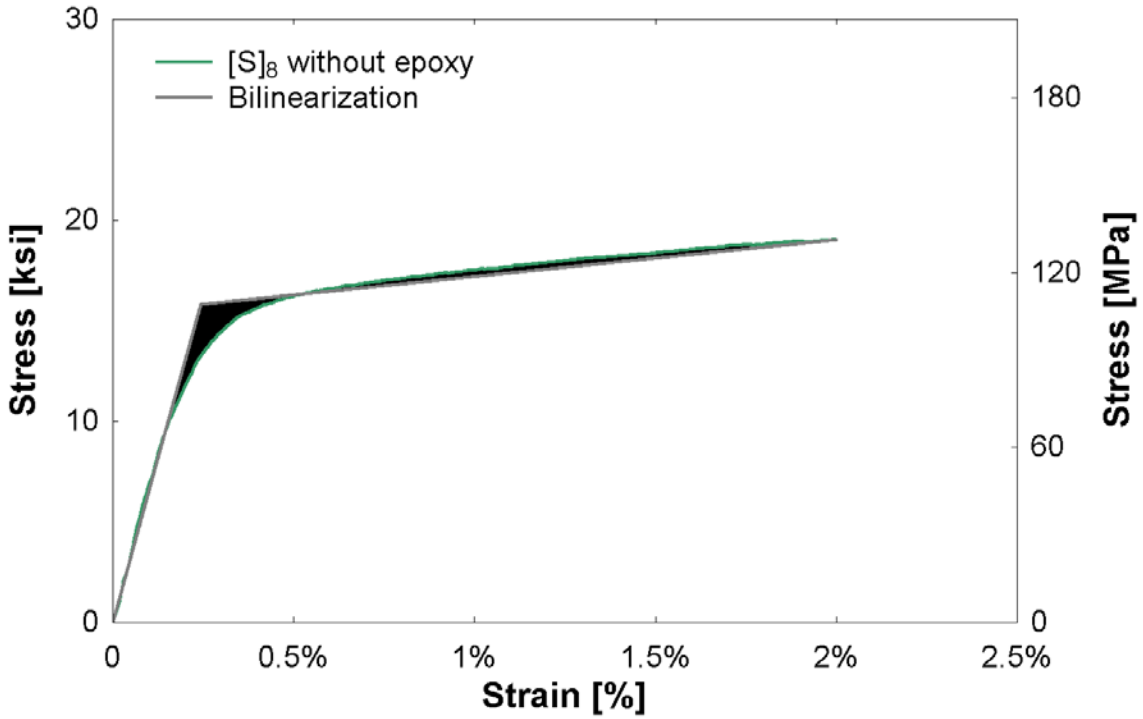

Figure 4-17 Bilinearization of $[S]_8$ using equal areas in order to obtain the post-yielding slope and yield strain

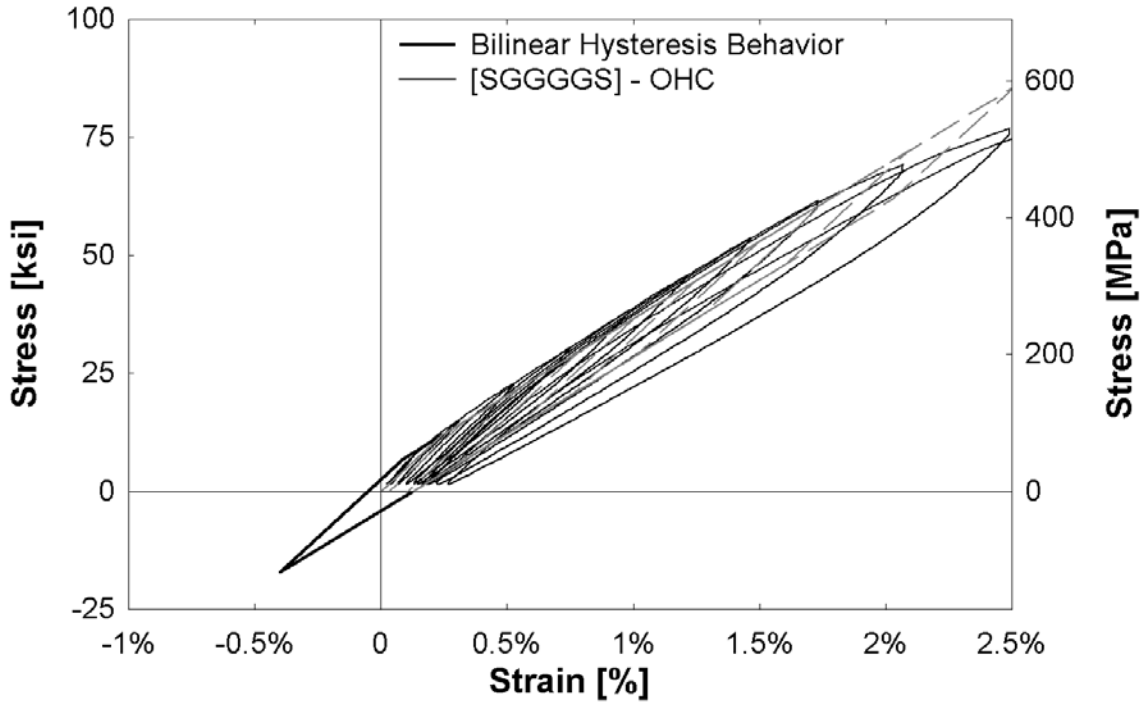
Bilinear Hysteresis Behavior
[SGGGGS] - OHC
Stress [ksi]
Stress [MPa]
Strain [%]
100
75
50
25
0
-25
600
400
200
0
-1%
-0.5%
0
0.5%
1%
1.5%
2%
2.5%

(a)

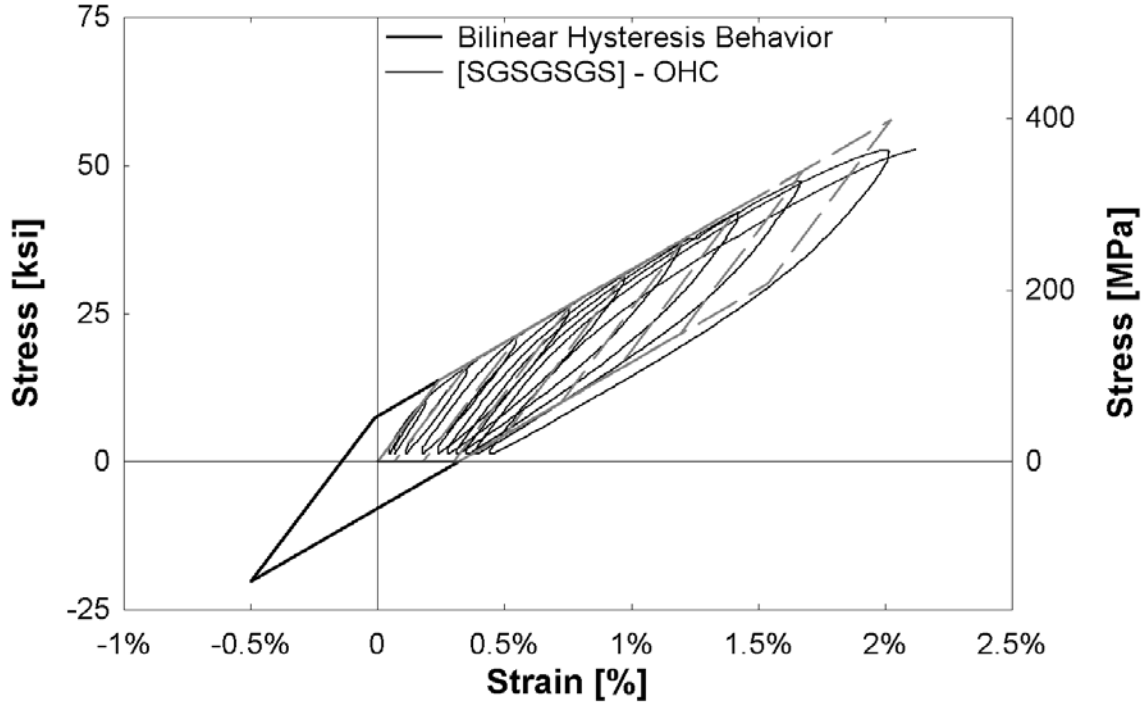
Bilinear Hysteresis Behavior
[SGSGSGS] - OHC
Stress [ksi]
Stress [MPa]
Strain [%]
75
50
25
0
-25
400
200
0
-1%
-0.5%
0
0.5%
1%
1.5%
2%
2.5%

(b)

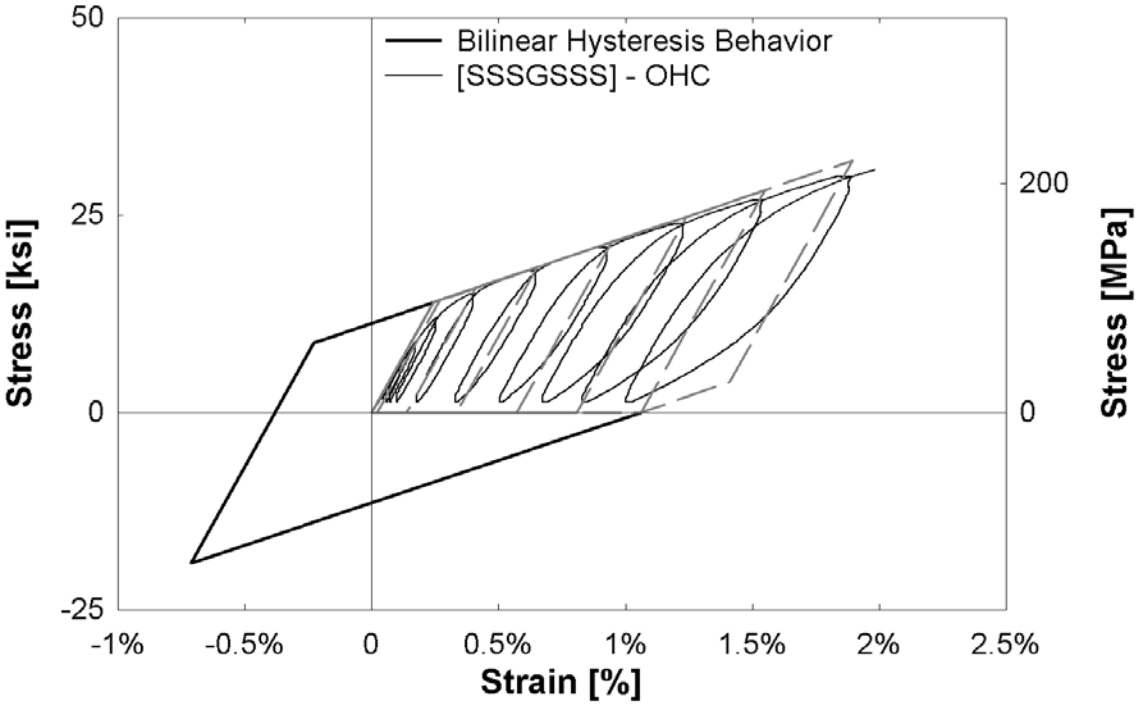

(c)

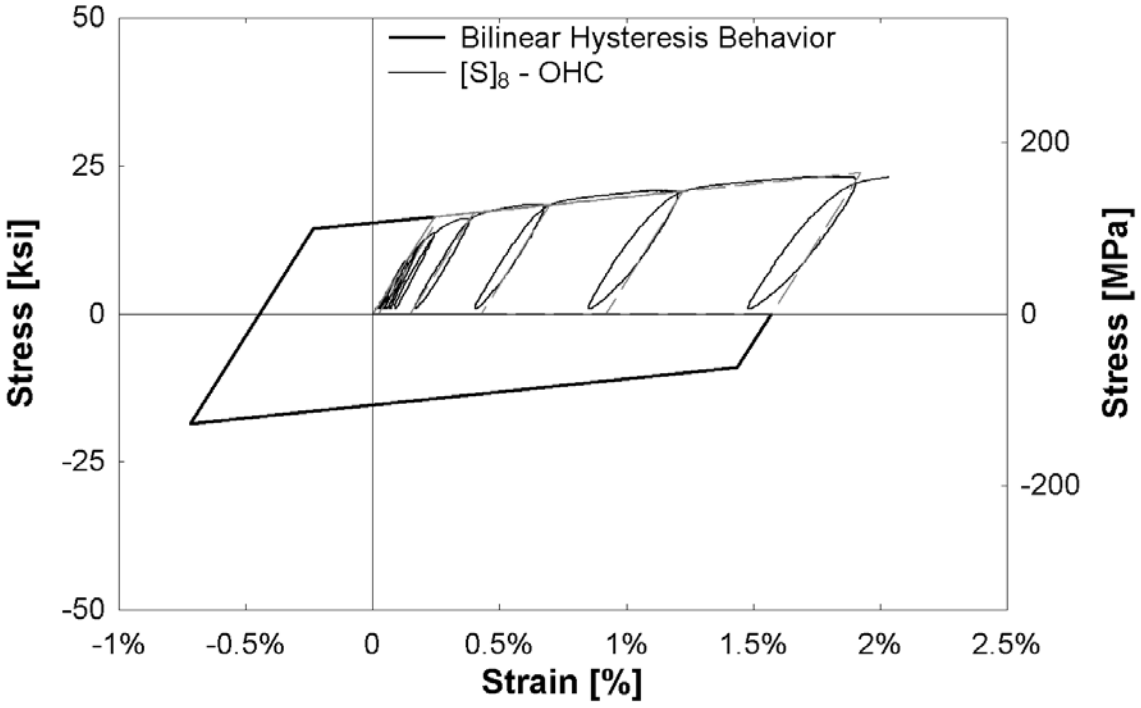

(d)

Figure 4-18 Ideal Hysteresis Behavior
(a) [SGGGGS]; (b) [SGSGSGS]; (c) [SSSGSSS]; (d) $[S]_8$

4.6 Data Collection Instrument Error Adjustments

Aside from expected noise in the extensometer collecting the strain data, there was an error during cyclic behavior. The extensometer used during testing was not originally intended for cyclic use. As the loading reached the top of each cycle and began unloading, there was a jump in the extension data being collected (Fig. 4-19). It was causing the top of each cycle to jump horizontally backwards before beginning its return path. This jump also occurred as the machine switched from unloading to loading as well. This became evident upon looking at the graph of extension vs. time (Fig. 4-20).

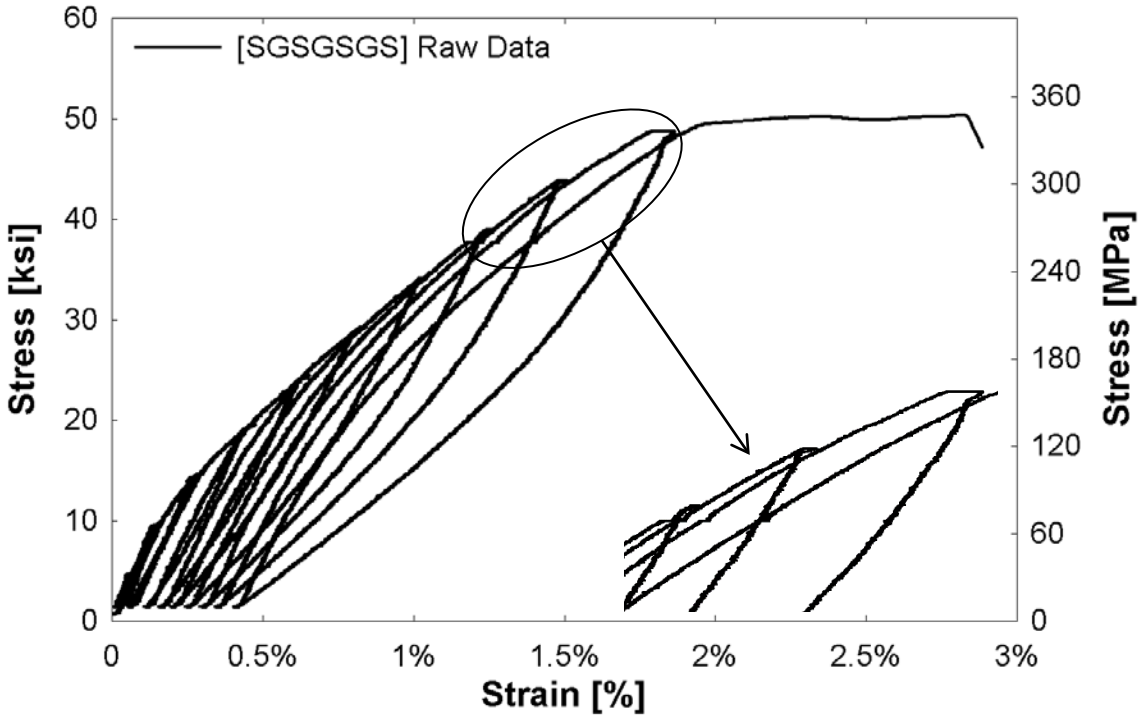

Figure 4-19 Stress-strain relationship displaying error in extensometer

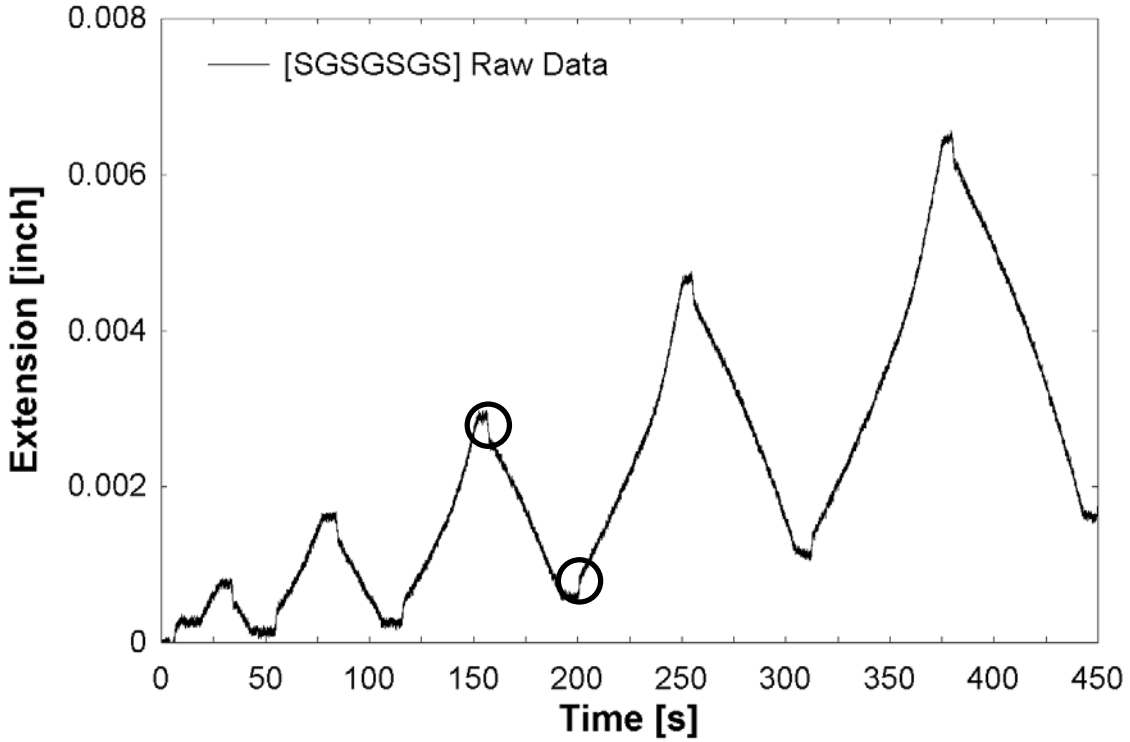

Figure 4-20 Strain vs. Time displaying jump in extensometer

In order to remedy this error, a prior and after moving average was taken of the strain vs. time curve (Fig. 4-21a). The frequency of the data acquired was 100Hz; therefore each moving average included 100 points before and after. These two curves were then subtracted from each other. Wherever there was a jump in the extensometer, there was a peak in the subtraction curve. This gave the exact location along the curve in which the jump occurred. One half of the 'jump window' was deleted from the position of each peak. The adjusted data was plotted as loading and unloading segments (Fig. 4-21b). Each unloading segment was then moved up in order to correct the jump. The final corrected stress-strain relationship is presented in Fig. 4-21c. This was necessary in order to correctly calculate energy dissipation values.

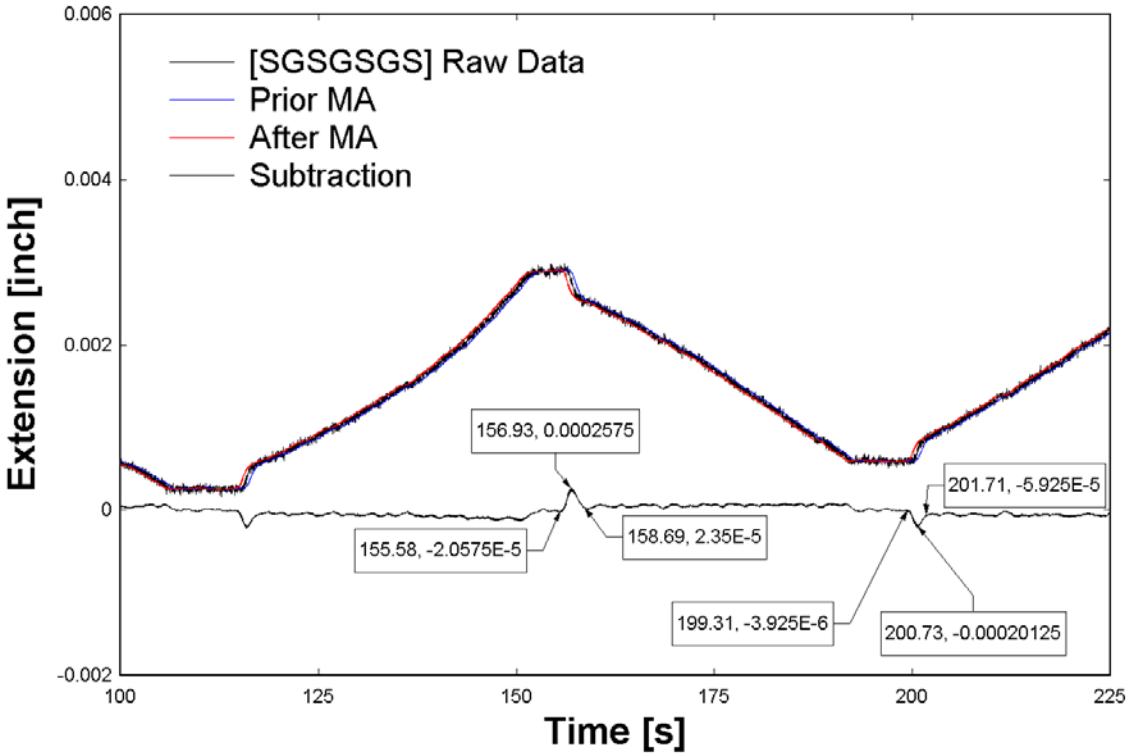
[SGSGSGS] Raw Data
Prior MA
After MA
Subtraction
Extension [inch]
Time [s]
0.006
0.004
0.002
0
-0.002
100
125
150
175
200
225
156.93, 0.0002575
158.69, 2.35E-5
155.58, -2.0575E-5
201.71, -5.925E-5
199.31, -3.925E-6
200.73, -0.00020125

(a)

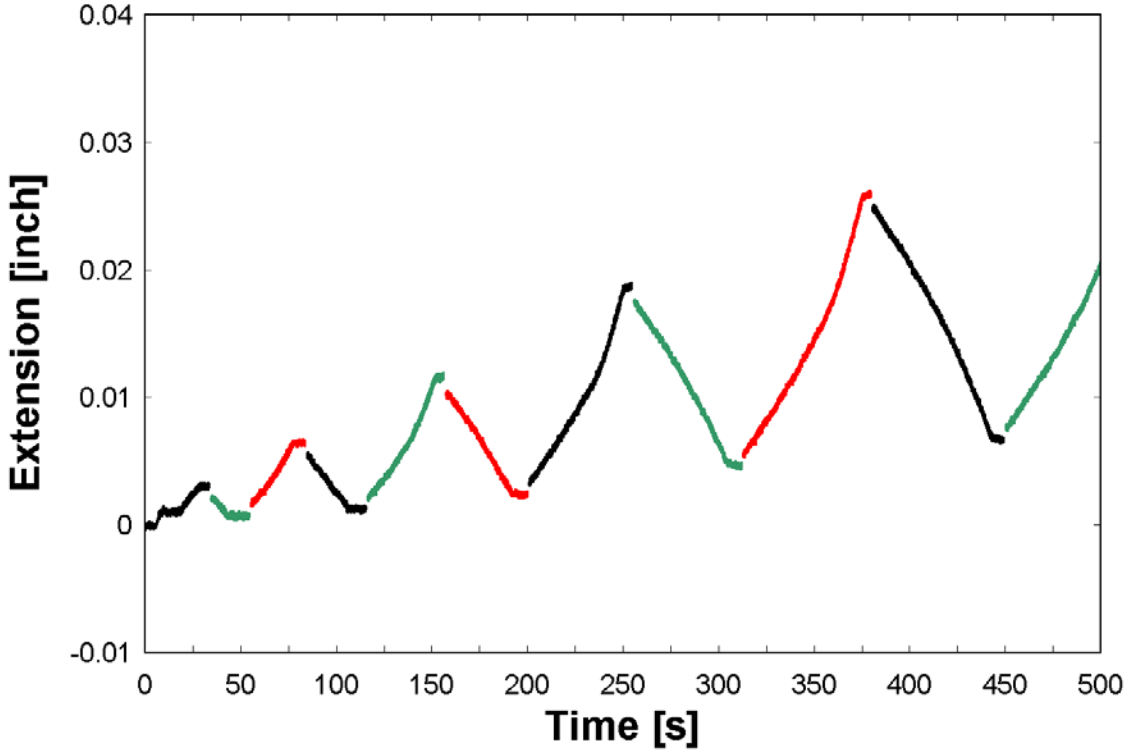
Extension [inch]
Time [s]
0.04
0.03
0.02
0.01
0
-0.01
0
50
100
150
200
250
300
350
400
450
500

(b)

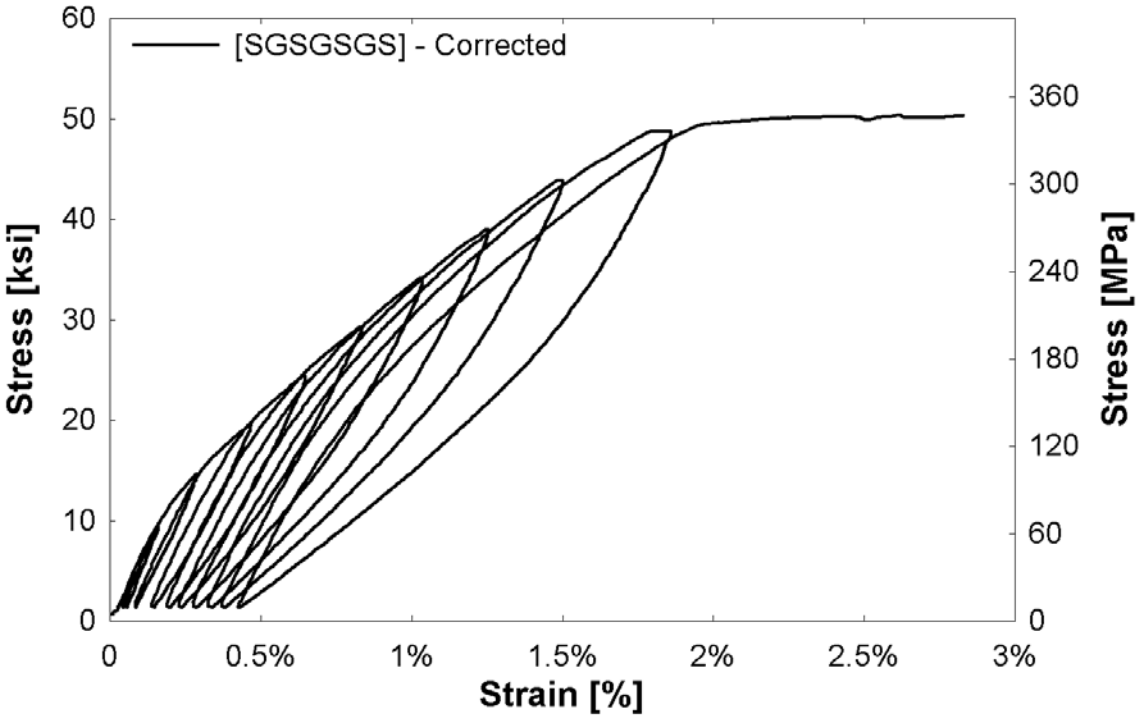

(c)

Figure 4-21 Curve adjustment procedure
(a) Moving averages and subtraction curve performed on stain vs. time graph; (b) Plotted loading and unloading segments; (c) Corrected stress-strain cyclic curve

5 CHAPTER FIVE – SUMMARY AND CONCLUSIONS

5.1 Summary

In an effort to offer a superior alternative construction material, a non-metal/metal hybrid composite was investigated. Ductility, energy dissipation, and re-centering were the properties of interest. Three different steel reinforcement types were incorporated into conventional glass fiber reinforced epoxy including: 1) small-diameter steel fibers, 2) fine wire steel mesh, and 3) thin perforated steel sheets. Among the fiber hybrids, three different fiber ratios of steel reinforcement were studied. Monolithic and open-hole tensile and half-cyclic tensile testing were conducted in order to characterize the material. The tensile properties, failure mechanisms, and cyclic behavior were investigated.

5.2 Conclusions

The conclusions presented herein are based on the results of the experimental investigation of glass/steel reinforced epoxy composite coupons. The mechanical properties of these composites were characterized and give rise to the following findings:

- Composites with thin steel fibers performed better than mesh and perforated steel in terms of strength, stiffness, and energy absorption. The failure mechanisms of the latter two indicate that the reinforcement was too thick and thus the composite did not act homogenously. The integrity of the composite was compromised after the failure of the glass fibers. It was concluded these two forms of reinforcement did not prove a viable option for the hybrid composite.

- The tensile strength of the hybrid composites was directly proportional to the respective glass and steel fiber percentages. The strengths from highest to lowest were as follows:

$[G]_5$, [SGGGGS], [SGSGSGS], {SSSGSSS], $[S]_8$. This order held true for tensile, open-hole tensile, and open-hole half-cyclic loading.

- The rule of mixtures (ROM) proved valid in the elastic region and predicted the stiffness values accurately. However, in the post-yield region, the ROM consistently over-predicted the stress. More research is needed on theoretical models of nonmetal-metal hybrid composites in the inelastic region.

- Composites with a higher percentage of steel had localized failure. In contrast, composites with higher percentages of glass had a more distributed failure pattern, making it difficult to predict failure location. The addition of steel helped maintain the integrity of the composite after the failure of the glass fibers. The hybrid composites experienced a ductile failure, which may provide warning to structural failure. This was due to the spread of plasticity over a larger area due to kinematic hardening.

- The addition of steel fibers to glass/epoxy composites decreased the vulnerability to stress concentrations. Accumulated damage from cyclic loading does not have a significant effect on the composite stress-strain relationship. This can be beneficial in structural elements subjected to repeat dynamic loading.

- [SGGGGS] outperformed [SGSGSGS] and [SSSGSSS] and offers a balanced compromise of constituent properties. This composite had the highest strength, dissipated the most energy during loading, and showed the most consistent re-centering capabilities. It was found that a lower percentage of steel fibers (8.2%) in the hybrid composite outperformed those with higher percentages (15.7%, 22.8%). This may signify

that there is an optimal amount of steel to be added to hybrid glass/steel fiber reinforced epoxy composites.

- The hybrid composite full-cyclic behavior may successfully be predicted using the bilinear hysteresis model of lead-rubber bearings. This model signified that the hybrid composites were stable and may give an indication when the steel fibers may begin yielding in compression. This model justified the experimental energy dissipation and residual strain ratio results.

- Overall, glass/steel fiber hybrid composites show promise in structural applications because of their high strength, energy absorption during loading, and re-centering capabilities, while maintaining a high strength-to-weight ratio. More research is needed to optimize the composite design to achieve higher failure strains.

5.3 Future Research

5.3.1 Off-axis Fiber Composites

This study comprised only of unidirectional glass and steel thin fibers. However, off-axis fiber fabrics, such as ±45°, more energy absorption may be possible using the in-plane shear effect. The failure mechanism will be matrix dominated and initiated by micro cracks. This may allow the fibers to rotate towards the loading direction, resulting in a higher elongation to failure and absorbing more energy. A compromise between stiffness and toughness must be found by varying fiber angles.

5.3.2 Corrosion Resistance of Hybrid Composites

A shortcoming of traditional construction materials includes corrosion under harsh environments. One major benefit of conventional fiber-reinforced polymer (FRP) composites comprised of non-metal fibers is corrosion resistance. Therefore, the addition of metal fibers to

these composites may present a concern to the industry. Although polymer resins have a high resistance to corrosive chemicals, the hybrid composites should be tested if they are to be used in structural applications.

5.3.3 Structural Member Application

The motivation behind this research was to introduce an alternative to conventional construction materials in civil infrastructure. The next phase of this research will involve manufacturing and testing of structural members comprised of this novel non-metal/metal hybrid composite.

REFERENCES

[1] Hollaway, L. C., 2010, "A Review of the Present and Future Utilisation of FRP Composites in the Civil Infrastructure with Reference to their Important In-Service Properties," Construction and Building Materials, 24(12), pp. 2419-2445.
[2] Mamalis, A. G., Manolakos, D. E., Ioannidis, M. B., and Papapostolou, D. P., 2005, "The Static and Dynamic Axial Collapse of CFRP Square Tubes: Finite Element Modelling," Composite Structures, 74(2), pp. 213-225.
[3] Echevarria, A., Zaghi, A. E., Christenson, R., and Accorsi, M., 2015, "CFFT Bridge Columns for Multihazard Resilience," ASCE Journal of Structural Engineering, XX(XX), pp. X-X.
[4] AASHTO, 2012, "LRFD Guide Specifications for Design of Concrete-Filled FRP Tubes, 1st Edition," AASHTO, Washington, D.C.
[5] Asgarinia, S., Viriyasuthee, C., Phillips, S., Dubé, M., Baets, J., Van Vuure, A., Verpoest, I., and Lessard, L., 2015, "Tension-tension Fatigue Behavior of Woven Flax/Epoxy Composites," Reinforced Plastics and Composites, 34(11), pp. 857-867.
[6] Bray, D. J., Dittanet, P., Guild, F. J., Kinloch, A. J., Masania, K., Pearson, R. A., and Taylor, A. C., 2013, "The modelling of the toughening of epoxy polymers via silica nanoparticles: The effects of volume fraction and particle size," Polymer, 54(26), pp. 7022-7032.
[7] Swolfs, Y., Meerten, Y., Hine, P., Ward, I., Verpoest, I., and Gorbatikh, L., 2015, "Introducing Ductility in Hybrid Carbon Fibre/Self-Reinforced Composites Through Control of the Damage Mechanisms," Composite Structures, 131, pp. 259-265.
[8] Tian, Z., Song, H., Wan, Z., and Du, X., 2001, "Fatigue Properties of Steel Cord-Rubber Composite," Journal of Elastomers and Plastics, 33, pp. 283-296.
[9] Ahmed, S. F. U., Maalej, M., and Paramasivam, P., 2007, "Analytical Model for Tensile Strain Hardening and Multiple Cracking Behavior of Hybrid Fiber-Engineered Cementitous Composites," Journal of Materials in Civil Engineering, 19(7), pp. 527-539.
[10] SA, N. B., 2013, "Stainless steel filler materials for plastics,"Belgium.
[11] Callens, M. G., Gorbatikh, L., and Verpoest, I., 2014, "Ductile Steel Fibre Composites with Brittle and Ductile Matrices," Composites: Part A, 61, pp. 235-244.
[12] Callens, M. G., De Cuyper, P., Gorbatikh, L., and Verpoest, I., 2015, "Effect of Fibre Architecture on the Tensile and Impact Behaviour of Ductile Stainless Steel Fibre Polypepylene Composites," Composite Structures, 119, pp. 528-533.
[13] Callens, M. G., Gorbatikh, L., Bertels, B., Smet, M., and Verpoest, I., 2015, "Tensile Behaviour of Stainless Steel Fibre/Epoxy Composites with Modified Adhesion," Composites: Part A, 69, pp. 208-218.
[14] Allaer, K., De Baere, I., Lava, P., Van Paepegem, W., and Degrieck, J., 2014, "On the in-plane mechanical properties of stainless steel fibre reinforced ductile composites," Composites Science and Technology, 100(21), pp. 34-43.
[15] Mosleh, Y., Clemens, D., Gorbatikh, L., Verpoest, I., and Van Vuure, A. W., 2015, "Penetration Impact Resistance of Novel Tough Steel Fibre-Reinforced Polymer Composites," Reinforced Plastics and Composites, 34(8), pp. 624-635.
[16] Faes, J. C., Rezaei, A., Van Paepegem, W., and Degrieck, J., 2015, "Influence of Matrix Toughness and Interfacial Strength on the Toughness of Epoxy Composites with Ductile Steel Fabric Reinforcement," 16th European Conference on Composite MaterialsSeville, Spain.

[17] Sinmazçelik, T., Avcu, E., Bora, M. O., and çoban, O., 2011, "A Review: Fibre Metal Laminates, background, bonding types and applied test methods," Materials and Design, 32(7), pp. 3671-3685.
[18] Botelho, E. C., Silva, R. A., Pardini, L. C., and Rezende, M. C., 2006, "Review on the Development and Properties of Continuous Fiber/Epoxy/Aluminum Hybrid Composites for Aircraft Structures," Materials Research, 9(3), pp. 247-256.
[19] Moussavi-Torshizi, S. E., Dariushi, S., Sadighi, M., and Safarpour, P., 2010, "A Study on Tensile Properties of a Novel Fiber/Metal Laminate," Materials Science and Engineering, 527(18-19), pp. 4920-4925.
[20] Technologies, F., "Along the Bond Line: Groundbreaking Aircraft Structures."
[21] Rubio-González, C., Velasco, F., and Martínez, J., 2015, "Analaysis of Notched Woven Composites and Fiber Metal Laminates with Previous Fatigue Damage," Journal of Composite Materials.
[22] Kretsis, G., 1987, "A Review of the Tensile, Compressive, Flexural and Shear Properties of Hybrid Fibre-Reinforced Plastics," Composites, 18(1), pp. 13-23.
[23] Swolfs, Y., Gorbatikh, L., and Verpoest, I., 2014, "Fibre Hybridisation in Polymer Composites: A Review," Composites: Part A, 67, pp. 181-200.
[24] Hayashi, T., "On the Improvement of Mechanical Properties of Composites by Hybrid Composition," Proc. 8th International Reinforced Plastics Conference, pp. 149-152.
[25] Hull, D., and Clyne, T. W., 1996, An Introduction to Composite Materials, Cambridge University Press, New Delhi, India.
[26] Marom, G., Fischer, S., Tuler, F. R., and Wagner, H. D., 1978, "Hybrid Effects in Composites: Conditions for Positive or Negative Effects Versus Rule-of-Mixtures Behaviour," Journal of Materials Science, 13(7), pp. 1419-1426.
[27] Gibson, R. F., 2010, "A Review of Recent Research on Mechanics of Multifunctional Composite Materials and Structures," Composite Structures, 92(12), pp. 2793-2810.
[28] Breuer, U. P., Schmeer, S., and Eberth, U., 2013, "Carbon and Metal Fiber Reinforced Airframe Structures- A New Approach to Composite Multifunctionality," German Aerospace CongressStuttgart, Germany.
[29] Ahmed, T. J., 2009, "Hybrid Composite Structures: Multifunctionality Through Metal Fibers," PhD, Technical University of Delft, Netherlands.
[30] Satish, K. G., Siddeswarappa, K., and Kaleemulla, K. M., 2010, "Characterization of In-Plane Mechanical Properties of Laminated Hybrid Composites," Journal of Minerals & Materials Characterization & Engineering, 9(2), pp. 105-114.
[31] Thysen, S., 2013, "Mechanical Behavior of Hybrid Steel and Glass Fibre Composites," Master of Science in Engineering, KU Leuven, Leuven, Belgium.
[32] De Bondt, S., and Decrop, J., 2007, "Bundle drawn stainless steel fibers," NV Bekaert SA, USA.
[33] Harik, V. M., Klinger, J. R., and Bogetti, T. A., 2002, "Low-cycle Fatigue of Unidirectional Composites: Bi-linear S-N curves," International Journal of Fatigue, 24(2-4), pp. 455-462.
[34] Hu, J. W., 2015, "Response of Seismically Isolated Steel Frame Buildings with Sustainable Lead-Rubber Bearing (LRB) Isolator Devices Subjected to Near-Fault (NF) Ground Motions," Sustainability, 7(1), pp. 111-137.

APPENDIX A: Manufacturer Material Data Sheets

HEXION

Technical Data Sheet

Re-issued September 2005

EPON™ Resin 826

Product Description

EPON™ Resin 826 is a low viscosity, light colored liquid bisphenol A based epoxy resin. It finds use in a variety of applications when crosslinked or hardened with appropriate curing agents.

Application Areas/Suggested Uses

- Fiber reinforced pipe and composites
- Tooling and molding compounds
- Construction, electrical and aerospace adhesives
- Electrical castings and laminates
- Chemical resistant high solids tank linings
- Flooring
- Grouting compounds

Benefits

- Low viscosity
- Low color
- Low ionic contamination
- Reacts with a full range of curing agents
- Produces high-strength cured systems resistant to chemical attack

Sales Specification

Property	Units	Value	Test Method/Standard
Weight per Epoxide	g/eq	178 – 186	ASTM D1652
Viscosity at 25°C	P	65 – 95	ASTM D445
Color	Gardner	1 max.	ASTM D1544

Typical Properties

Property	Units	Value	Test Method/Standard
Viscosity at 50°C	P	4.5	ASTM D445

Viscosity at 75°C	P	0.8	ASTM D445
Density at 25°C	lb/gal	9.7	ASTM D1475
Density at 25°C	g/ml	1.16	

Processing/How to use

General Information
The low viscosity and curing properties of EPON Resin 826 allow its use under various conditions and fabrication techniques. These include:

- Spraying and brushing
- Filament winding
- Pressure laminating
- Vacuum bag laminating
- Pultrusion
- Casting
- Molding
- Troweling

Benefits
EPON Resin 826 can be crosslinked with a variety of curing agents/depending on processing conditions and properties desired for the finished product. A guide to selecting curing agents for combination with EPON Resin 826 for various applications given in technical bulletin SC:235-01.828.

EPON 826 is commonly used to fabricate high strength fiber reinforced pipes and composites. The low viscosity of the resin provides rapid wetout of a wide range of reinforcing fibers including glass, graphite, aramid and boron. High fiber content with low void content can be achieved with this resin. Structural composites such as this have a high ratio of strength to weight. This makes them suitable for applications ranging from sporting goods equipment to aerospace structural members.

EPON Resin 826 systems are also excellent electrical insulators. Such systems are used frequently in electrical encapsulations, laminates and molding compounds.

Structures, linings and coatings made with EPON Resin 826 protect metal surfaces and resist attack from acids, bases, solvents and fuel. They find use in the oil, gas, mining and chemical industries.

The higher shear strength obtained with EPON Resin 826 adhesives is due in part to the low internal stresses inherent in cured epoxy resins. Such adhesives are used to bond a broad range of substrates..

FDA
Several paragraphs of Title 21 of the Code of Federal Regulations permit and regulate the use of epoxy resins such as cured EPON Resin 826 as indirect food additives in food contact applications. Examples are: 175.105 and 175.300.

HEXION

Technical Data Sheet

Re-issued September 2005

EPON™ Resin 828

Product Description

EPON™ Resin 828 is an undiluted clear difunctional bisphenol A/epichlorohydrin derived liquid epoxy resin. When cross-linked or hardened with appropriate curing agents, very good mechanical, adhesive, dielectric and chemical resistance properties are obtained. Because of this versatility, EPON Resin 828 has become a standard epoxy resin used in formulation, fabrication and fusion technology.

Benefits

- Fiber reinforced pipes, tanks and composites
- Tooling, casting and molding compounds
- Construction, electrical and aerospace adhesives
- High solids/low VOC maintenance and marine coatings
- Electrical encapsulations and laminates
- Chemical resistant tank linings, flooring and grouts
- Base resin for epoxy fusion technology

Sales Specification

Property	Units	Value	Test Method/Standard
Weight per Epoxide	g/eq	185 – 192	ASTM D1652
Viscosity at 25°C	P	110 – 150	ASTM D445
Color	Gardner	1 max.	ASTM D1544

Typical Properties

Property	Units	Value	Test Method/Standard
Density at 25°C	lb/gal	9.7	ASTM D1475
Denisty at 25°C	g/ml	1.16	
Vapor pressure @ 25°C (77° F)	mm Hg	0.03	
Refractive index @ 25°C (77° F)		1.573	
Specific heat	BTU/lb/°F	0.5	

Processing/How to use

General Information
The low viscosity and cure properties of EPON Resin 828 allow its use under various application and fabrication techniques including:

• Spraying and brushing	• Pultrusion
• Filament winding	• Casting
• Pressure laminating	• Molding
• Vacuum bag laminating	• Toweling

Curing Agents
EPON Resin 828 can be cured or cross-linked with a variety of curing agents depending on properties desired in the finished product and the processing conditions employed. Some commonly used curing agents, recommended concentrations, typical cure schedules employed in major end-use applications, plus sources for these curing agents are displayed in Table 1.

Performance Properties
Perfomance Characteristics of Cured EPON Resin 828
Mechanical Properties
High performance, high strength materials are obtained when this resin is cured with a variety of curing agents. Unfilled systems in common use have tensile values greater than 10,000 psi (69 MPa) with modulus values greater than 400,000 psi (2750 MPa). Such systems are normally very rigid. If greater flexibility is needed systems can be formulated to provide up to 300% elongation.

Adhesive Properties
One of the most widely recognized properties of cured EPON Resin 828 is strong adhesion to a broad range of substrates. Such systems exhibit shear strength of up to 6,000 psi (41 Mpa). One factor which contributes to this property is the low shrinkage shown by these systems during cure. Compared to other polymers, epoxy resins have low internal stresses resulting in strong and durable finished products.

Electrical Properties
EPON Resin 828 cured systems have very good electrical insulating characteristics and dielectric properties. For example, systems can be obtained with anhydride and amine curing agents having volume resistivities up to 1 x 10E16 ohm-cm, dielectric constants of 3-5 and dissipation factors of 0.002 to 0.020 at ambient conditions. Electrical encapsulations, laminates and molding compounds are frequently based on EPON Resin 828.

Chemical Resistance
Cured EPON Resin 828 is highly resistant to a broad range of chemicals, including caustic, acids, fuels and solvents. Chemically resistant reinforced structures and linings or coatings over metal can be formulated with EPON Resin 828.

Formulating Techniques
The primary components of a thermosetting resin formula are the epoxy resin and the hardener or curing

HEXION

Technical Data Sheet

Issued: September 2010

EPIKOTE™ Resin 874L-X-90

Product Description

EPIKOTE Resin 874L is a Bisphenol-A based epoxy resin solution that has been modified to improve flexibility and to reduce solution viscosity. The standard product is supplied as a 90% wt solution in Xylene (EPIKOTE Resin 874L-X-90). This resin solution is ideally suited to formulate ambient temperature curing systems with significantly lower levels of Volatile Organic Compounds (VOC) when compared to conventional solvent-borne epoxy-polyamide systems.

In ambient cure applications, EPIKOTE 874L-X-90 out-performs standard liquid epoxy resin grades with respect to flexibility of the epoxy coating; as well as, standard solid epoxy resin grades with respect to solvent emissions from the coating formulation. This epoxy resin solution can be combined with the full range of curing agents typically used for liquid epoxy resins. It is recommended for use with high performance types as Mannich bases, cycloaliphatic polyamines and low viscosity polyamides.

Application Areas/Suggested Uses

EPIKOTE 874L-X-90 is designed for use in high solids, ambient cure epoxy coatings and is suitable for use in either epoxy primers or topcoats in these applications:

- Industrial maintenance (protective coatings)
- Marine coatings
- Industrial finishes

Benefits

- Complies with stringent VOC requirements (<100 g/L VOC)
- Offers the potential for cost savings
- Very good flexibility and corrosion resistance
- Easy application by roller, brush or spray

Cost Savings

Conventional solid resin based systems typically have VOC emission levels of ~450 g/l at application viscosity. The current VOC emission limit for marine and maintenance applications in many European countries and in the USA is 340 g/L and in some cases even down to 250 g/Ll. EPIKOTE 874-X-90 enables the formulation of high-solids paints with VOC emission levels down to less than 100 g/L. Since EPIKOTE 874-X-90 can meet both current and future VOC legislation; the customer can avoid future re-formulation costs. Lower VOC emissions correspond with solvent cost savings. Significant savings are also achieved by reduced labor costs. Paints with higher volume solids content require fewer spraying cycles to achieve

the desired dry film thickness. Packaging, transportation and storage cost savings are achieved because of the very high solids content of the paint. Finally, the versatility of EPIKOTE 874-X-90 makes it a viable alternative to both solid and liquid resin grades in many different applications. This offers many opportunities for grade range rationalization and inventory cost reduction

Sales Specifications

Property	Units	Value
Epoxy Number	%	15.9 – 18.7
Epoxy Equivalent Wt*	g/eg	230 - 270
Viscosity @ 25°C *	mPa.s **	2100 –2300
Solids	% m/m	89 - 91
Color, Gardner		3 max

* Number of grams of resin containing 1 equivalent of epoxide (Weight per equivalent, WPE, is alternative term)
** 1mPa.s = centipoise

Typical Properties

Property	Units	Value
Density Solution 25°C	kg/l	1.07 – 1.17
Solvent		Xylene

Performance details

The table below shows the performance of EPIKOTE Resin 874L-X-90 compared to a standard solid solution resin grade in a red iron oxide anticorrosion primer.

PROPERTY	Unit	EPIKOTE 874L-X-90*	EPIKOTE 874L-X-90*	EPIKOTE Resin 1001-X-75**
EPIKURE™ Curing agent		3155	195	3115-X-70
Pigment volume concentration	%	27	30	30
Solids (%wt) at application viscosity	%	80	83	60
Volatile Organic Compounds (VOC)	g/L	<250	<250	<450
Pot life	Hours	4	4	8
Application viscosity	Pa.s	0.2-0.3	0.2-0.3	0.2-0.3
Dry film thickness	mm	75	75	130
Number of coating layers		1	1	4
Corrosion resistance				
Salt spray 1500 hrs		F2-M6	F8-F4	F2-M6
Chemical resistance				
10% Sodium hydroxide		10	F6 at bottom	10
10% Sulphuric acid		170 hrs. VD8 at bottom	170 hrs. FM4	96 hrs. Delamination
10% Acetic acid		24 hrs. MD8	170 hrs. M4	29 hrs. Delamination
Solvent resistance				
Xylene (1500 hrs.)		10	10	10

MIBK (1200 hrs.)	10	Glossy	10	Glossy	10	Loss of gloss

? Paint formulation similar to EPIKOTE Technical Bulletin EK 2.2.4.6
?? Paint formulation similar to EPIKOTE Technical Bulletin EK 2.2.4.1

Safety, Storage & Handling
Please refer to the MSDS for the most current Safety and Handling information.

Please refer to the Hexion web site for Shelf Life and recommended Storage information.

For literature and technical assistance, visit our website at: www.hexion.com/epoxy

PDS-9272- (Rev.5/26/2015 7:40:16 PM)

HEXION

Technical Data Sheet

Re-issued August 2005

EPIKURE™ Curing Agent 3055

Product Description

EPIKURE™ Curing Agent 3055 is an aliphatic amidoamine. Due to its versatility and convenient working characteristics, it should be considered for room temperature curing applications for epoxy resins and in many applications where elevated temperature curing cycles can be used. When EPIKURE 3055 is used as the sole crosslinker, the combining ratio with an epoxy resin can be varied to obtain a wide range of properties. It may also be used in conjunction with other curing agents to vary properties or curing rates.

Application Areas/Suggested Uses

- Adhesives
- Laminating binders
- Electrical encapsulants
- Grouts
- Floor topping and repair compositions

Benefits

- Low viscosity
- Complete compatibility with conventional epoxy resins
- Extended pot life
- Wide range of combining ratios

Sales Specification

Property	Units	Value	Test Method/Standard
Amine value	g/eq	449-473	ASTM D2896
Viscosity at 25°C	cP	150-300	ASTM D2196
Color	Gardner	<13	ASTM D1544

Typical Properties

Property	Units	Value	Test Method/Standard
Equivalent weight, approx.		90	
Pounds/gallon @ 25 °C	lbs/gal	7.87	ASTM D1475

General Information

EPIKURE Curing Agent 3055 is usually recommended for use with EPON™ Resin 828 at a ratio of 50 parts per 100 parts of resin, but it can be used within a range of 40 to 100 parts per 100 parts of resin, depending on the desired properties of the cured product. Increasing the amount of EPIKURE 3055 improves toughness and flexibility at the expense of tensile strength, moisture resistance and electrical properties particularly at elevated temperatures. Several representative formulations are described in Table 1. For applications requiring very low viscosity, a part or all of the EPON 828 can be replaced with a reactive diluent such as HELOXY™ Modifier 61. As shown in Table 1, such substitution is accompanied by some change in the properties of the cured resin.

As with all room temperature curing epoxy resin systems, the gel time and exothermic temperature rise for an epoxy resin composition containing EPIKURE Curing Agent 3055 depend on the size of the batch, the amount and type of filler loading, the ratio of resin to curing agent and the mixing temperature. Cure time at room temperature depends to a large extent on the exothermic temperature rise. In thin sections where exothermic heat is readily dissipated, an overnight cure is required for the composition to reach handling strength and full cure is reached within several days.

Developed primarily to cure epoxy resins at room temperature, EPIKURE Curing Agent 3055 can also be used at elevated temperatures. Since elevated temperatures greatly reduce the cure time, the cure schedule should be carefully watched. A comparison of the physical properties of samples cured at room temperature as well as at 100 °C is listed in Columns B and H in Table 1. Except for heat deflection temperature, differences in properties are small, indicating that even though cure may not be complete at room temperature, it is satisfactory for many applications.

Performance Properties

Table 1 / **Properties of Systems Cured with EPIKURE™ Curing Agent 3055**

	Method	Units	A	B	C	D [1]	E	F	G	H
EPON™ Resin 828		pbw	100	100	100	100	100	90	80	100
HELOXY™ Modifier 61		pbw	---	---	---	---	---	10	20	---
EPIKURE Curing Agent 3055		pbw	40	50	60	82	100	50	50	50
			---	---	---	---	---	---	---	---
Handling Properties @ 25°C			---	---	---	---	---	---	---	---
Initial viscosity		cP	2,500	1,900	1,700	1,300	1,000	550	225	1,900
Gel Time, 100 gram mass		minutes	---	240	---	---	---	---	---	---

Property	Test Method	Unit	E-Glass	Advantex® ECR glass	OC™ H-Glass	OC™ AR-Glass
Fiber and Bulk Glass Properties						
Density (bulk annealed)	ASTM C693	g/cm^3	2.63-2.64	2.66	2.65	2.74
Fiber Density (predicted)	Proprietary	g/cm^3	2.60-2.62	2.63	2.6	2.63
Refractive Index (bulk annealed)	Proprietary	-	1.562-1.565	1.567	1.558	1.566
Abbe Number (bulk annealed)	Proprietary	-	59.2-59.5	58	59.4	51.9
Mechanical Properties						
Vickers Hardness	Vickers Indenter	-	614-639	626	675	617
Pristine Fiber Tensile Strength . 22 °C	Based on ASTM D3822. using an extension rate of 2%/min*	MPa	3815-3830	4050	4635	3525
Specific Pristine Strength	Calculation	MJ/kg	1.45-1.46	1.53	1.78	1.29
Specific Pristine Strength	Calculation	$\times 10^5$ m	1.48-1.49	1.56	1.81	1.31
Young's Modulus. 22 °C	Proprietary	GPa	78-79	82	87.5	77.5
Specific Modulus	Calculation	MJ/kg	29.9	30.9	33.5	28.4
Specific Modulus	Calculation	$\times 10^6$ m	3.05	3.15	3.41	2.89
Elongation at Break	*Based on ASTM D3822	%	3	3	3.2	2.8
Thermal Properties						
Coefficient of Thermal Expansion. 50-300 °C	ASTM E228	$\times 10^{-6}$ cm/cm•°C	5.9-6.6	6.6	6.3	9.9
Specific Heat @ 23 °C	ASTM C832	kJ/kg•K	0.807	0.79	/	/
Strain Point (Log 14.5 poise)	ASTM C336	°C	631-632	680	648	598
Annealing Point (Log 13 poise)	ASTM C336	°C	670-671	722	685	642
Electrical Properties						
Conductivity	ASTM C177	watts/m•K	1.0-1.3	1.22	/	/
Dielectric Constant @ ~1 GHz	Interpolation using Split post resonator method	-	6.99-7.07	7.16	6.68	/
Loss tan δ @ ~1 GHz	Interpolation using Split post resonator method	-	0.0055-0.0065	0.0061	0.0059	/
Dielectric Constant @ ~10 GHz	Interpolation	-	6.90-6.97	7.07	6.6	/
Loss tan δ @ 10 GHz	Interpolation	-	0.0053-0.0064	0.0059	0.0054	/
Dielectric Constant @ ~20 GHz (19.77 GHz avg actual)	IPC-TM-650 2.5.5.13 Split cavity resonator	-	6.89-6.95	7.06	6.58	/
Loss tan δ @ 20 GHz	IPC-TM-650 2.5.5.13 Split cavity resonator	-	0.0053-0.0064	0.0059	0.0054	/
Fiber Weight Loss @ 96 °C. 24 hours. 17 µm fiber						
10% HCl		%	31.7	7.9	7.6	/
10% H_2SO_4		%	32.0	6.9	6.5	/
1 N Nitric		%	23.5	7.2	6.7	/

Technical Data Sheet

LOCTITE® 4014™

February 2010

PRODUCT DESCRIPTION

LOCTITE® 4014™ provides the following product characteristics:

Technology	Cyanoacrylate
Appearance (uncured)	Transparent, colorless to slightly yellow liquid[LMS]
Components	One part - requires no mixing
Viscosity	Very low
Cure	Humidity
Application	Bonding
Key Substrates	Plastics and Metals

LOCTITE® 4014™ is designed to provide fast room temperature fixturing and is also suitable for applications where heat resistance is required. Suitable for use in the assembly of **disposable medical devices**.

ISO-10993

An ISO 10993 Test Protocol is an integral part of the Quality Program for LOCTITE® 4014™. LOCTITE® 4014™ has been qualified to Henkel's ISO 10993 Protocol as a means to assist in the selection of products for use in the medical device industry. Certificates of Compliance are available on Henkel's website or through the Henkel Quality Department.

TYPICAL PROPERTIES OF UNCURED MATERIAL

Specific Gravity @ 25 °C	1.1
Flash Point - See SDS	
Viscosity, Cone & Plate, mPa·s (cP):	
Temperature: 25 °C, Shear Rate: 100 s^{-1}	1 to 4[LMS]
Viscosity, Brookfield - LVF, 25 °C, mPa·s (cP):	
Spindle 1, speed 30 rpm,	1 to 5

TYPICAL CURING PERFORMANCE

Under normal conditions, the atmospheric moisture initiates the curing process. Although full functional strength is developed in a relatively short time, curing continues for at least 24 hours before full chemical/solvent resistance is developed.

Cure Speed vs. Substrate

The rate of cure will depend on the substrate used.

Fixture Time, seconds:	
PVC to PVC	60 to 80
ABS to ABS	5 to 10
Polycarbonate to Polycarbonate	20 to 25
Polyurethane to Polyurethane	8 to 10
G-10 Epoxy to G-10 Epoxy	25 to 30
Stainless steel to PVC	5 to 10
Stainless steel to ABS	5 to 10
Stainless steel to Polycarbonate	5 to 8
Stainless steel to Polyurethane	20 to 25
Stainless steel to G-10 Epoxy	6 to 10

Cure Speed vs. Bond Gap & Humidity

The rate of cure will depend on the bondline gap. Thin bond lines result in high cure speeds, increasing the bond gap will decrease the rate of cure. The rate of cure is also influenced by the ambient relative humidity; the higher the relative humidity, the greater the cure speed.

Cure Speed vs. Activator

Where cure speed is unacceptably long due to large gaps, applying activator to the surface will improve cure speed. However, this can reduce ultimate strength of the bond and therefore testing is recommended to confirm effect.

TYPICAL PROPERTIES OF CURED MATERIAL

Cured for 24 hours @ 22 °C

Physical Properties:

Shore Hardness, ISO 868	65
Elongation, ISO 527-2, %	2
Tensile Strength, ISO 527-3	28 (4,000)

TYPICAL PERFORMANCE OF CURED MATERIAL

Adhesive Properties

Cured for 10 seconds @ 22 °C

Tensile Strength, ISO 6922:

Buna-N	N/mm²	≥6.9[LMS]
	(psi)	(≥1,000)

Cured for 24 hours @ 22 °C

Lap Shear Strength, ISO 4587:

PVC to PVC	N/mm²	>7.5
	(psi)	(>1,100)
ABS to ABS	N/mm²	>4
	(psi)	(>580)
Polycarbonate to Polycarbonate	N/mm²	>7.5
	(psi)	(>1,100)

MANUFACTURERS OF
ELECTRICAL INSULATION MATERIALS

INSULATING COMPONENTS FOR POWER SYSTEMS EQUIPMENT

The Gund Company, Inc
St. Louis, Missouri – USA
TEL - 314.423.5200
FAX - 314.423.9009

MATERIAL DATA SHEET

Item: NEMA Grade G-10 Glass Epoxy Laminate

Description: NEMA Grade G-10 material is a continuous filament woven fiberglass sheet bonded with epoxy resin. The material has the ability to maintain excellent mechanical, electrical, and physical properties at elevated temperatures to 130°C. NEMA G-10 is a non-brominated, non-flame retardant grade of glass epoxy laminate.

Please note that much of the industry refers to "G-10" material when they want a flame retardant, V-0 rated glass epoxy laminate rated at 130°C RTI such as NEMA FR4. Technically, NEMA G-10 is a non-flame retardant, non-brominated version of glass epoxy laminate. If a non-brominated material is required, please specifically address this issue.

Standards:

NEMA LI-1	Grade FR4
IEC 60893	EP GC 201
MIL-I-24768	27 GEE

Availability:

		English Units	SI Units
Laminate Sheets:	Thickness:	.006" to 5.0"	0.15 mm to 127 mm
	Sheet Sizes:	36" x 48", 39" x 48"	91.4 cm x 122 cm, 99 cm x 122 cm
		36" x 72", 48" x 48"	91.4 cm x 182.2 cm, 122 cm x 122 cm
		48" x 96", 48" x 108"	122 cm x 243.8 cm, 122 cm x 274.3 cm

Convolute Tubing: Available in an infinite number of inner diameter/outer diameter combinations as per customer requirements.

Fabricated Parts: The Gund Company custom fabricates insulation materials to the exact specifications and drawings of our customers

Key Characteristics	Test Method	Units - English (SI)	Typical Values
Specific Gravity	--	lb./in.^{3} (g/cc)	0.064 (1.77)
Rockwell Hardness (.50")	--	M Scale	99
Tensile Strength (.125") LW CW	ASTM D-638	psi (MPa)	43,000 (296) 39,000 (269)
Compressive Strength, Flatwise (.50")	ASTM D-695	psi (MPa)	44,000 (303)
Flexural Strength (.062") LW CW	ASTM D-790	psi (MPa)	66,000 (455) 60,000 (413)
Flexural Modulus (.062") LW CW	ASTM D-790	ksi (MPa)	3,400 (23,442) 3,300 (22,753)
Shear Strength, Perpendicular (.062")	ASTM D-732	psi (MPa)	19,000 (130)
IZOD Impact Strength LW CW	ASTM D-256	ft.-lbs./in. Notched	9.5 7.5
Dielectric Strength (.062") Condition A D-48/50	ASTM D-149	V/mil	960 1,000
Breakdown Voltage (.062") Condition A D-48/50	ASTM D-149	kV	66 65

APPENDIX B: Raw Data

B.1 Epoxy Testing

EPON 826 – Room Temperature

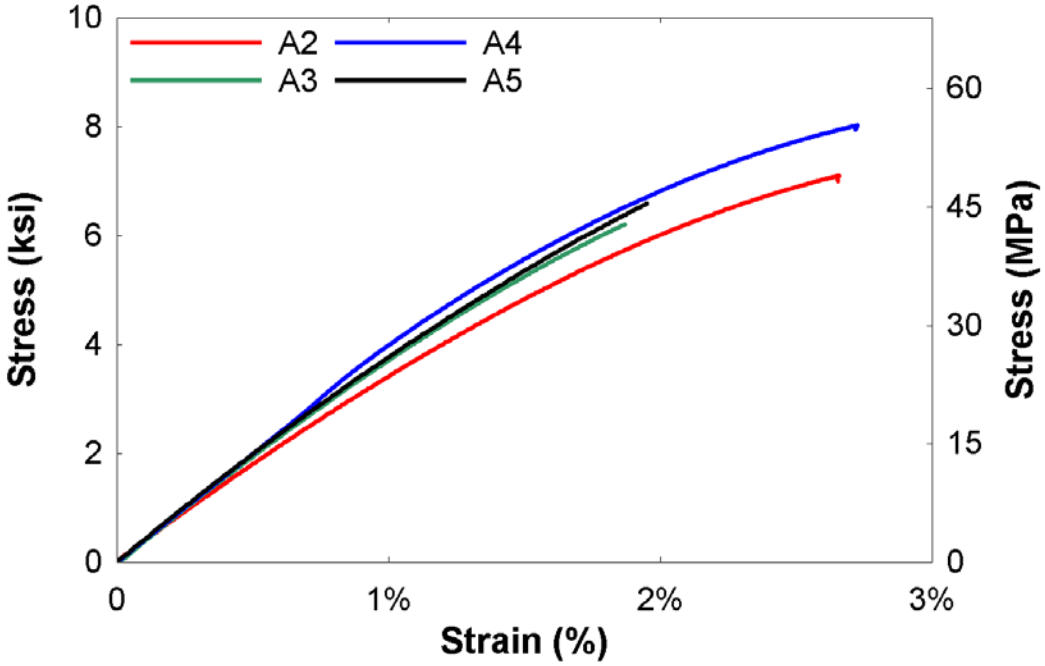

Figure B.1-1: Stress-strain relationship of EPON 826 (Sample A) Specimens cured at room temperature
*Note: A1 was conducted as a practice test and no raw data was collected

EPON 828 – Room Temperature

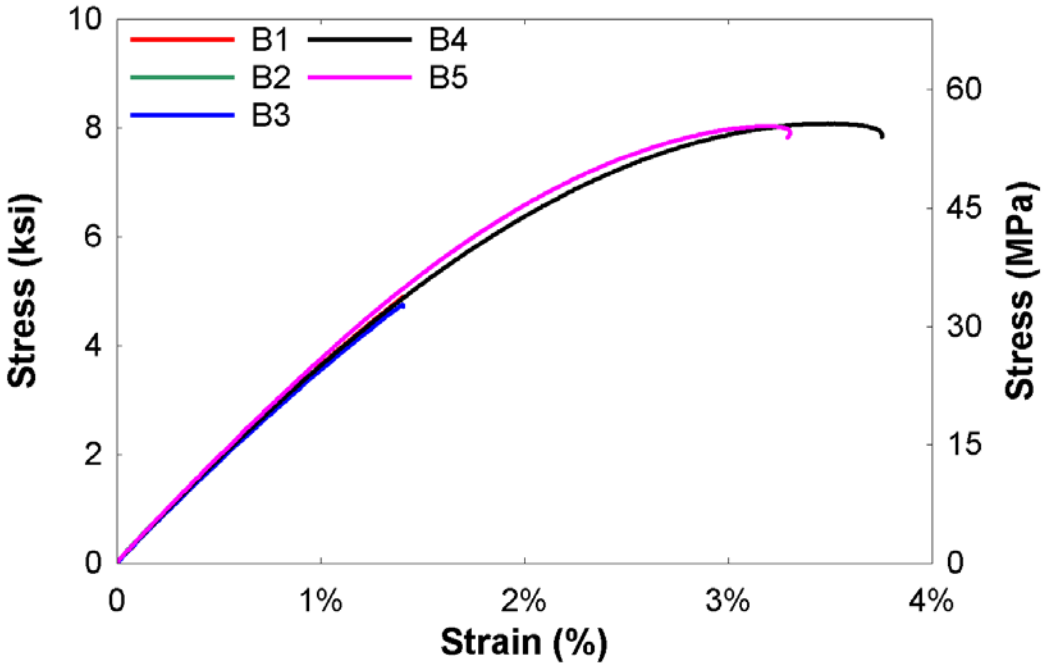

Figure B.1-2: Stress-strain relationship of EPON 828 (Sample B) Specimens cured at room temperature
*Note: B1 failed prematurely and was not included in the average calculations of the mechanical properties

EPIKOTE 874 – Room Temperature

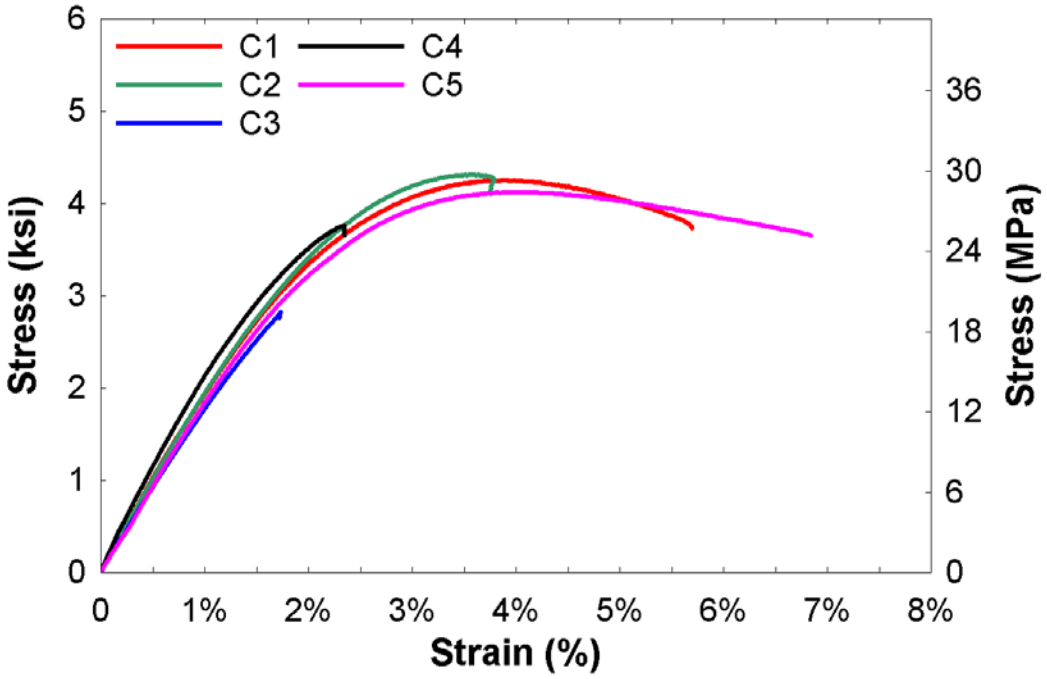

Figure B.1-3: Stress-strain relationship of EPIKOTE 874 (Sample C) Specimens cured at room temperature
*Note: C3 failed prematurely and was not included in the average calculations of the mechanical properties

EPON 828 – Heat Cured

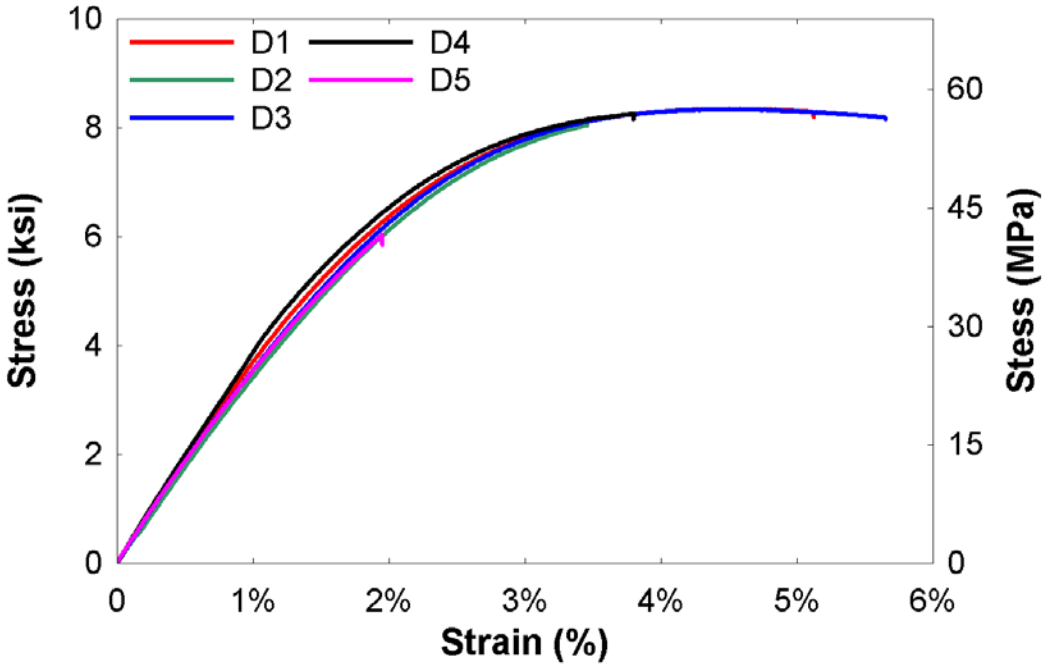

Figure B.1-4: Stress-strain relationship of EPON 828 (Sample D) Specimens cured at 200°F
*Note: D5 failed prematurely and was not included in the average calculations of the mechanical properties

B.2 Non-hybrid Composite Testing

Unidirectional Glass

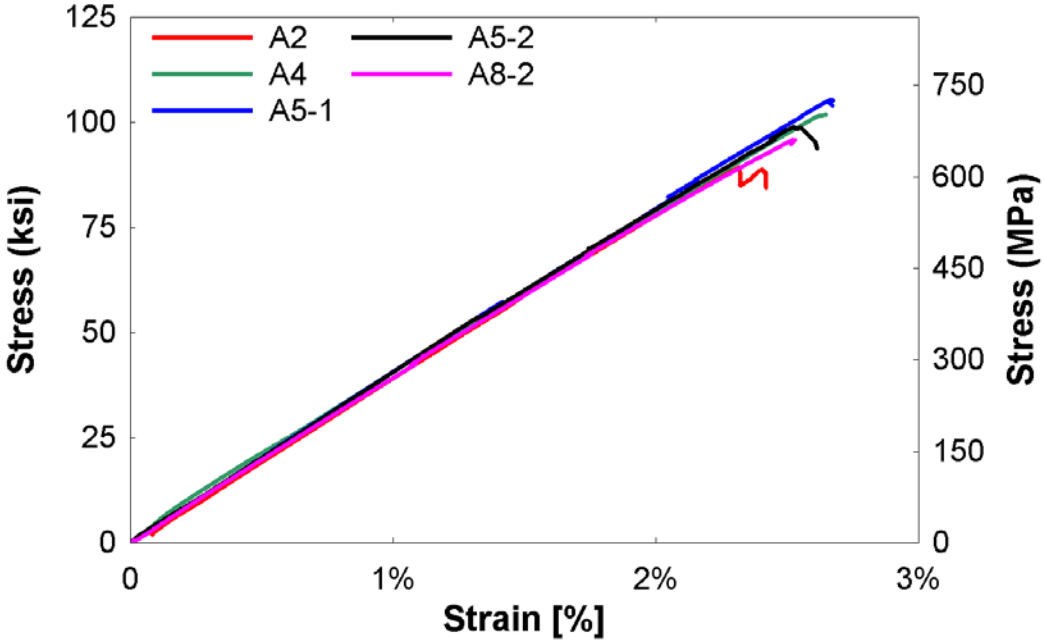

Figure B.2-1: Stress-strain relationship of unidirectional glass composite (Sample A) specimens under monolithic tensile loading

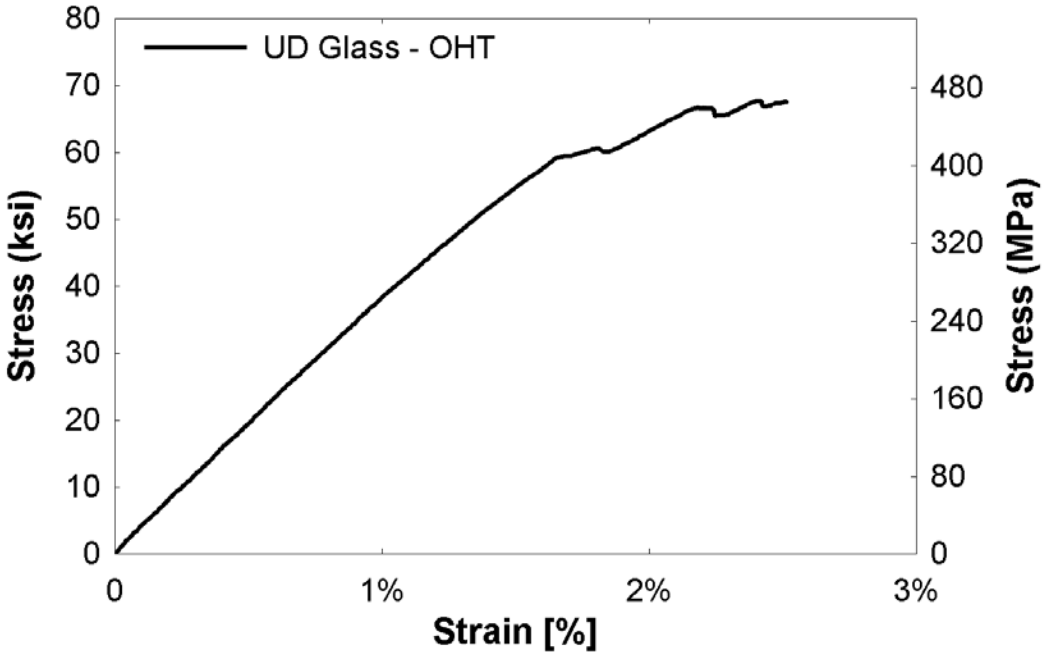

Figure B.2-2: Stress-strain relationship of unidirectional glass composite (Sample A) specimens under open-hole monolithic tensile loading

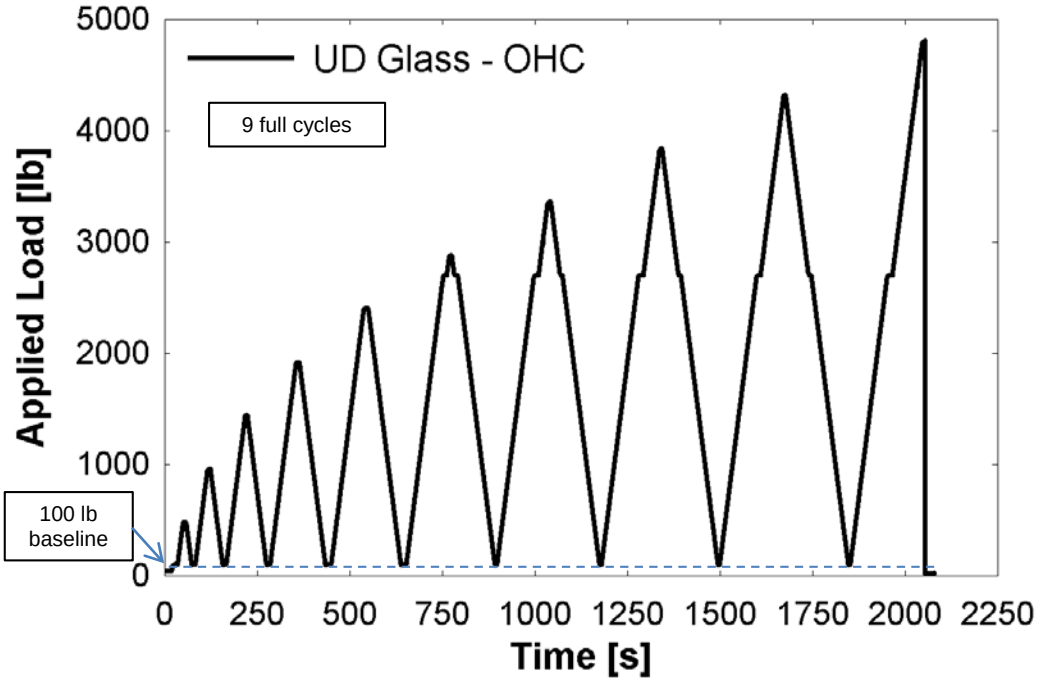

Figure B.2-3: Loading protocol of unidirectional glass composite (Sample A) specimens under open-hole half cyclic loading; each cycle increased by 10% of ultimate open-hole tensile strength.

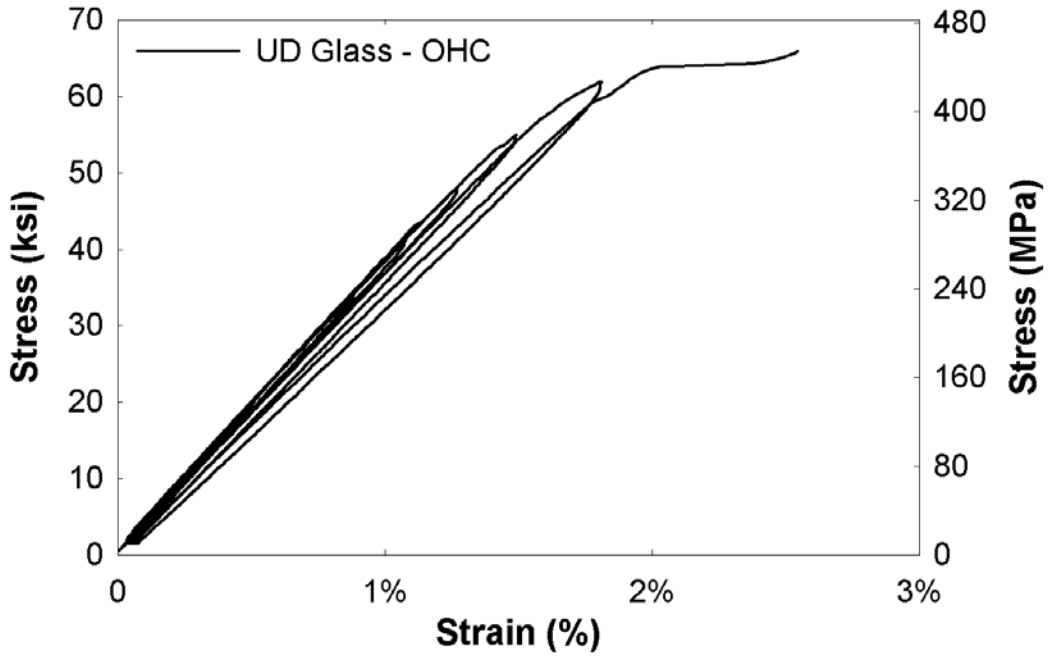

Figure B.2-4: Stress-strain relationship of unidirectional glass composite (Sample A) specimens under open-hole half cyclic tensile loading

Unidirectional Steel

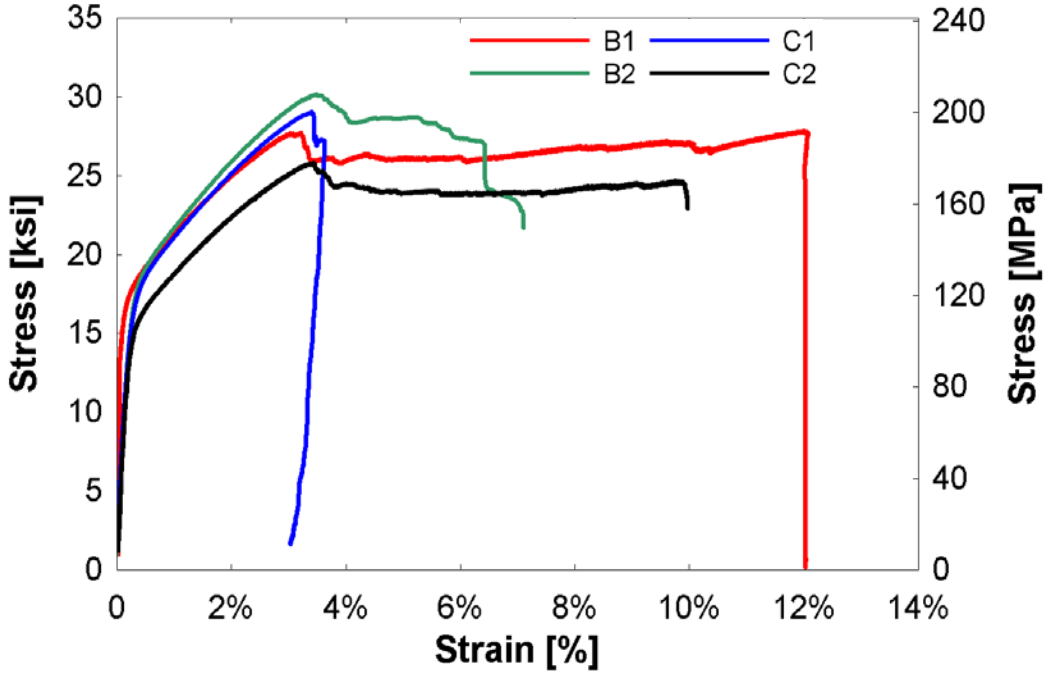

Figure B.2-5: Stress-strain relationship of unidirectional steel fiber composite specimens under monolithic tensile loading. Sample B represents bonded specimens and Sample C represents debonded specimens.
*Note 1: C1 failed prematurely and was not included in the average calculations of the mechanical properties

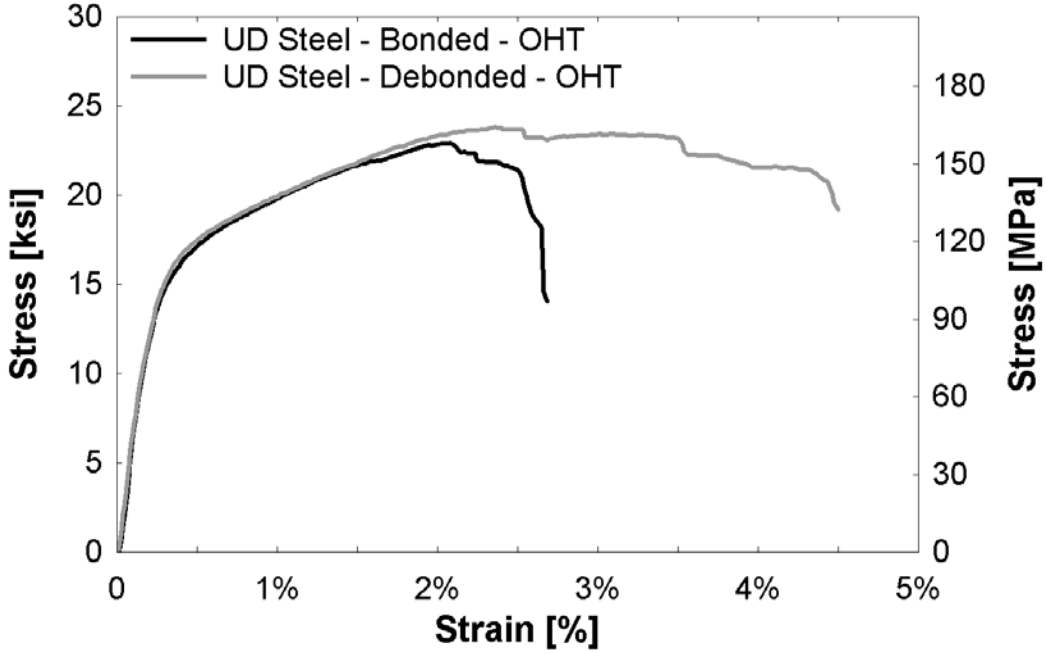

Figure B.2-6: Stress-strain relationship of unidirectional steel fiber composite specimens under open-hole monolithic tensile loading.

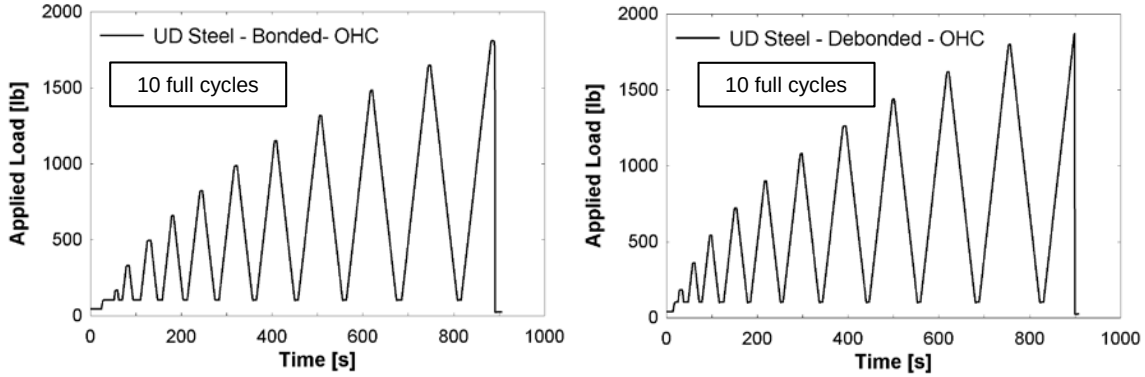

Figure B.2-7: Loading protocol of unidirectional steel fiber composite (Sample B, C) specimens under open-hole half cyclic loading; each cycle increased by 10% of ultimate open-hole tensile strength

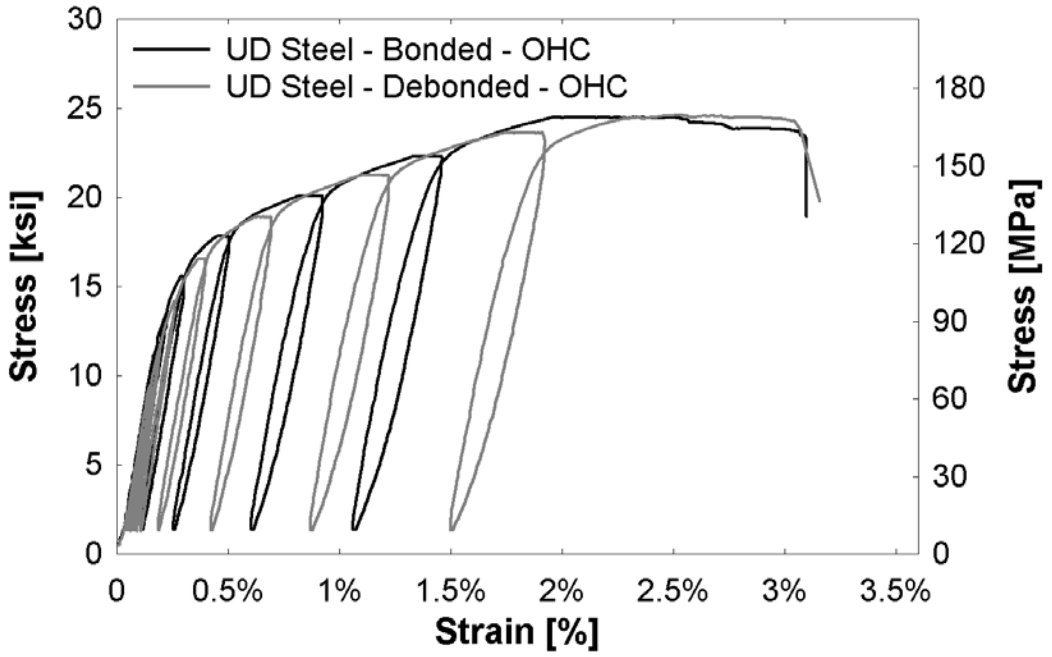

Figure B.2-8: Stress-strain relationship of unidirectional steel fiber composite (Sample B, C) specimens under open-hole half cyclic tensile loading

Steel Mesh

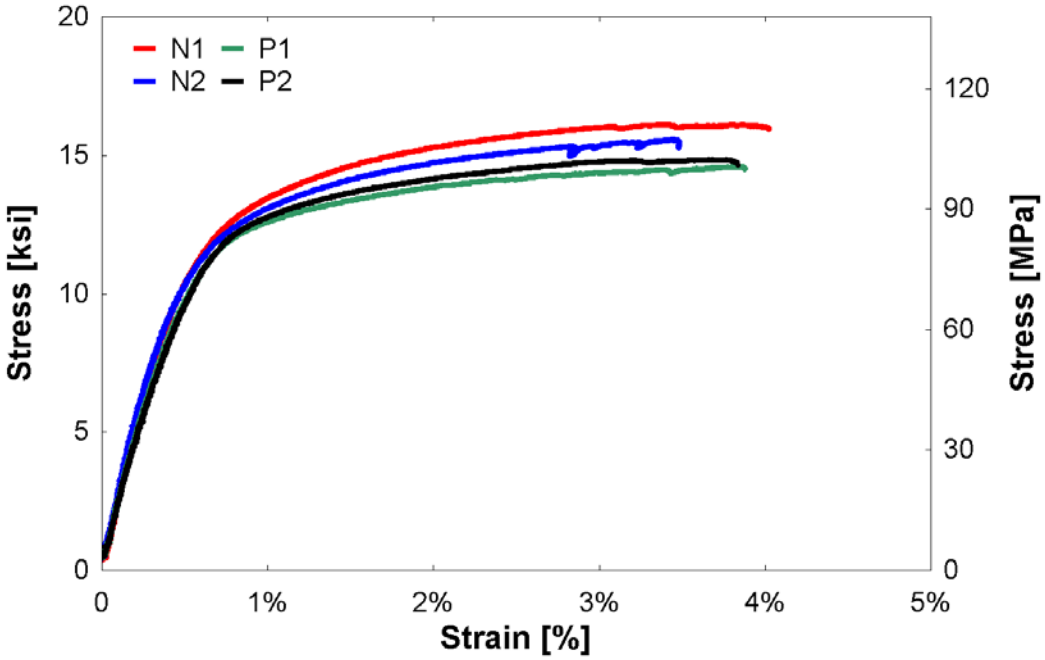

Figure B.2-9: Stress-strain relationship of steel mesh composite specimens under monolithic tensile loading. Sample N represents bonded specimens and Sample P represents debonded specimens.

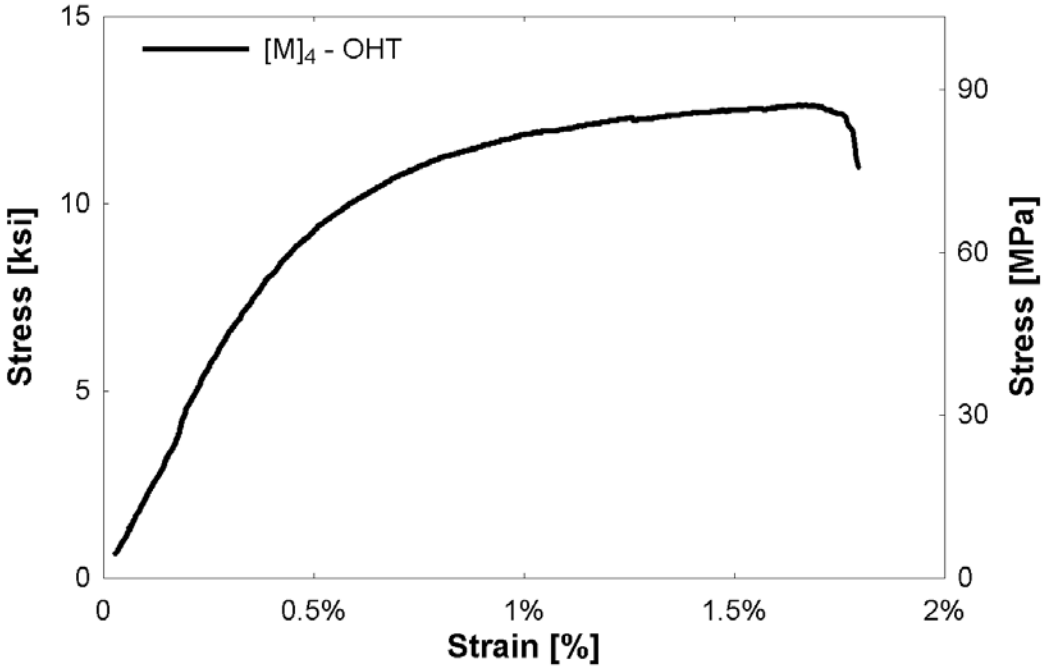

Figure B.2-10: Stress-strain relationship of steel mesh composite (Sample N) specimen under open-hole monolithic tensile loading.

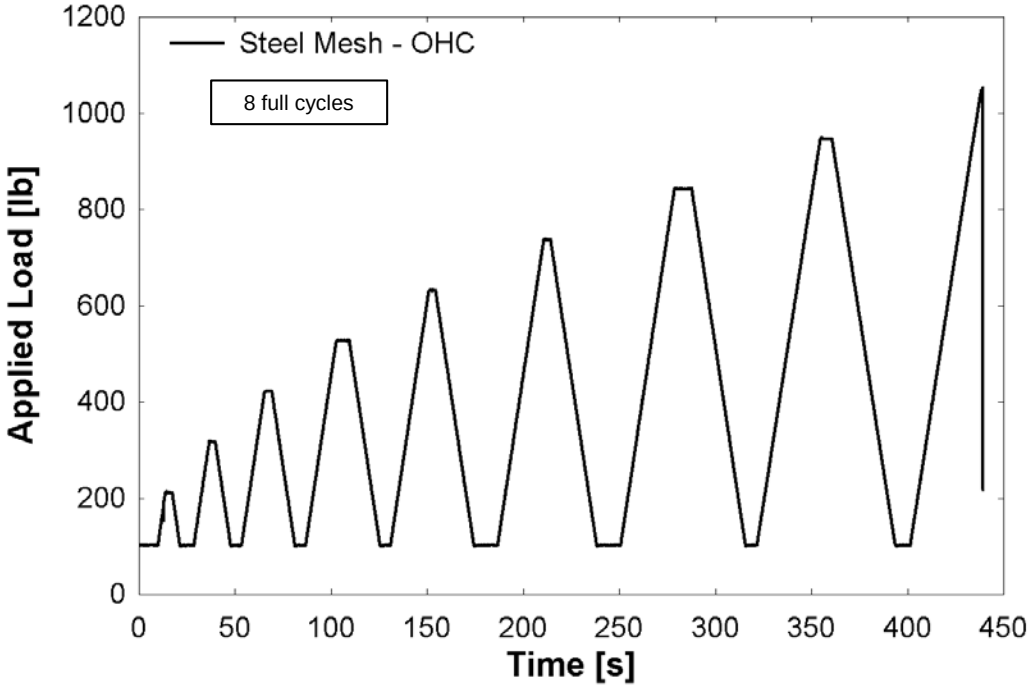

Figure B.2-11: Loading protocol of steel mesh composite (Sample P) specimen under open-hole half cyclic loading; each cycle increased by 10% of ultimate open-hole tensile strength

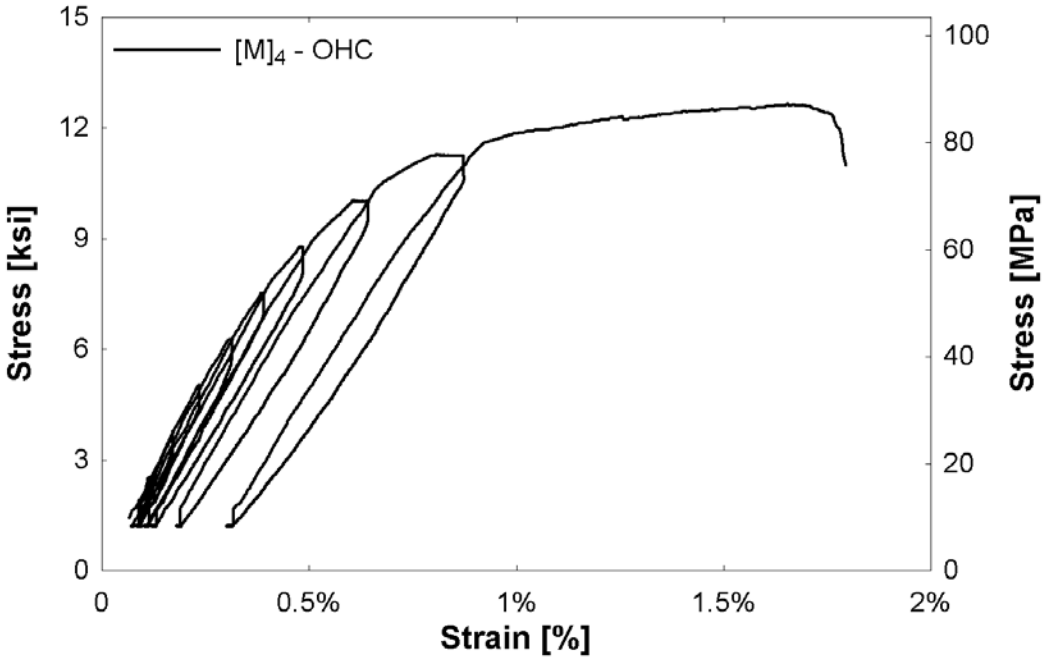

Figure B.2-12: Stress-strain relationship of unidirectional steel fiber composite (Sample P) specimen under open-hole half cyclic tensile loading

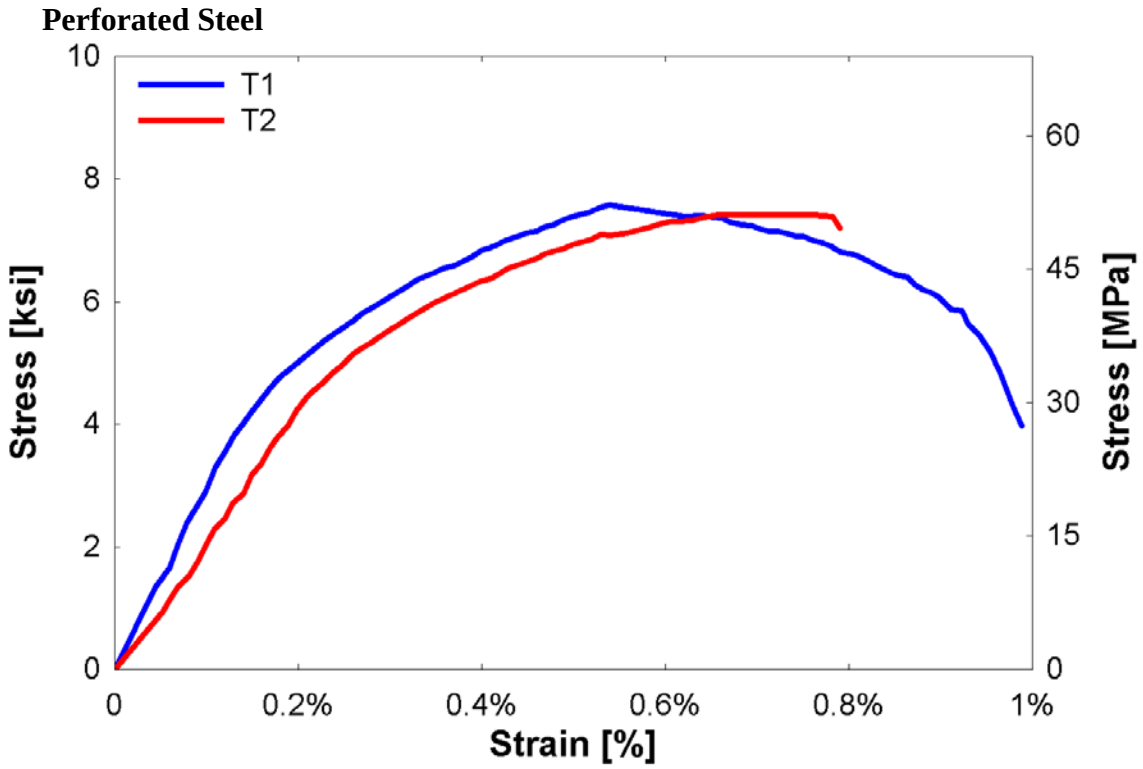

Figure B.2-13: Stress-strain relationship of perforated steel composite (Sample T) specimens under monolithic tensile loading.

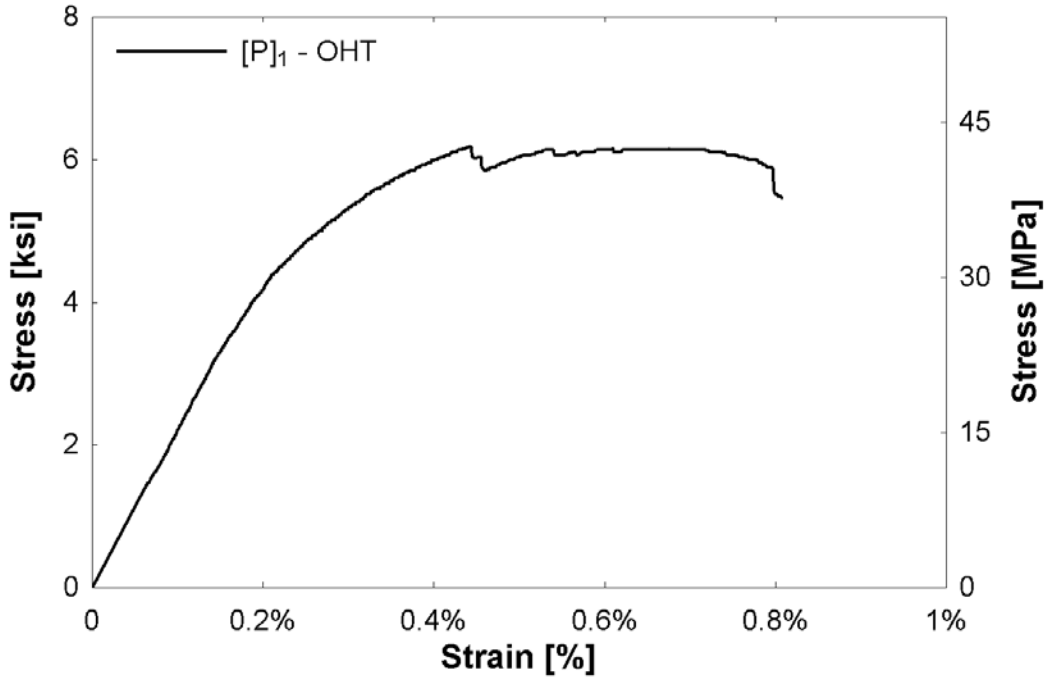

Figure B.2-14: Stress-strain relationship of perforated steel composite (Sample T) specimen under open-hole monolithic tensile loading.

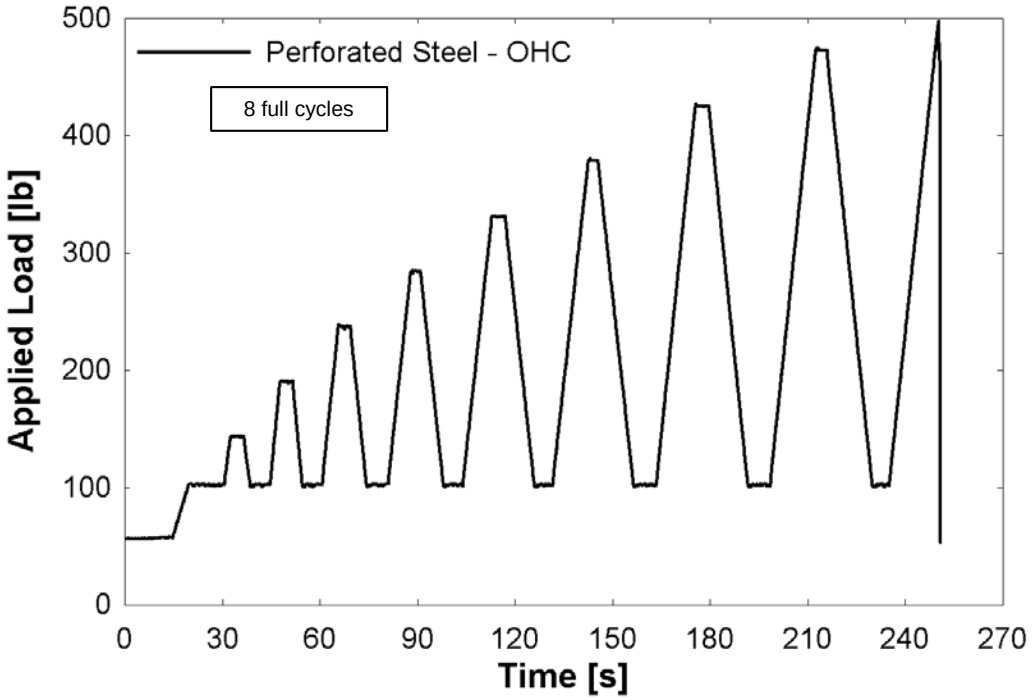

Figure B.2-15: Loading protocol of perforated steel composite (Sample T) specimen under open-hole half cyclic loading; each cycle increased by 10% of ultimate open-hole tensile strength

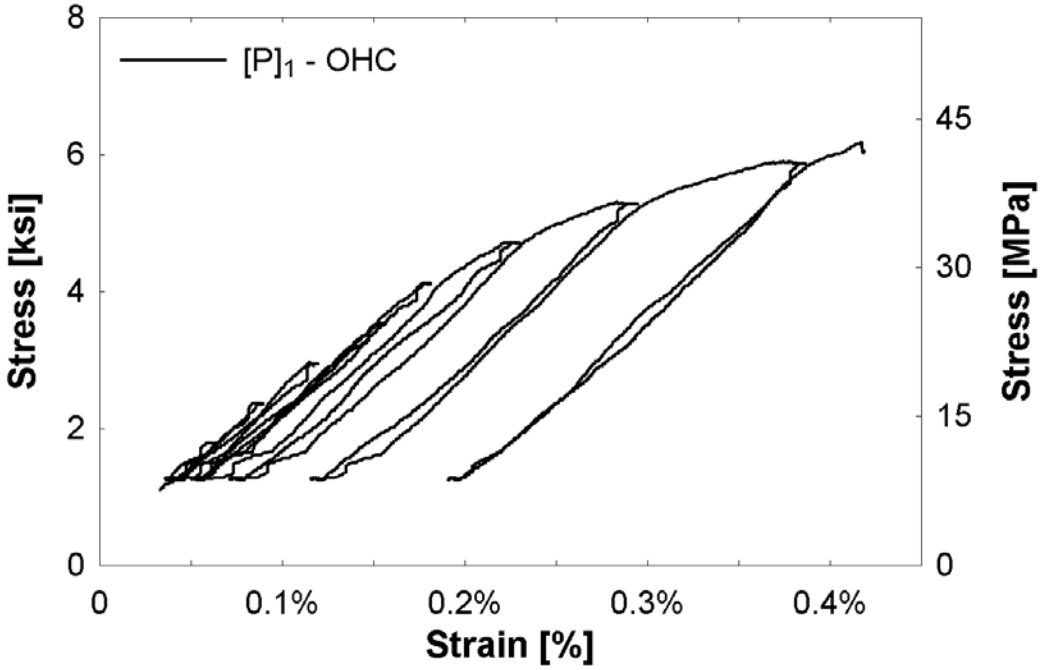

Figure B.2-16: Stress-strain relationship of perforated steel composite (Sample T) specimen under open-hole half-cyclic tensile loading.

B.3 Hybrid Composite Testing

70G:30S Hybrid

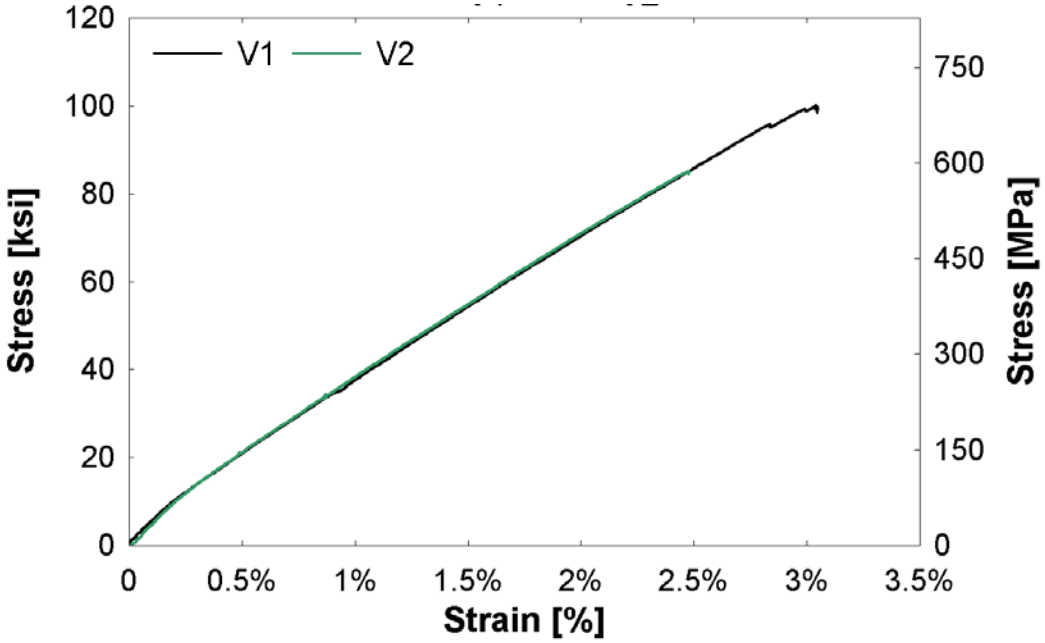

Figure B.3-1: Stress-strain relationship of 70:30 glass steel fiber hybrid composite (Sample V) specimens under monolithic tensile loading.

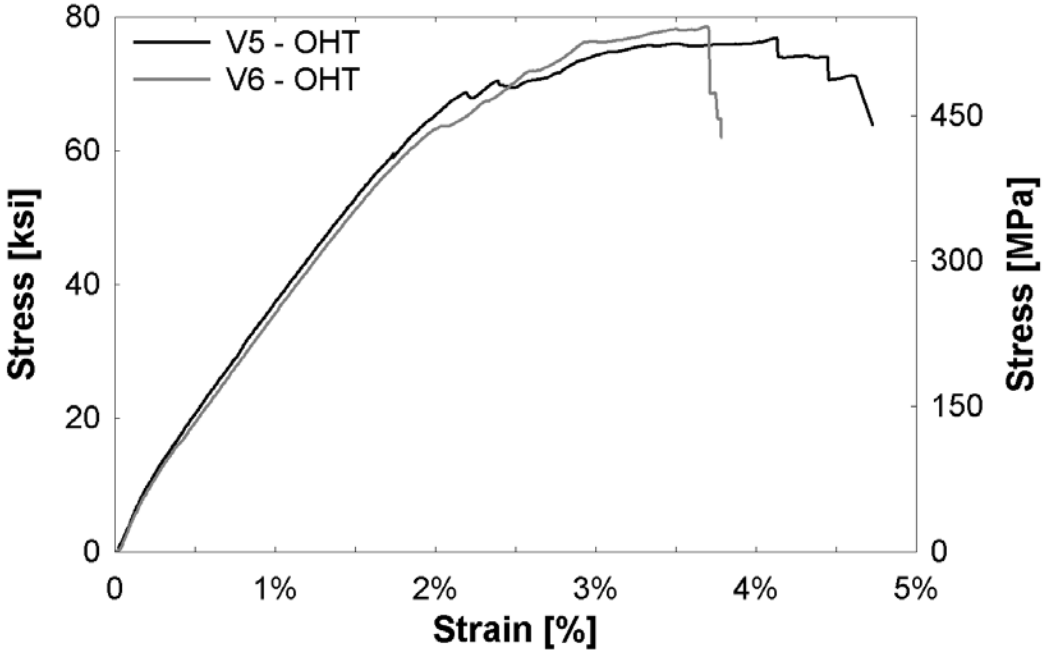

Figure B.3-2: Stress-strain relationship of 70:30 glass steel fiber hybrid composite (V) specimens under open-hole monolithic tensile loading.

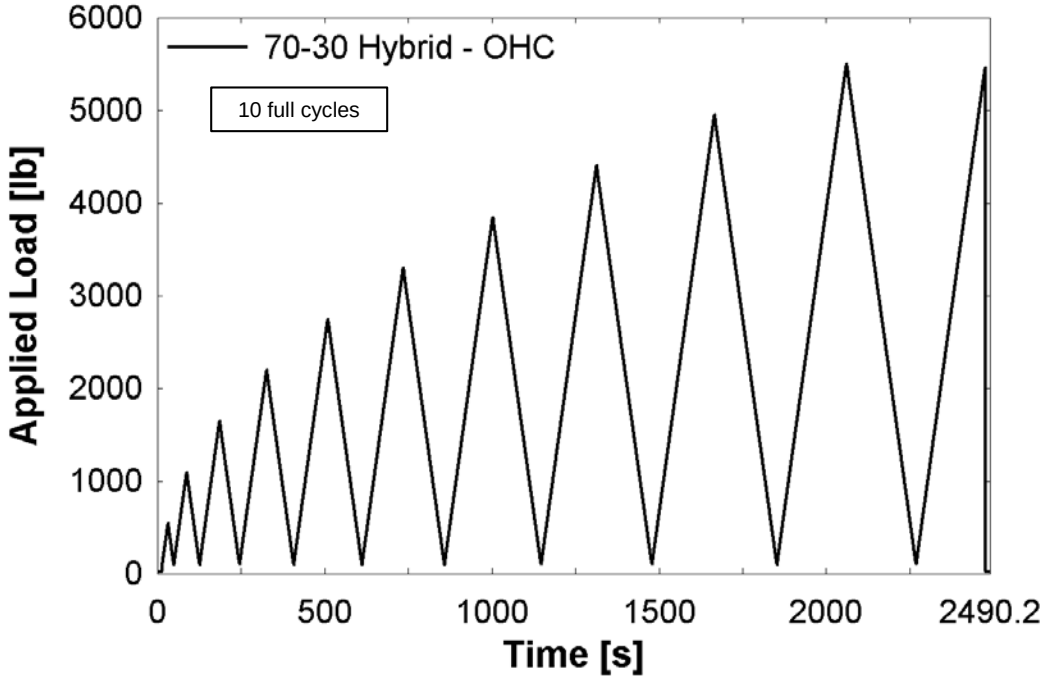

Figure B.3-3: Loading protocol of 70:30 glass steel fiber composite (Sample V) specimens under open-hole half cyclic loading; each cycle increased by 10% of ultimate open-hole tensile strength

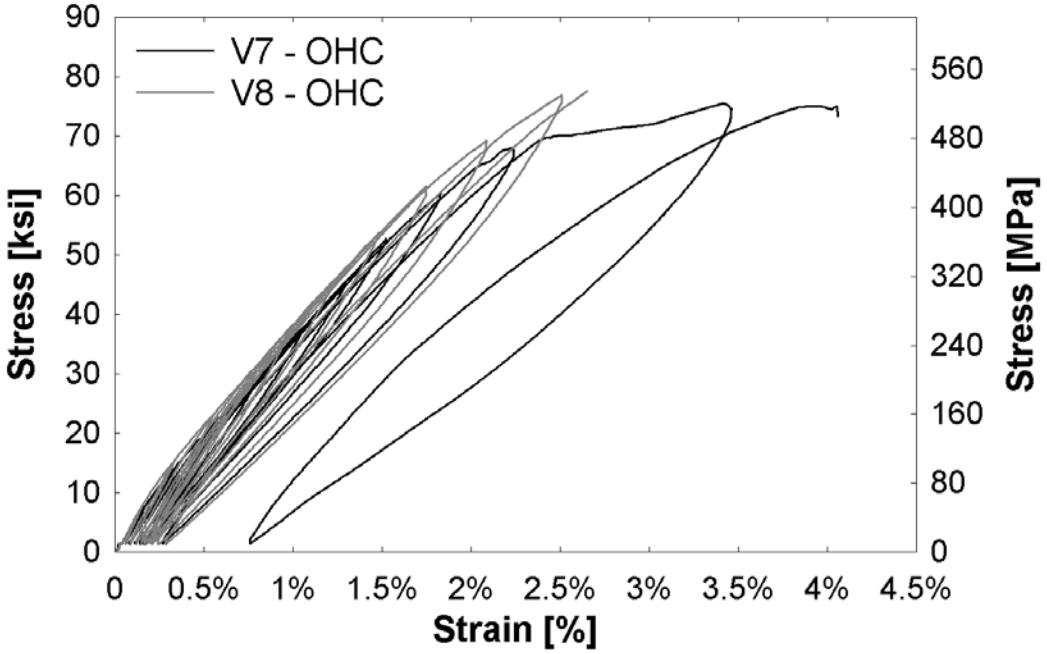

Figure B.3-4: Stress-strain relationship of 70:30 glass steel fiber composite (Sample V) specimens under open-hole half cyclic tensile loading

50G:50S Hybrid

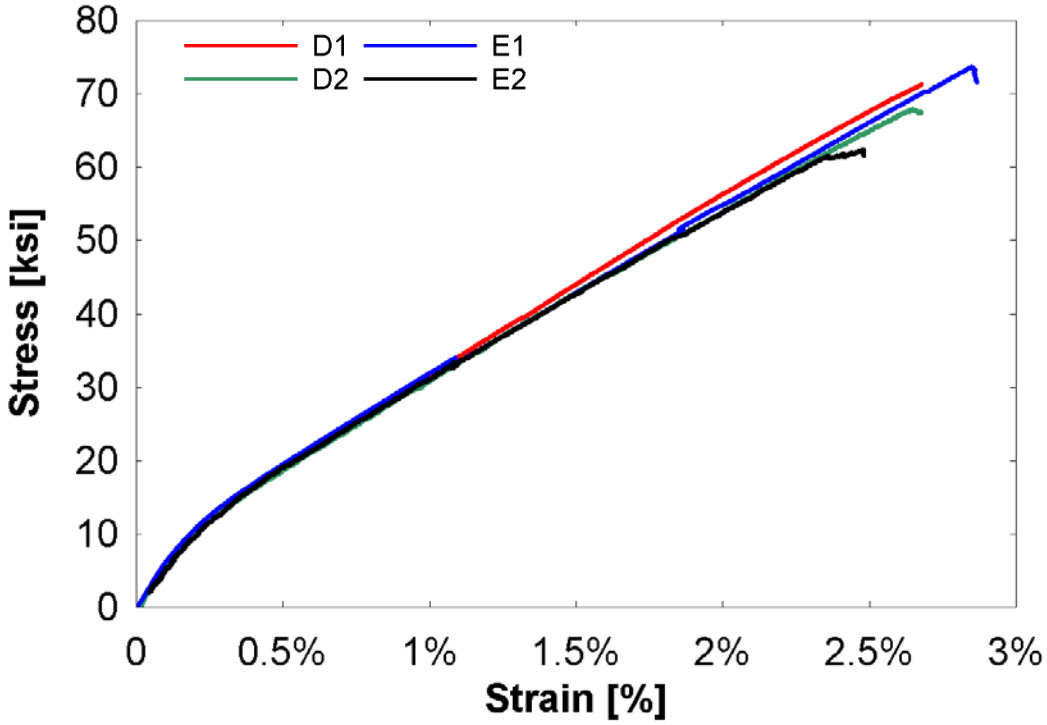

Figure B.3-5: Stress-strain relationship of 50:50 glass steel fiber hybrid composite (Sample D, E) specimens under monolithic tensile loading. Sample D represents bonded specimens and Sample E represents debonded specimens.

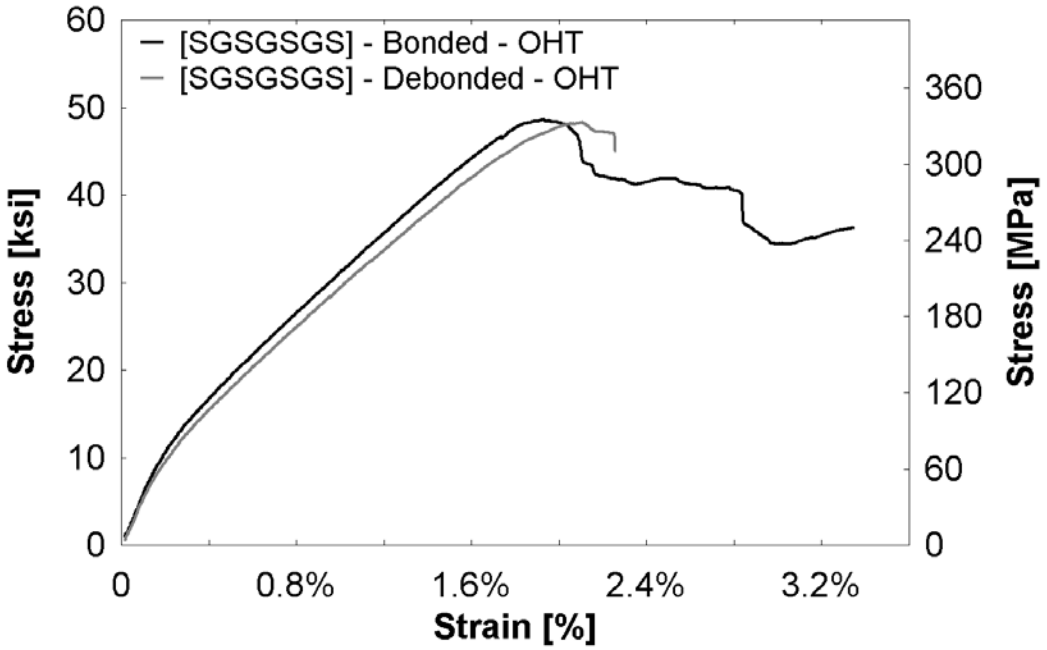

Figure B.3-6: Stress-strain relationship of 50:50 glass steel fiber hybrid composite (Sample D, E) specimens under open-hole monolithic tensile loading.

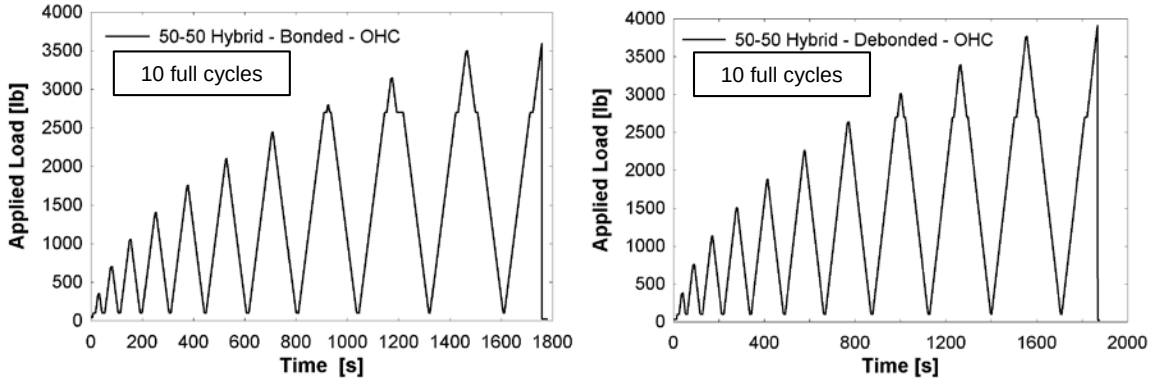

Figure B.3-7: Loading protocol of 50:50 glass steel fiber composite (Sample D, E) specimens under open-hole half cyclic loading
Note: Each cycle increased by 10% of ultimate open-hole tensile strength

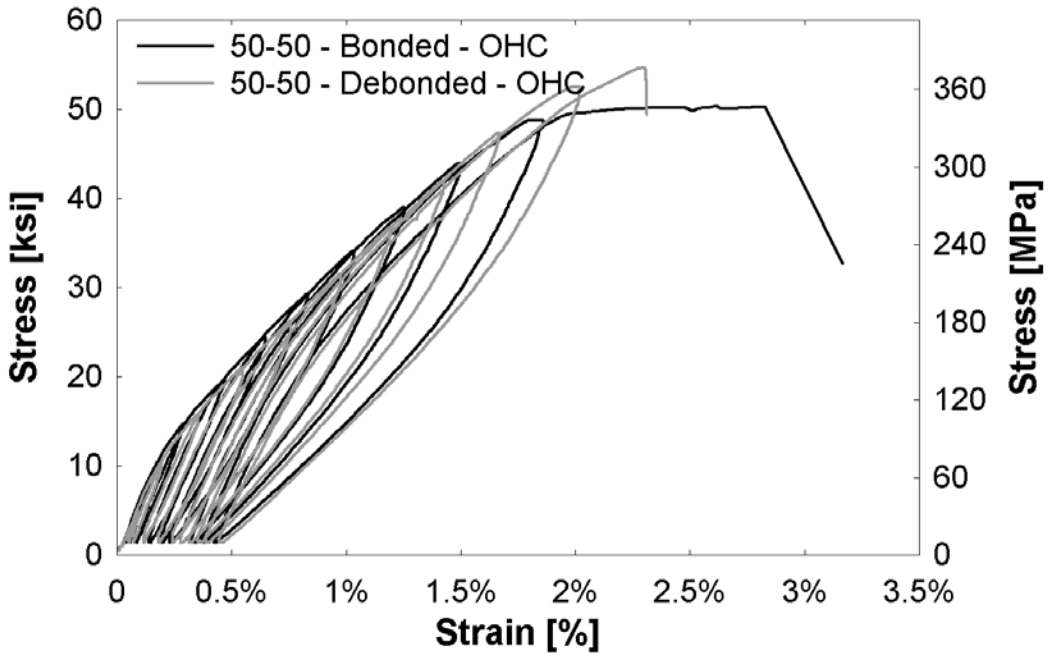

Figure B.3-8: Stress-strain relationship of 50:50 glass steel fiber composite (Sample D, E) specimens under open-hole half cyclic tensile loading

30G:70S Hybrid

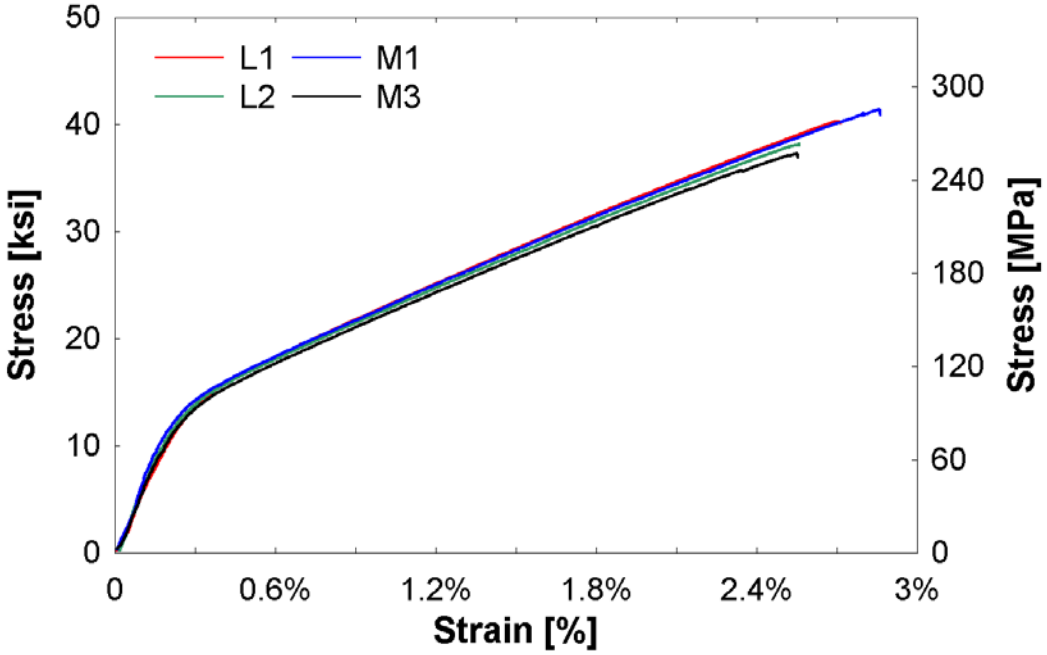

Figure B.3-9: Stress-strain relationship of 30:70 glass steel fiber hybrid composite (Sample L, M) specimens under monolithic tensile loading. Sample L represents bonded specimens and Sample M represents debonded specimens

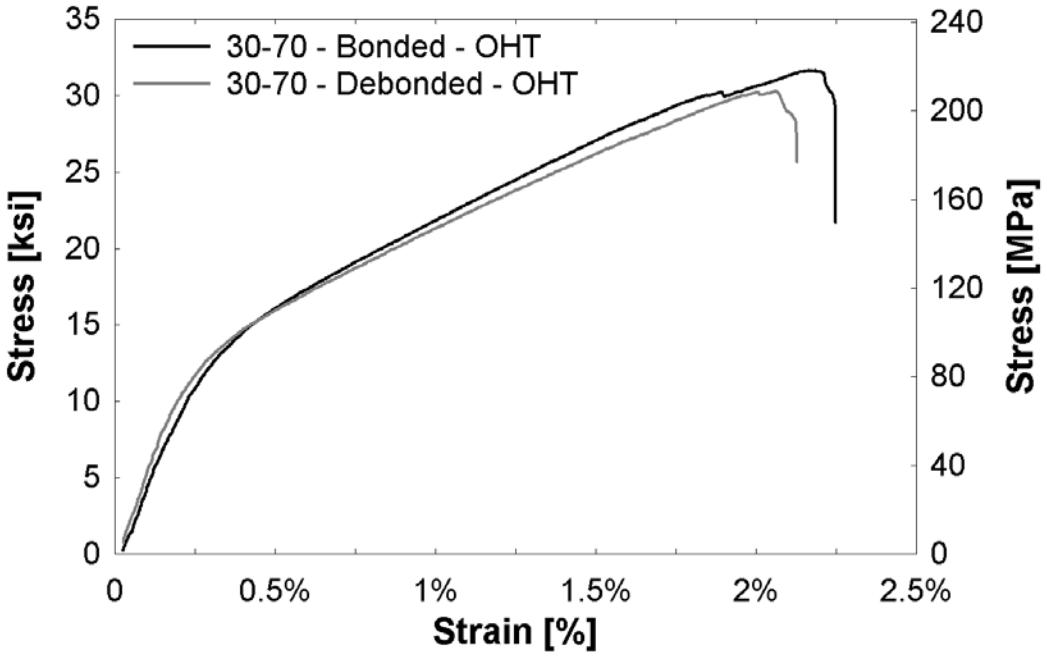

Figure B.3-10: Stress-strain relationship of 70:30 glass steel fiber hybrid composite (Sample L, M) specimens under open-hole monolithic tensile loading

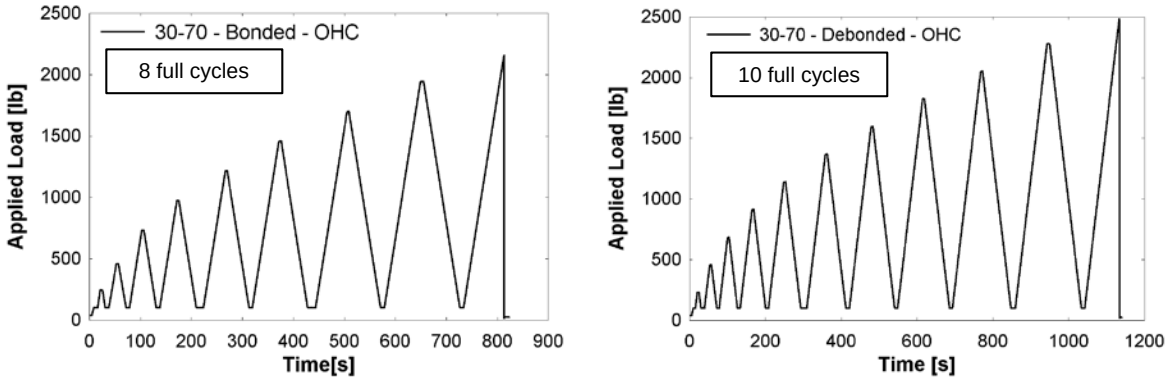

Figure B.3-11: Loading protocol of 30:70 glass steel fiber composite (Sample L, M) specimens under open-hole half cyclic loading
Note: Each cycle increased by 10% of ultimate open-hole tensile strength

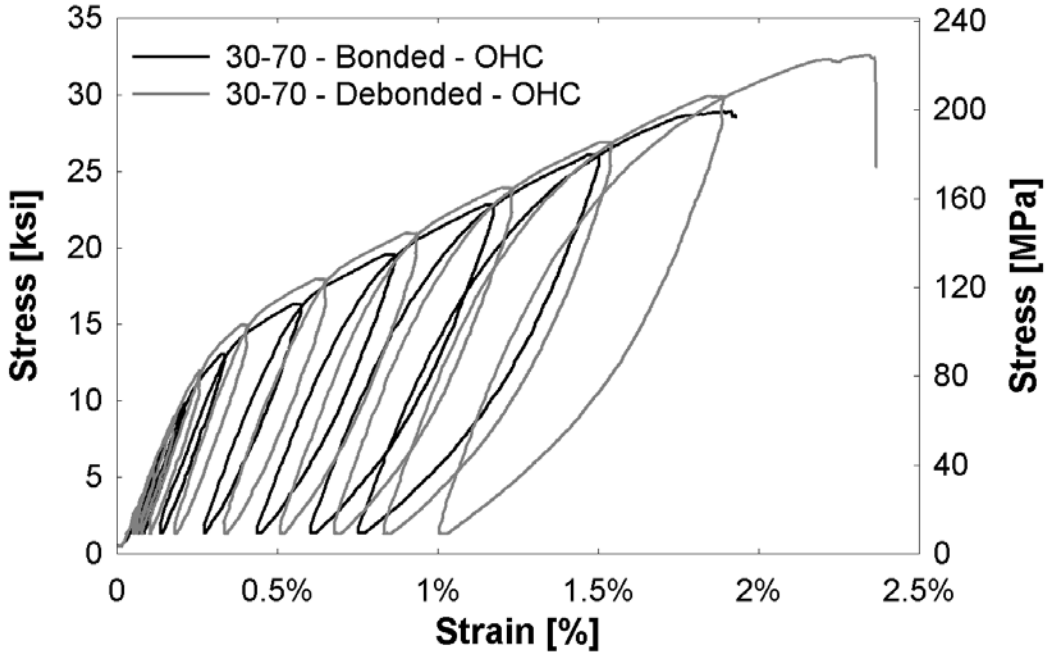

Figure B.3-12: Stress-strain relationship of 30:70 glass steel fiber composite (Sample L, M) specimens under open-hole half cyclic tensile loading

Steel Mesh Hybrid

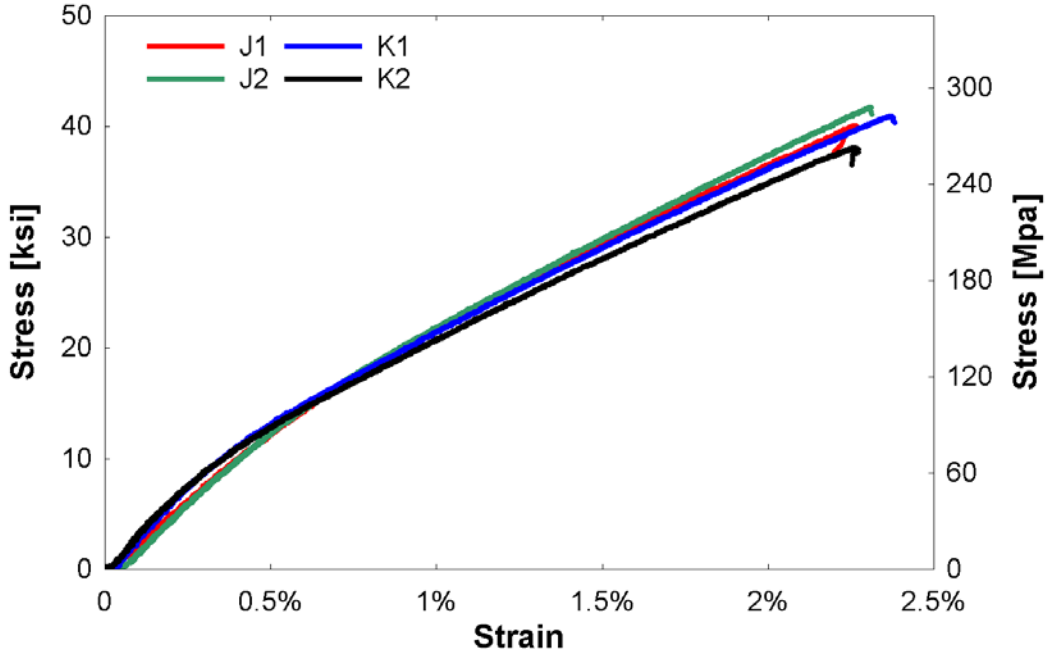

Figure B.3-13: Stress-strain relationship of steel mesh hybrid composite (Sample J, K) specimens under monolithic tensile loading. Sample J represents bonded specimens and Sample K represents debonded specimens

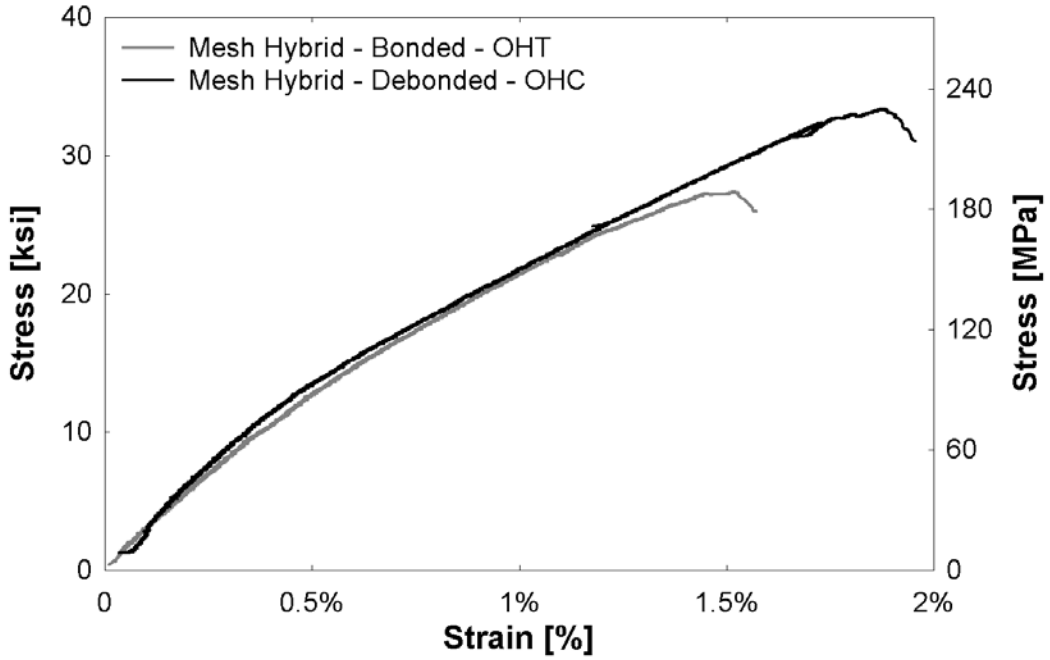

Figure B.3-14: Stress-strain relationship of steel mesh hybrid composite (Sample J, K) specimens under open-hole monolithic tensile loading

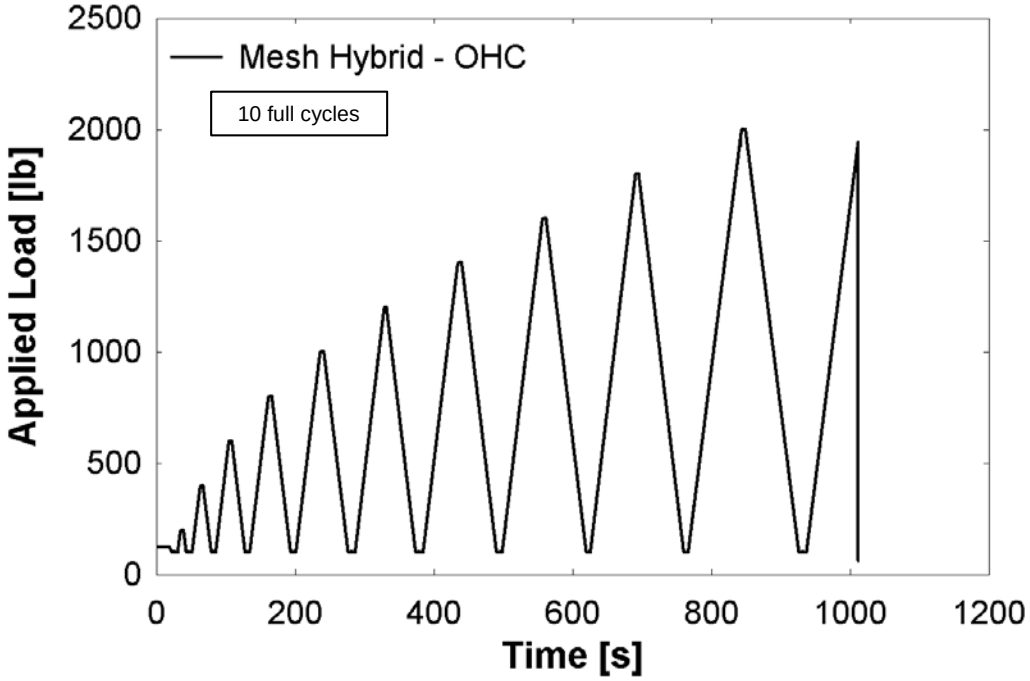

Figure B.3-15: Loading protocol of steel mesh hybrid composite (Sample J) specimen under open-hole half cyclic loading
Note: Each cycle increased by 10% of ultimate open-hole tensile strength

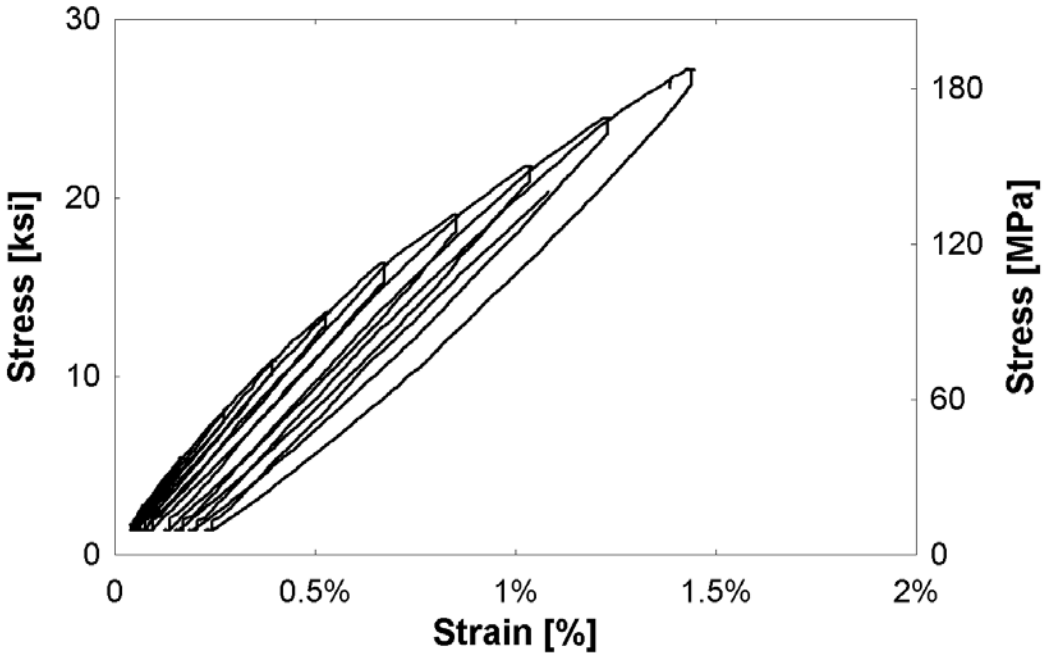

Figure B.3-16: Stress-strain relationship of steel mesh hybrid composite (Sample J) specimen under open-hole half cyclic tensile loading

Perforated Steel Hybrid

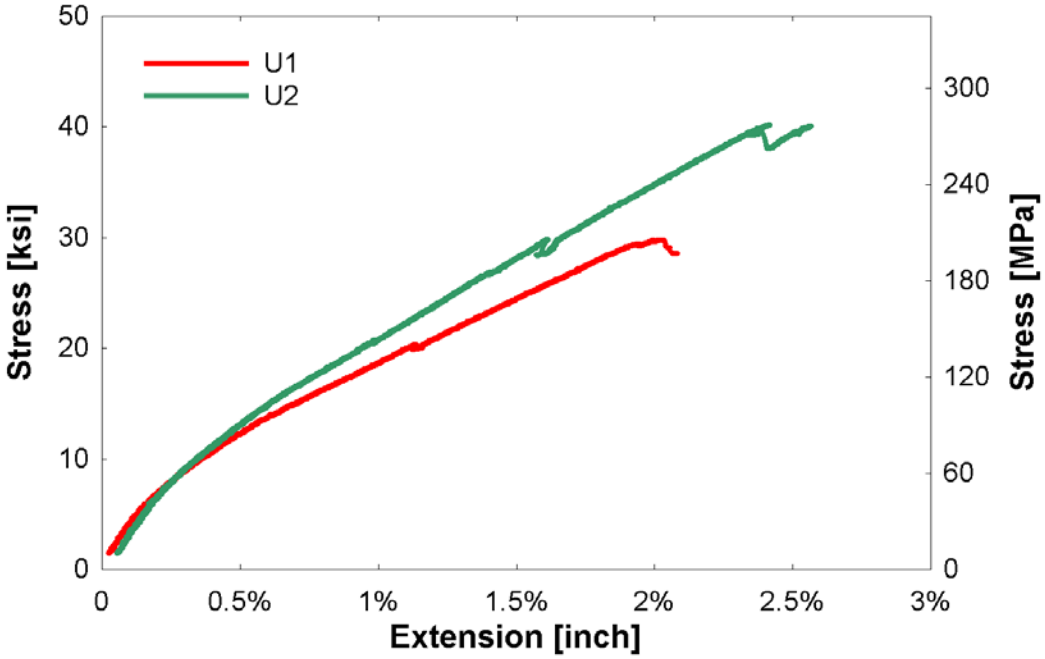

Figure B.3-17: Stress-strain relationship of perforated steel hybrid composite (Sample U) specimens under monolithic tensile loading.

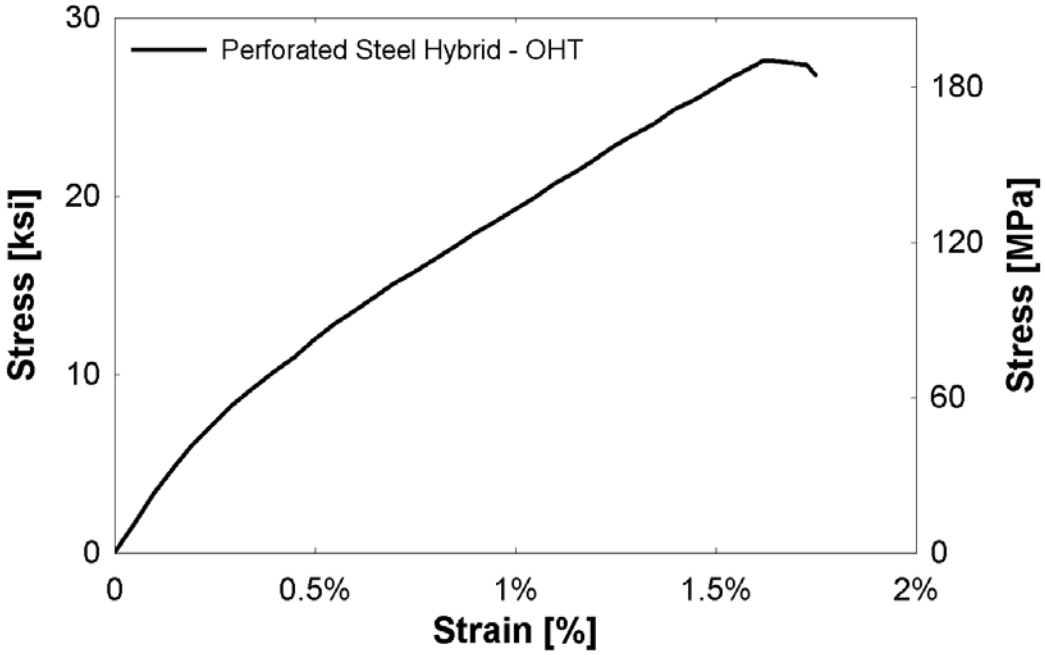

Figure B.3-18: Stress-strain relationship of perforated steel hybrid composite (Sample U) specimen under open-hole monolithic tensile loading

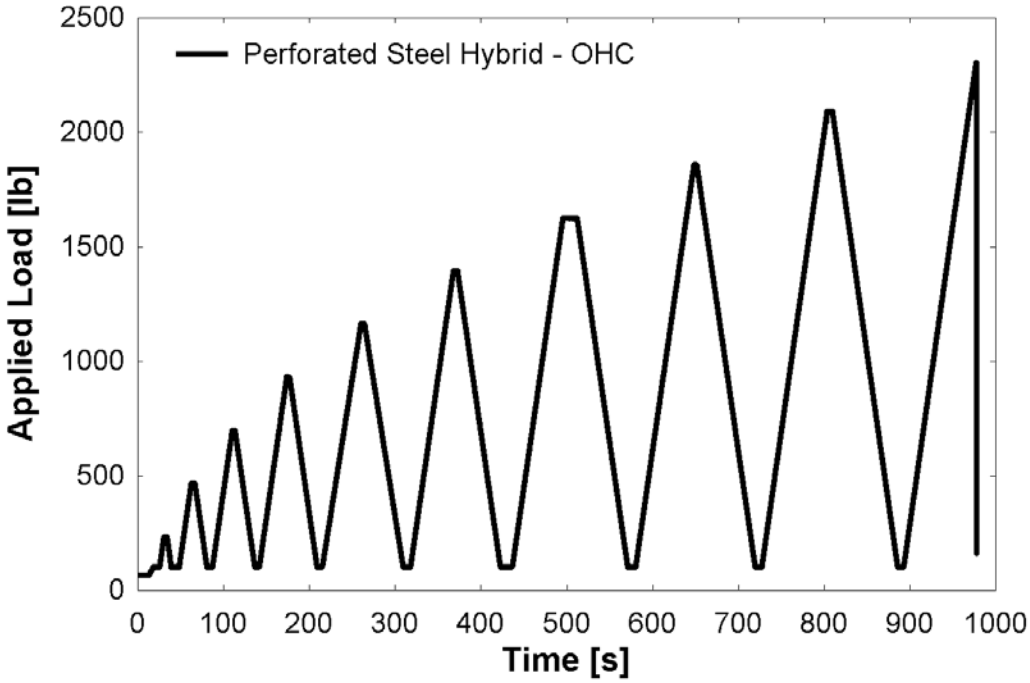

Figure B.3-19: Loading protocol of steel mesh hybrid composite (Sample U) specimen under open-hole half cyclic loading
Note: Each cycle increased by 10% of ultimate open-hole tensile strength

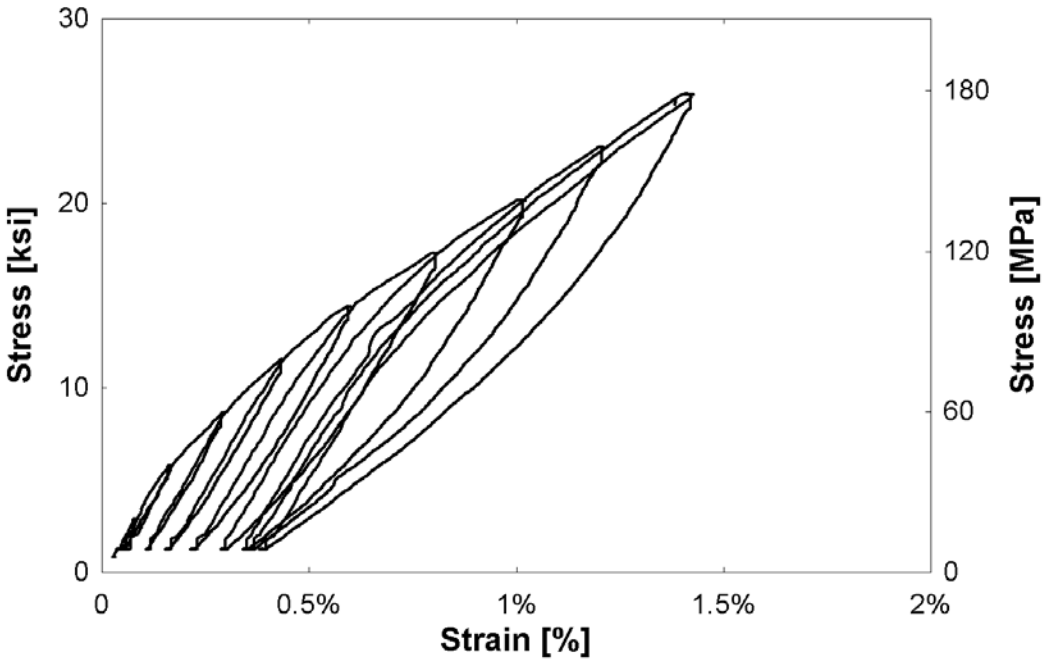

Figure B.3-20: Stress-strain relationship of perforated steel hybrid composite (Sample U) specimen under open-hole half cyclic tensile loading

APPENDIX C: Failure Specimens

C.1 Epoxy Specimens

EPON 826 – Room Temperature

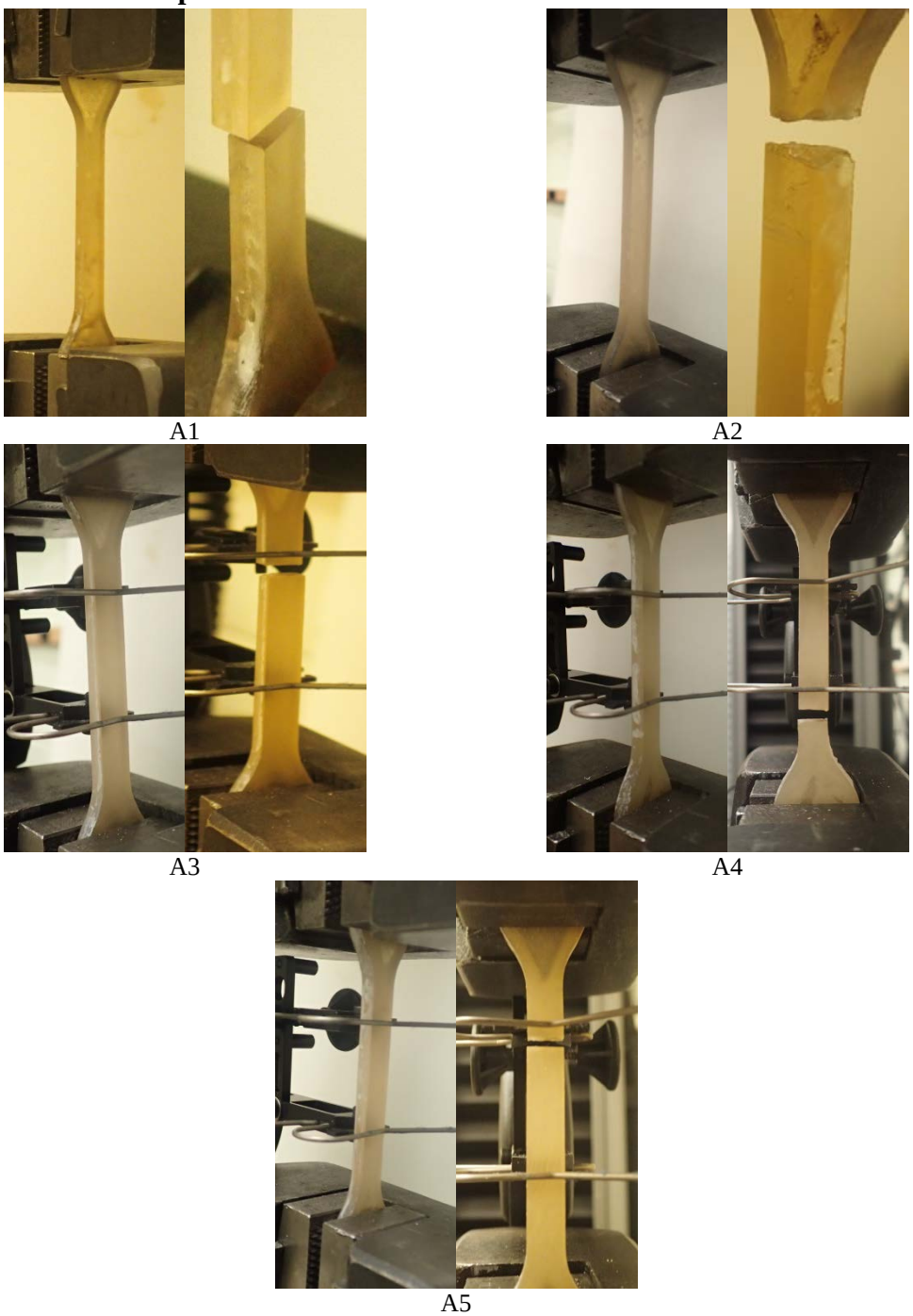

A1 A2

A3 A4

A5

Figure C.1-1 EPON 826 failure specimens

EPON 828 – Room Temperature

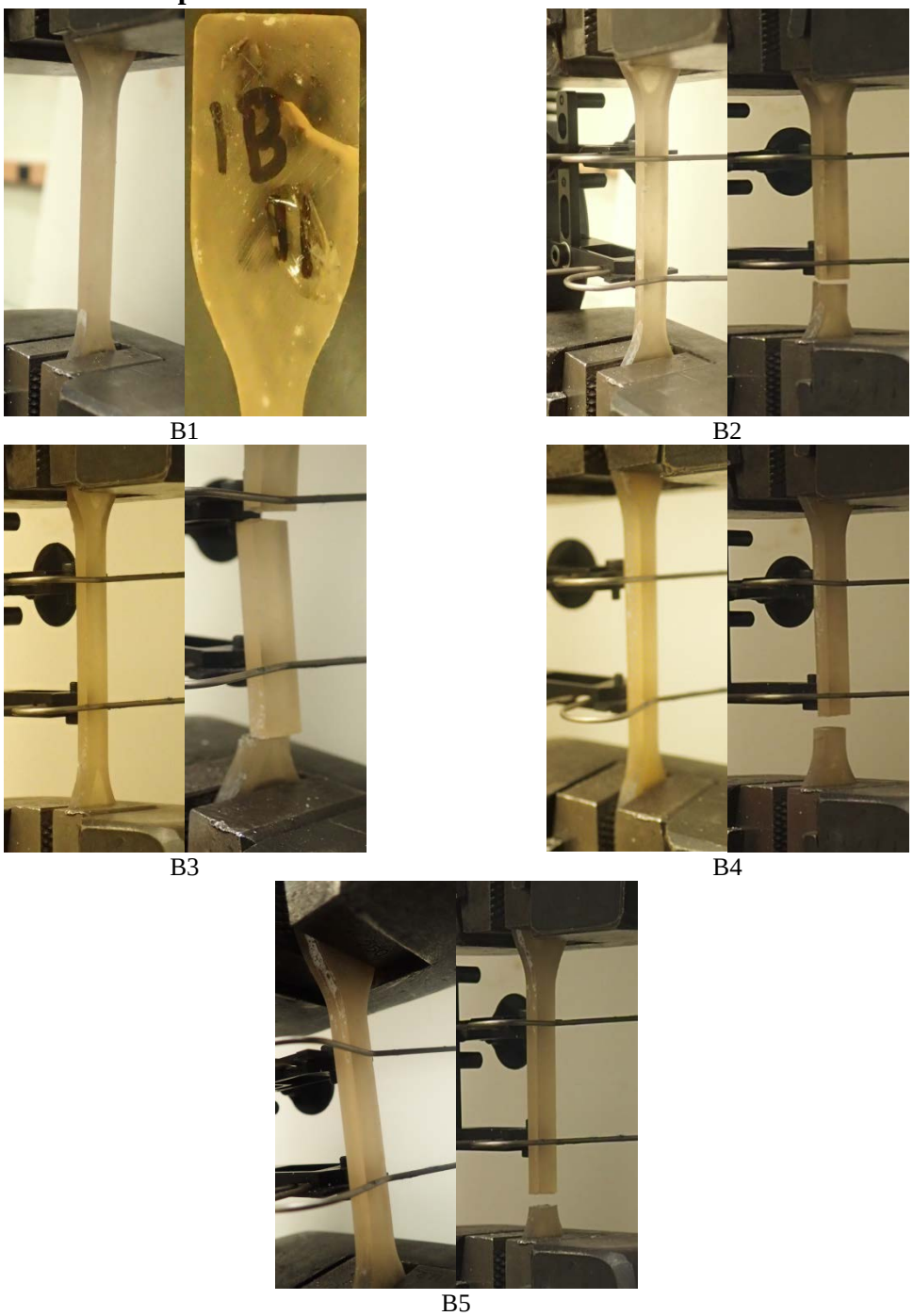

Figure C.1-2 EPON 828 (room temperature) failure specimens

EPIKOTE 874– Room Temperature

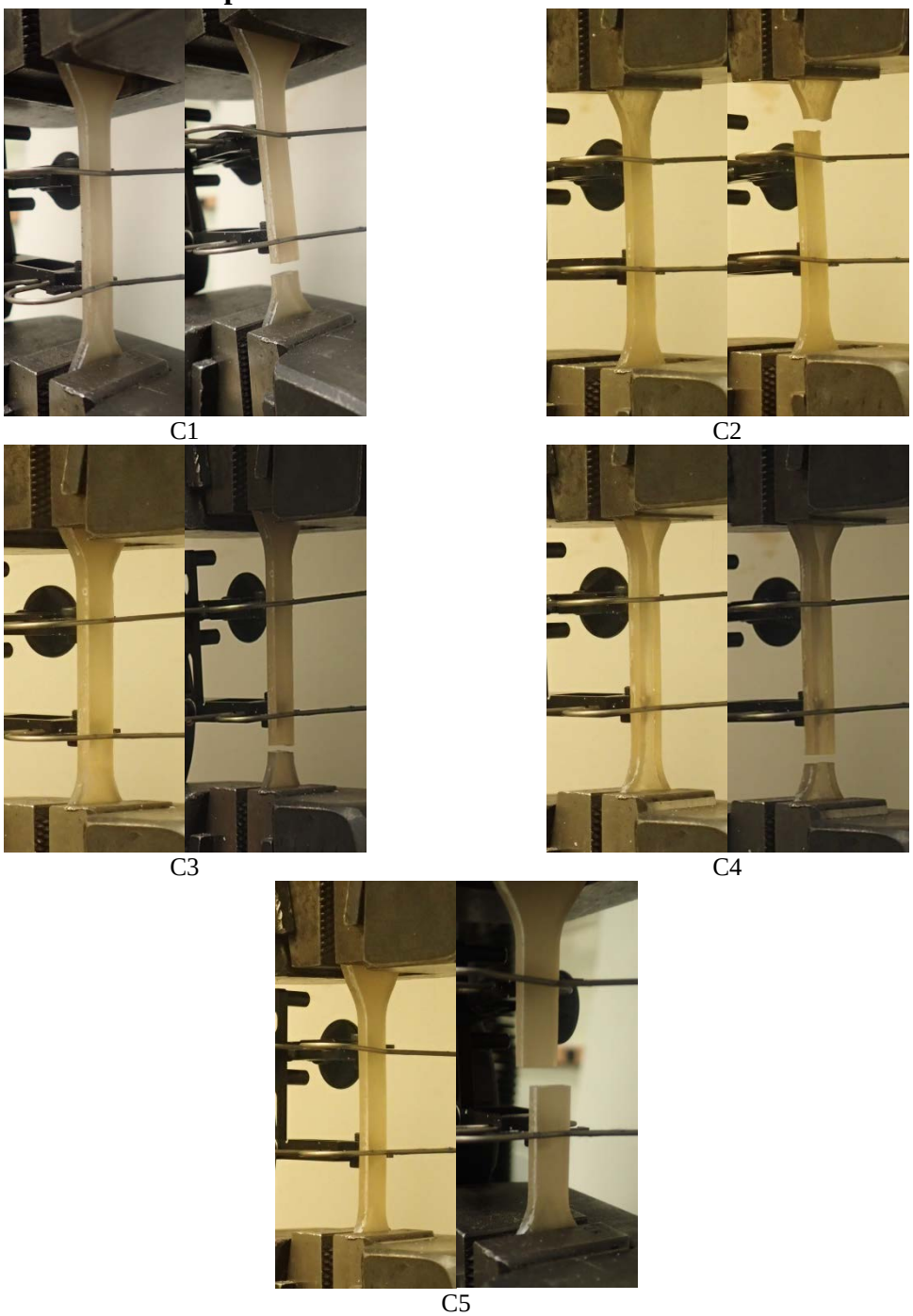

C1 C2

C3 C4

C5

Figure C.1-3 EPIKOTE 874 failure specimens

EPON 828 – Heat Cure

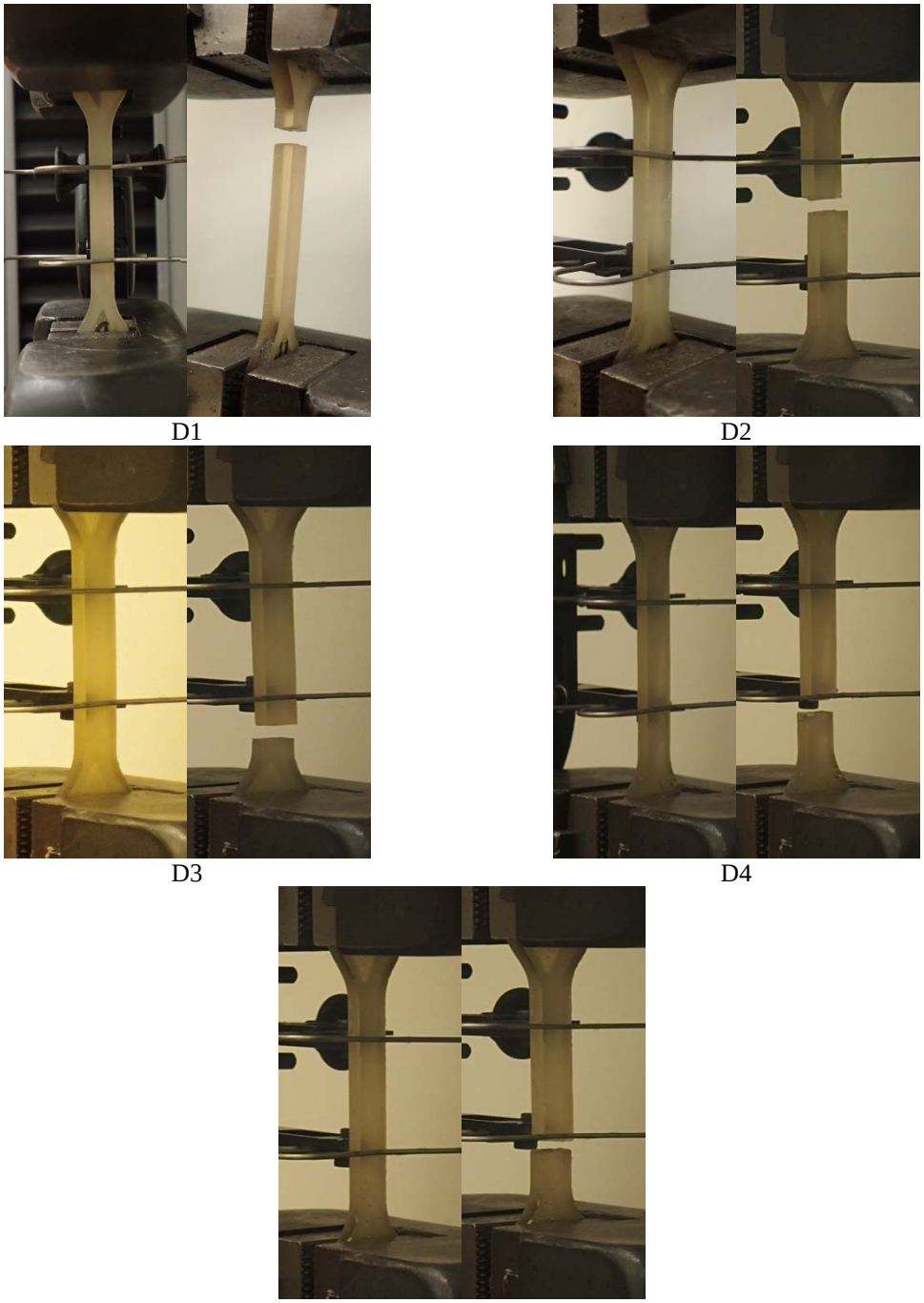

D1 D2

D3 D4

D5

Figure C.1-4 EPON 828 (heat cured) failure specimens

C2. Non-hybrid Composite Specimens

Unidirectional Glass

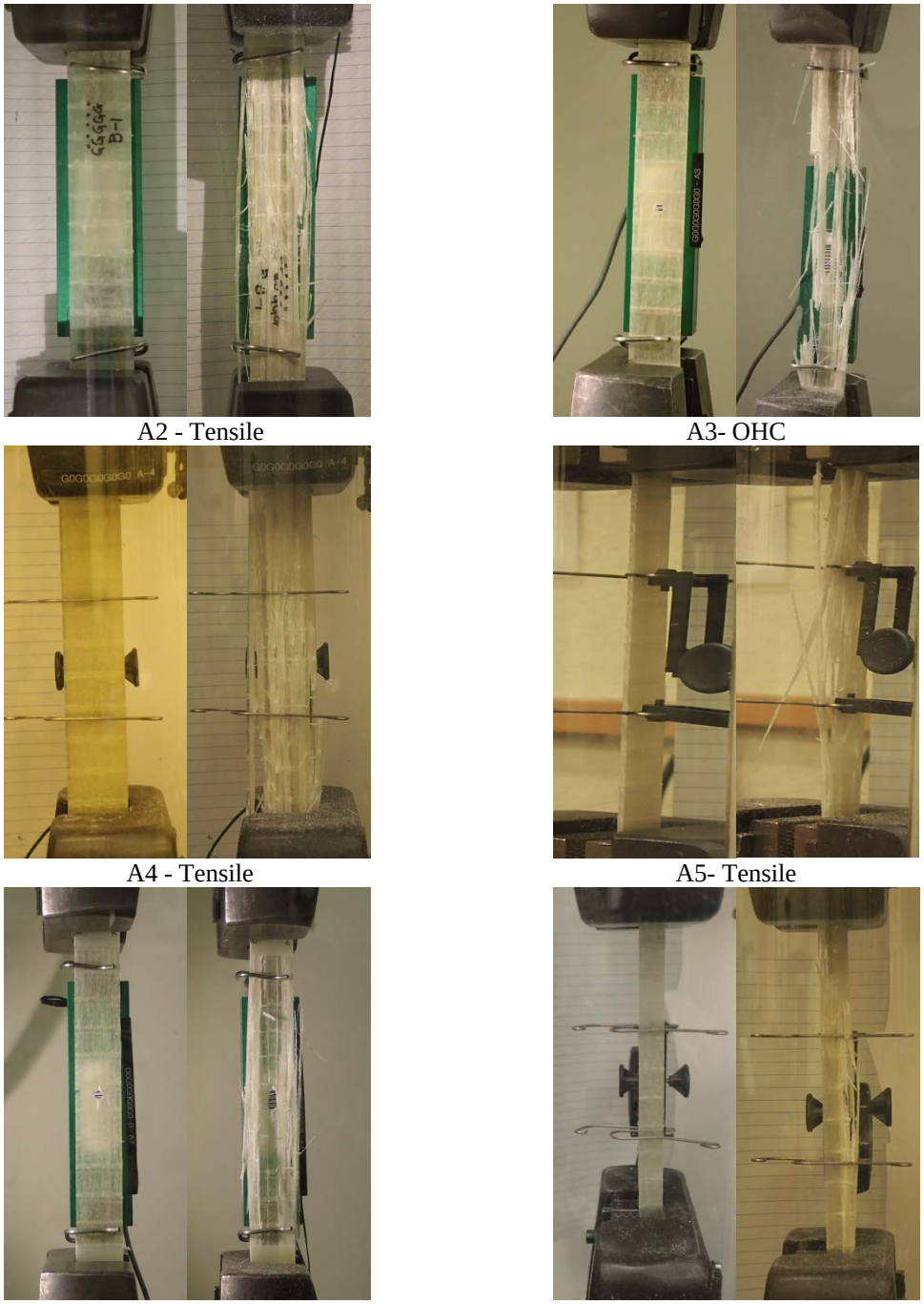

A2 - Tensile | A3- OHC

A4 - Tensile | A5- Tensile

A7 - OHT | A8 – Tensile

Figure C.2-1 $[G]_5$ composite failure specimens

Unidirectional Steel

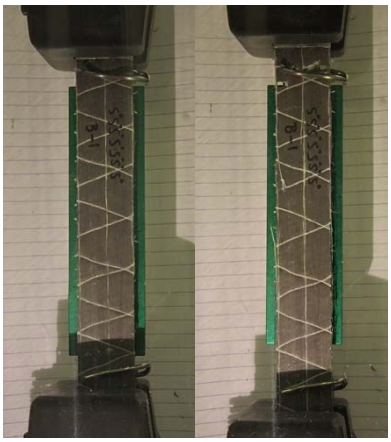

B1 – Tension

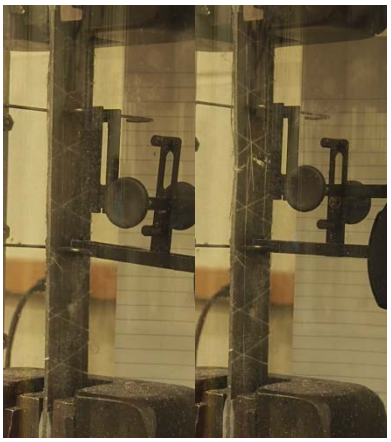

B2 – Tension

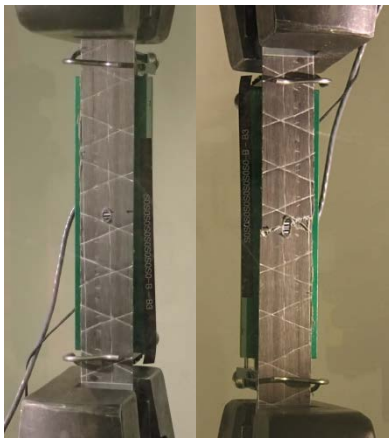

B3 - OHT

B4 – OHC

C1 – Tension

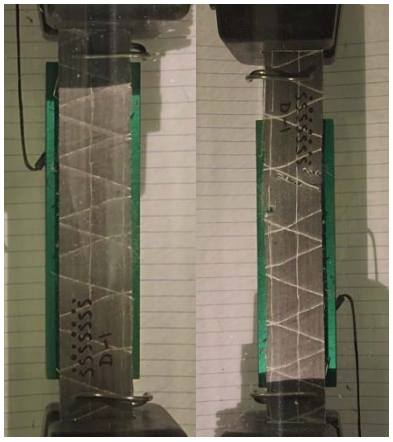

C2 – Tension

C4 – OHT

C4 – OHC

Figure C.2-2 $[S]_8$ composite failure specimens

Steel Mesh

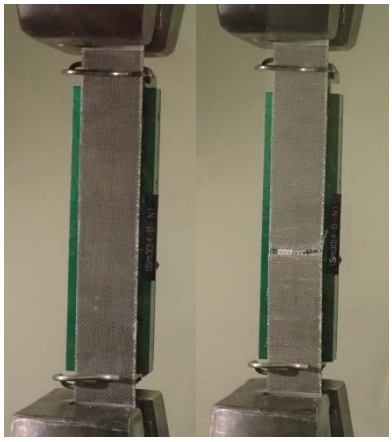

N1 – Tension

N2 – Tension

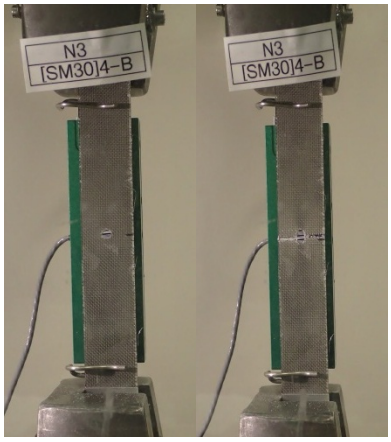

N3 – OHT

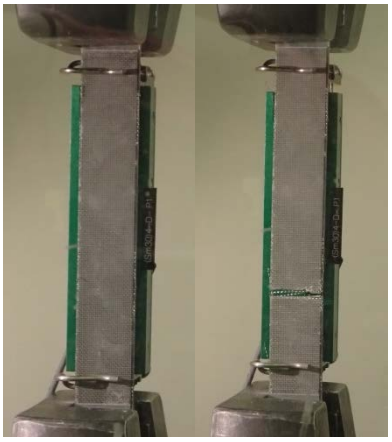

P1 - Tension

P2 – Tension

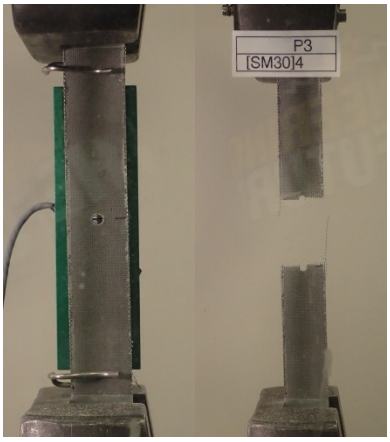

P3 – OHC

Figure C.2-3 $[M]_4$ composite failure specimens

Perforated Steel

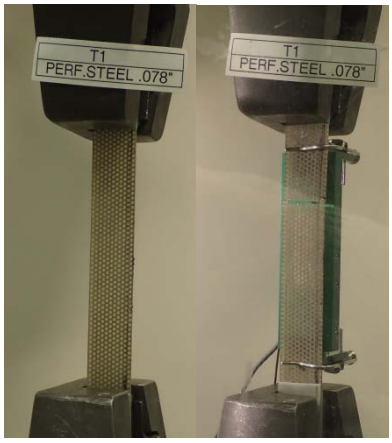

T1 – Tension

T2 – Tension

T3 – OHT

T4 – OHC

Figure C.2-4 $[P]_1$ composite failure specimens

C. 3 Hybrid Composite Specimens

70:30 Hybrid

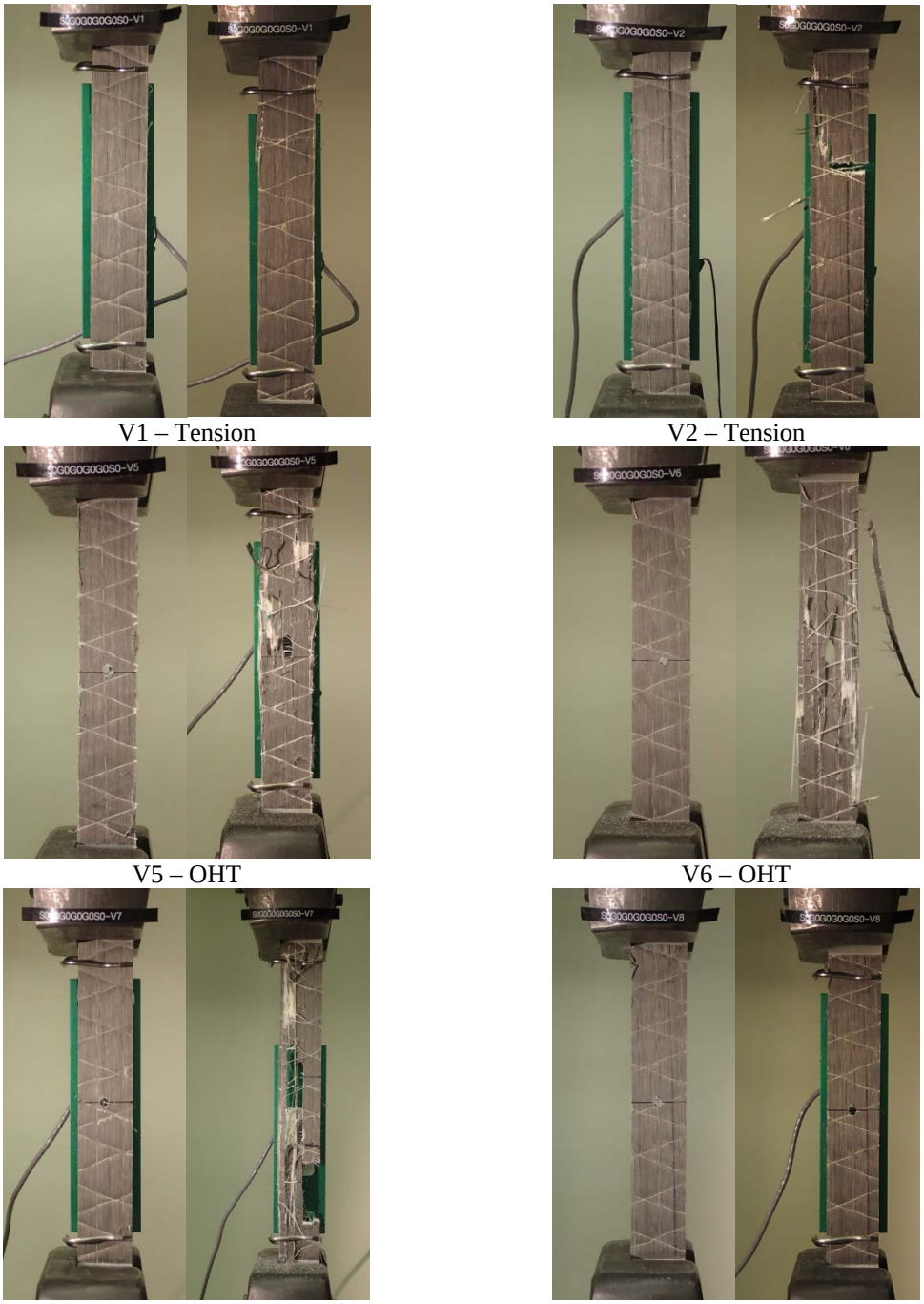

V1 – Tension V2 – Tension

V5 – OHT V6 – OHT

V7 – OHC V8 – OHC

Figure C.3-1 [SGGGGS] composite failure specimens

50:50 Hybrid

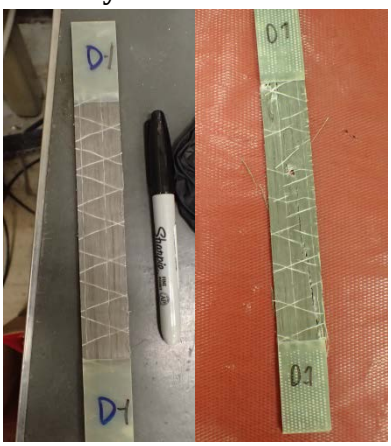
D1 – Tension

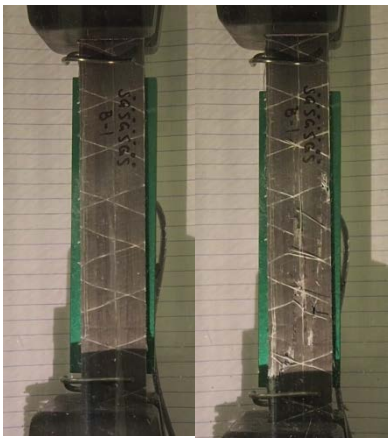
D2 – Tension

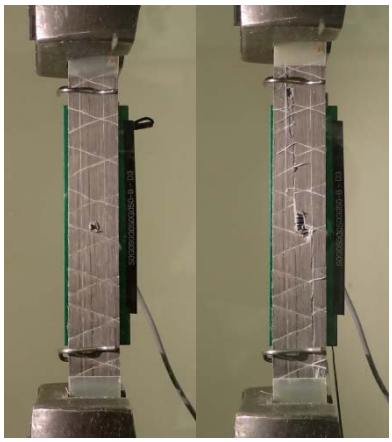
D3 – OHT


D4 – OHC

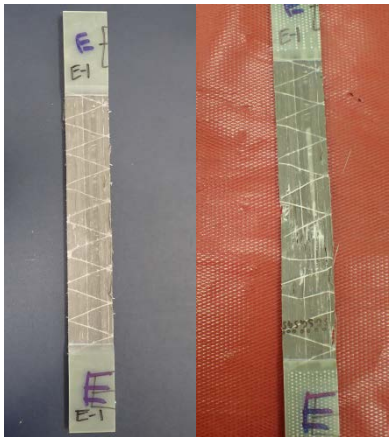
E1 – Tension

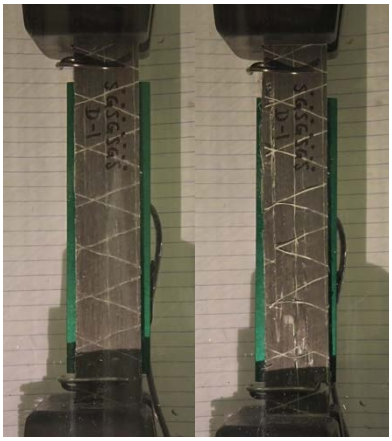
E2– Tension


E3 – OHT


E4 – OHC

Figure C.3-2 [SGSGSGS] composite failure specimens

30:70 Hybrid

L1 – Tension

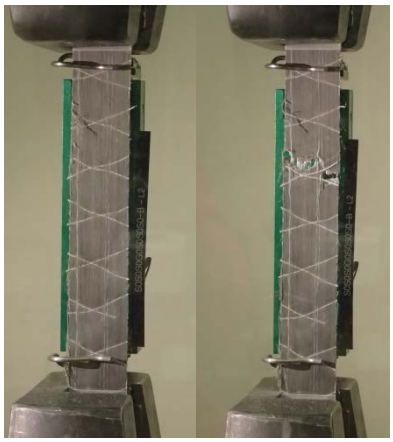

L2 – Tension

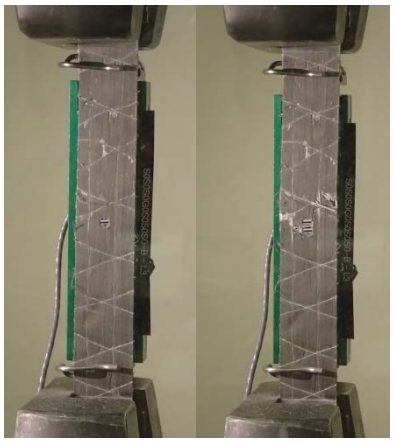

L3 – OHT

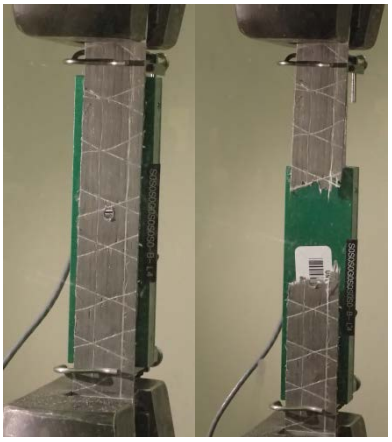

L4 – OHC

M1 – Tension

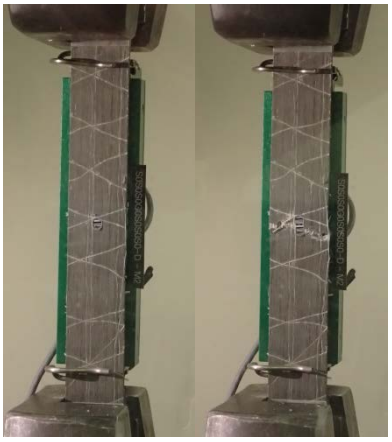

M3 – Tension

M2 – OHT

M4 – OHC

Figure C.3-3 [SSSGSSS] composite failure specimens

Steel Mesh Hybrid

J1 – Tension

J2 – Tension

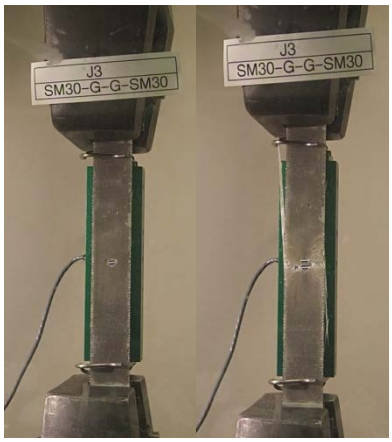

J3 – OHT

J4 – OHC

K1 – Tension

K2 – Tension

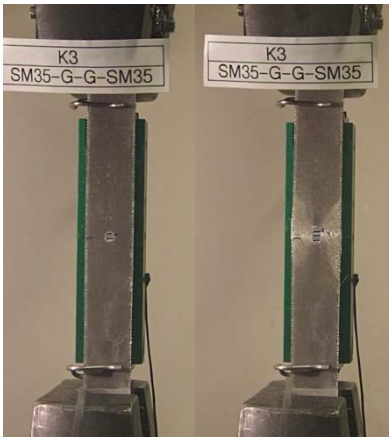

K3 – OHT

Figure C.3-4 [MGGM] composite failure specimens

Perforated Steel Hybrid

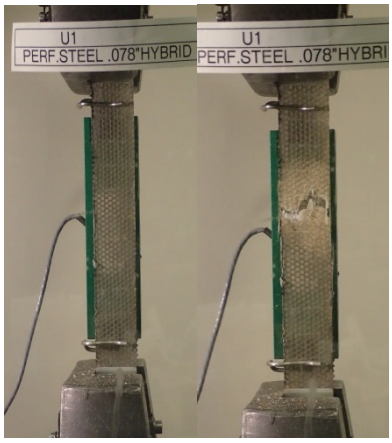

U1 – Tension

U2 – Tension

U3 – OHT

U4 – OHC

Figure C.3-5 [GPG] composite failure specimens